Dissertation

submitted to the
Combined Faculties of the Natural Sciences and Mathematics
of the
Ruperto-Carola University of Heidelberg, Germany
for the degree of

Doctor of Natural Sciences

presented by
Dipl.-Phys. Anne Bochow
born in Eberswalde-Finow

Oral examination: 3rd February 2011

A systematic study of Supernova Remnants as seen with H.E.S.S.

Referees: Prof. Dr. Werner Hofmann
Prof. Dr. Heinz Völk

Abstract

Supernova remnants (SNRs) are the remainders of extremely energetic explosions occurring at the end of a star's life. With the energy released during the supernova explosion they are believed to accelerate charged particles to energies of up to 10^{15} eV. In the very-high-energy (VHE, $> 10^{11}$ eV) γ-ray band, SNRs represent one of the most populous classes of Galactic sources. Due to its unprecedented sensitivity, H.E.S.S. was the first instrument to allow for a morphological resolution of individual SNRs, proving the existence of particle acceleration and subsequent VHE γ-ray emission. However, to date many more SNRs are known in the radio waveband than in VHE γ-rays. This work presents a systematic study of the VHE γ-ray signal of a sample of around 200 radio SNRs. The VHE γ-ray-signal of these SNRs is studied individually. Besides the spatial correlation of radio SNRs and VHE γ-ray sources, the measured flux of VHE γ-rays is compared to theoretical flux predictions. These predictions are based on assumptions of the total explosion energy, the particle acceleration efficiency, the density of the surrounding medium and the distance of the SNRs. The results presented here suggest that these parameters can vary strongly for individual SNRs. Future observations of SNRs in VHE γ-rays and other wavebands will help to constrain the parameter space and will allow to further discuss acceleration mechanisms in SNRs.

Kurzfassung

Das Leben eines massiven Sterns endet in einer Supernovaexplosion. Dabei werden große Massen von Materie in das interstellare Medium geschleudert und gewaltige Energiemengen freigesetzt. Vom verbleibenden Supernovaüberrest wird weithin angenommen, dass dort geladene Teilchen auf Energien von bis zu 10^{15} eV beschleunigt werden können. Im Wellenlängenbereich der sehr hochenergetischen γ-Strahlung ($> 10^{11}$ eV) gehören Supernovaüberreste zu den zahlenmäßig dominanten Klassen galaktischer Quellen. Dank der herausragenden Empfindlichkeit des H.E.S.S.-Detektors konnte die Morphologie mehrerer Supernovaüberreste aufgelöst werden und somit ein Zusammenhang zwischen Teilchenbeschleunigung in Supernovaüberresten und sehr hochenergetischer γ-Strahlung hergestellt werden. Dennoch sind im Radiowellenlängenbereich wesentlich mehr Supernovaüberreste bekannt als bisher im γ-Bereich detektiert wurden. In der vorliegenden Arbeit wird erstmals eine systematische Untersuchung von etwa 200 im Radiobereich bekannten Supernovaüberresten präsentiert. Der gemessene hochenergetische γ-Fluss wird mit einem theoretisch ermittelten Wert verglichen, der auf Annahmen der Gesamtenergie der Supernovaexplosion, der Beschleunigungseffizienz der Teilchen im Supernovaüberrest, der Umgebungsdichte und der Entfernung basiert. Die Ergebnisse dieser Studie verdeutlichen die Abweichung dieser Parameter vom angenommen Wert für viele Überreste. Zukünftige Beobachtungen im sehr hochenergetischen γ-Bereich und anderen Wellenlängen können daher einen wichtigen Beitrag liefern, die Parameter einzuschränken und Beschleunigungsmechanismen in Supernovaüberresten genauer zu untersuchen.

Contents

1 Introduction

Supernova explosions belong to the most violent processes in the universe, with energies released of up to 10^{51} erg (=10^{44} J). Astronomers all over the world have observed supernovae already hundreds of years ago and studied their behavior. The documentation of these observations provides detailed information about supernova explosions, predicting a supernova to occur every few decades within our Galaxy. Most of them are obscured by dust and so only for few the explosion date is known. These supernovae, observed by Arabic, Chinese, Japanese and European astronomers in the years 1006, 1054, 1572 (documented by Tycho Brahe), and 1604 (documented by Johannes Kepler) are called historical supernovae. The last supernova visible to the naked eye occurred in 1987 in the Large Magellanic Cloud.

Following a supernova explosion a shock front expands into the interstellar medium. It is widely believed that this shock front is a source of cosmic rays with energies of up to 10^{15} eV. Travelling through the galaxy, the cosmic rays are deflected in turbulent magnetic fields. Therefore their arrival directions are isotropically distributed, making it impossible to backtrace their source of origin. The only way to visualize the sources of cosmic rays is through the detection of electromagnetic radiation like γ-rays and of neutral secondary particles like neutrinos, which are not deflected by magnetic fields. The detection of cosmic neutrinos is very difficult and requires large detection volumes. Electromagnetic radiation in the radio and X-ray waveband results from Bremsstrahung and synchrotron radiation of electrons as well as from line emission, whereas γ-rays are generated during inverse Compton processes and Bremsstrahlung of electrons and proton-nucleon interactions. Satellite-based experiments are suitable for direct measurements of γ-rays, however, with γ-ray fluxes following the steep spectrum of cosmic rays at higher energies, larger detection areas are necessary. For indirect measurements of γ-rays the use of the atmosphere as detection medium for ground-based detectors is possible. Beyond energies of $\sim$100 GeV the Imaging Atmospheric Čerenkov Technique has proven to be very successful. It was pioneered in the late 1960s by the Whipple collaboration (Weekes et al. 1989) and makes use of the effect that each γ-ray hitting the Earth's atmosphere interacts with atmospheric particles and initiates a cascade of secondary charged particles. Those secondary particles that are travelling faster than the speed of light in the air emit Čerenkov light which reaches the ground. Due to the short lifetime of the traveling particles the Čerenkov light emission lasts only a few nanoseconds. Telescopes with a fast camera and sufficient mirror area can collect the faint light and image the shower, allowing to reconstruct the direction and energy of the primary γ-ray. The stereoscopic approach, pioneered in the 1990s by the HEGRA collaboration (Daum et al. 1997; HEGRA Collaboration et al. 1999) confirmed predictions for systems of Čerenkov telescopes made earlier by Aharonian (1993). It has been successfully applied in the following years by the H.E.S.S., CANGAROO, and VERITAS collaborations (Hinton 2004; Kubo et al. 2004; Weekes et al. 2002) and more recently by the MAGIC collaboration (Colin et al. 2009), improving the background reduction and the angular resolution and lowering the energy threshold of the detector. The Imaging Atmospheric Čerenkov Technique is a powerful technique for imaging γ-ray sources and obtaining energy spectra in the energy range of $10^{11} - 10^{14}$ eV. Since the detection of the pulsar wind nebula in the Crab nebula in 1989 (Weekes et al. 1989), more than 100 very-high-energy γ-ray sources have been detected.

Initially, supernova remnants were discovered in the radio waveband. Theoretical predictions about their visibility in γ-rays and the following detection of several galactic supernova remnants in very-high-energy γ-rays have contributed to the understanding of the acceleration of cosmic rays in shock fronts. Morphological studies of the supernova remnant RX J1713.7-3946 with the H.E.S.S. detector have shown the acceleration of particles beyond 100 TeV in the shell of the remnant (Aharonian et al. 2004). This result suggests that supernova remnants are potential cosmic ray accelerators. To support this hypothesis, a systematic study of the γ-ray signal from a large ensemble of known supernova remnants is necessary.

The present work summarizes the observations with the H.E.S.S. detector and the analysis results for over 200 supernova remnants known from radio observations. For all remnants listed in Green's radio supernova remnant catalog (Green 2009) lying within the field of view of H.E.S.S., an upper limit on the γ-ray flux or value of the γ-ray flux at the remnants' positions is given. The observational value is compared to theoretical predictions from a model proposed by Drury et al. (1994). This model predicts the very-high-energy γ-ray flux from a supernova remnant based on its characteristic parameters, which are the total supernova explosion energy, the density of the surrounding medium, the efficiency of the particle acceleration, and the distance of the remnant. On the one hand, using the experimental result, constraints on the ensemble of model parameters are given, considering the total supernova explosion energy, the cosmic ray acceleration efficiency, and the density of the surrounding medium. On the other hand, using the theoretical predictions, recommendations for follow-up observations with the H.E.S.S. instrument are given for supernova remnants with little exposure and a predicted flux being close to the observational limit. Furthermore the coincidence of supernova remnants with known H.E.S.S. sources is investigated and current flux measurements of the observed supernova remnants are compared with results obtained with the HEGRA detector.

The current setup of the H.E.S.S. detector allows for an energy threshold of ~100 GeV. In order to increase the sensitivity at lower energies and to improve the investigation of sources with steep spectra an extension of the H.E.S.S. detector is currently being built. The H.E.S.S. array, consisting of four Čerenkov telescopes, will be extended by an additional telescope, which will be located in the middle of the existing array. The much larger mirror area of the new telescope lowers the energy threshold of the detector down to ~30 GeV. This will allow for a better overlap in energy between space-based and ground-based detectors, as space-based instruments have reached an unprecedented angular resolution and energy reconstruction for γ-rays between 20 MeV and 300 GeV with the launch of the Fermi satellite (Ritz et al. 2007).

The coordination of individual telescopes providing data is done by the *Central Trigger System*. The upgrade of the detector to H.E.S.S. phase II requires an upgrade of the existing Central Trigger System. In this work necessary changes of the trigger electronics and test results are presented.

The general outline of the thesis is as follows:

- Chapters 2, 3 and 4 describe the experimental technique, the central trigger system of the H.E.S.S. instrument and the applied analysis procedure.
- In chapter 5, an introduction into supernova remnants and particle acceleration in shock fronts is given.
- The results of the systematic study on supernova remnants are presented and discussed in chapter 6.
- Chapter 7 summarizes the results of the work and gives an outlook on future work in this field.

2 The H.E.S.S. telescope system

The H.E.S.S. (**H**igh **E**nergy **S**tereoscopic **S**ystem) experiment is an array of four Imaging Atmospheric Čerenkov Telescopes (IACTs) standing at the corners of a square with a side length of ∼120 m. Together, the four telescopes form a powerful instrument which is designed to detect very-high-energy (VHE) γ-rays in the energy range between ∼100 GeV and ∼100 TeV. The full array, depicted in Figure 2.1, has been in operation since December 2003. The use of stereoscopy with IACTs together with excellent technical characteristics such as the 5° field of view, the angular resolution for single γ-rays of 5' and the precision of the source location of ∼20" have led to many exciting discoveries of galactic and extragalactic TeV γ-ray emission regions. The great success of the H.E.S.S. instrument is based on the IACT technique, which had been applied for the first time in the late 1960s by the Whipple collaboration and led to the detection of the first TeV γ-ray source in the Crab nebula (Weekes et al. 1989). In this chapter the experimental technique is described, beginning with the description of the IACT technique and further on showing parts of the H.E.S.S. telescopes.

Figure 2.1: The H.E.S.S. telescopes during daytime.

2.1 The IACT technique

As briefly described in the introduction, IACTs image the Čerenkov light which is generated in the atmosphere. The Čerenkov radiation is generated when a cosmic-ray particle enters the Earth's atmosphere. The incident particle interacts with atmospheric nuclei and creates an air shower of secondary particles. For high-energy γ-rays, Heitler (1954) introduced a simple model (illustrated in Figure 2.2), which is based on three assumptions: *(1)* The radiation length of electrons and the conversion length of photons are assumed to be equal. *(2)* Pair production and bremsstrahlung are the only processes creating secondary particles. *(3)* The energy is shared equally between secondary particles after

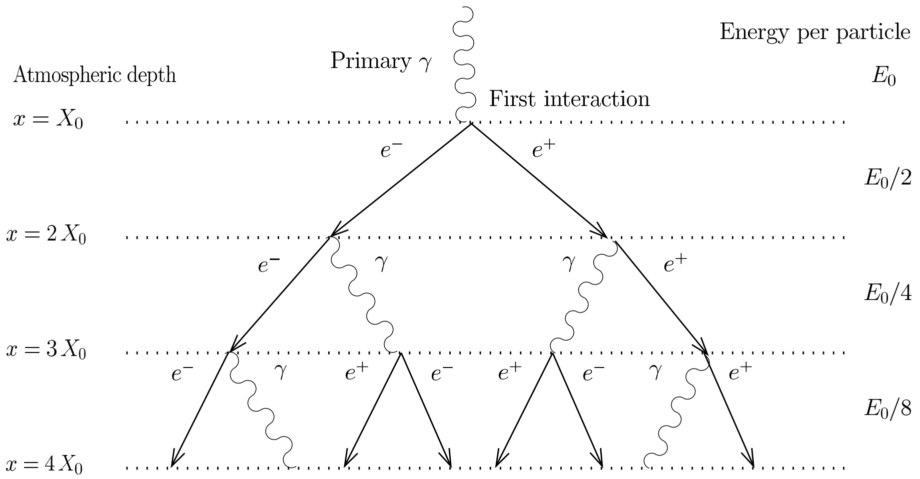

Figure 2.2: A simple shower modell suggested by Heitler (1954).

every interaction process. High-energy γ-rays entering the atmosphere with energies above ~30 GeV undergo multiple pair production. The resulting electron-positron pairs immediately generate further γ-rays via bremsstrahlung and lose energy by ionization. The secondary γ-rays undergo pair production until their energy drops below the rest mass of the resulting electron-positron pair $E = 2m_e c^2 = 1.022\,\mathrm{MeV}$. Hence the size of the whole air shower depends on the energy of the primary γ-ray. The relativistic electrons and positrons travel through the atmosphere at a speed greater than the speed of light in air and thus polarise nearby molecules. These emit prompt radiation in the visible part of the spectrum when depolarizing. This Čerenkov light travels through the atmosphere to the ground where it can be detected by imaging telescopes. The opening angle of the Čerenkov light cone depends on the speed of the electron or positron and therefore on the energy of the incident γ-ray and is given by $\cos\theta = \frac{v}{c}$. The maximum of the Čerenkov light emission is located at an altitude of ~10 km, the light cone thus covers an area with a diameter of about 250 m on the ground. An IACT situated within this area can collect Čerenkov light and take an image of the shower. The imaging of the shower is illustrated in Figure 2.3. The length and width of the image in the focal plane are proportional to the length and width of the shower.

The geographical location of the H.E.S.S. array in the Khomas Highland of Namibia about 1800 m a.s.l. is advantageous to minimize the absorption of the Čerenkov radiation in the atmosphere. Furthermore the distance to highly populated areas reduces light pollution. Measurements can only be taken during clear and moonless nights which allows for ~1000 h of observation per year. The great advantage of IACTs compared to space-bound detectors is the large collection area of $10^5\,\mathrm{m}^2$ using the Earth's atmosphere as the detection medium. With rapidly falling particle fluxes at high energies, space-bound detectors become inefficient due to their small collection areas of $\lesssim 1\,\mathrm{m}^2$.

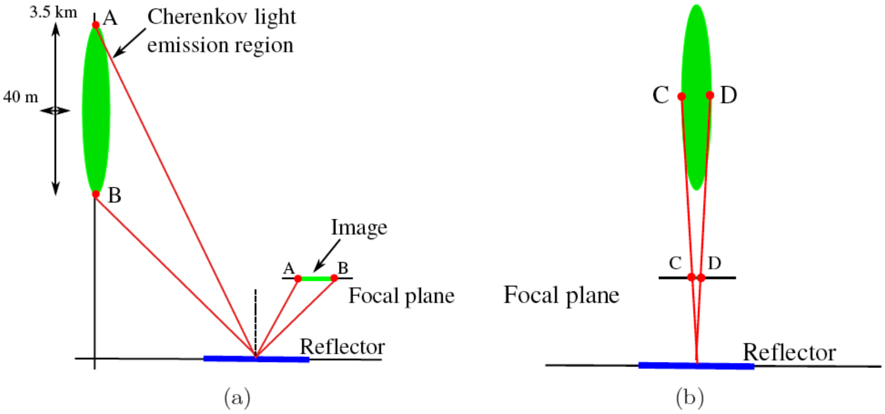

Figure 2.3: The detection principle of an Imaging Atmospheric Čerenkov Telescope. The length (a) and width (b) of the camera image are proportional to the length and width of the shower. The image has been taken from Hoppe (2008).

2.2 The H.E.S.S. telescopes

The H.E.S.S. telescopes are designed to perform reliably under extreme temperature and humidity conditions and without much maintenance. This section will briefly describe their technical and operational parts. One of the telescopes and a camera are shown in Figure 2.4.

2.2.1 Mount and dish

The H.E.S.S. telescopes use an altitude-azimuth mount. Each telescope can turn within an angle of more than 360° in the horizontal plane and has an angular range in elevation of more than 90°. Each pointing position in the sky can be reached within $\sim$2 min. The total reflecting area of each telescope amounts to $\sim$107 m^2. It is provided by 382 identical round mirrors with a diameter of $\sim$60 cm^2 each which are assembled in a Davies-Cotton design (Davies & Cotton 1957) with a focal length of $\sim$15 m.

2.2.2 Camera

The camera of each H.E.S.S. telescope (Vincent et al. 2003) is positioned in the focal plane of the reflector dish. Each camera contains a hexagonal array of 960 photomultiplier tubes (PMTs), the pixels. They are furnished with Winston cones (Winston 1970) which funnel the light into the PMTs, giving a nearly gap-less focal plane. Each pixel covers an area in the sky of 0.16°, which results in a total field of view of the detector of 5° (about 10 times the angular size of the moon). The small pixel size allows for a resolution of image details, whereas the large field of view permits to detect extended emission regions. The incoming Čerenkov light is translated into an electrical signal, which is sampled by a 1 GHz Analog Ring Sampler and stored in a 128 ns buffer. The pixels are grouped into overlapping sectors with 8×8 pixels each. The trigger condition for a single telescope

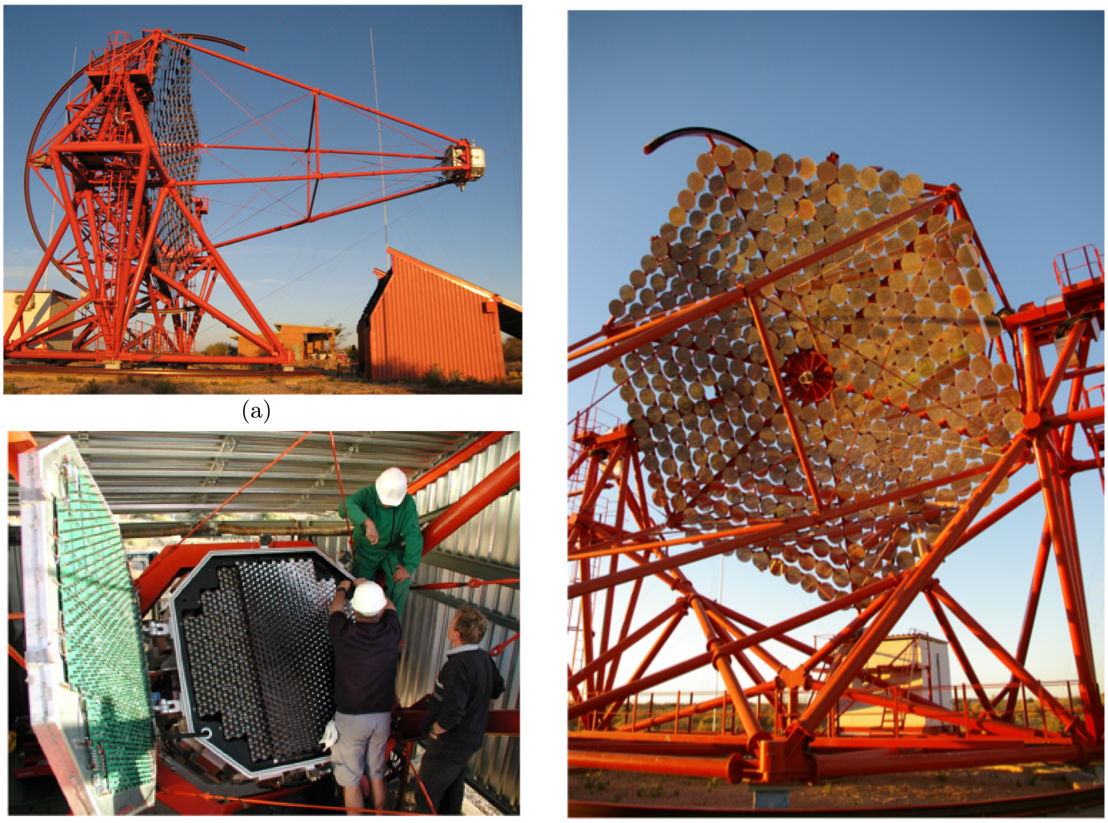

(a)

(b)

(c)

Figure 2.4: (a) One of the H.E.S.S. telescopes and its camera shelter (b) maintenance at the camera in the shelter (c) a closer look onto the mirror area. In (c) the lid camera is visible in the middle of the mirror area and a missing mirror at $\sim$ 9 o'clock in the photograph shows the position of the sky camera.

is fulfilled if the light yield exceeds 5 p.e. in at least 3 pixels in the same sector within 1.5 ns, thus rejecting uncorrelated PMT signals. In this case the ring buffer is stopped and a signal, an *active trigger* is sent to the *Central Trigger System* (CTS) (see section 3). If the telescope receives no response within 5 μs, the data is discarded and new data can be written to the buffer. While reading out data, the camera is still able to measure the light yield in the PMTs and send new triggers to the CTS including information on its readout status. These *busy triggers* do not contain any data and are used only for dead time calculations.

2.2.3 Operation

Knowing the exact pointing position of the telescopes while data taking is crucial for the analysis of the data. The apparent movement of the night sky as well as the weight-induced distortion of the steel structure make it necessary to constantly correct the pointing position of the telescopes. Therefore *pointing runs* are conducted, during which the light of a star with known position in the sky is projected onto the camera lid and compared to the image of LEDs, which are fixed at the telescope. This allows to derive a model for the correction of the telescope position. Details on the operating mode of the pointing are given in Bolz (2004) and Braun (2007).

The great advantage of the H.E.S.S. experiment is the use of stereoscopy by taking images of the same shower with multiple telescopes from different viewing angles. This allows to reduce the number of background events and to lower the energy threshold of the instrument. Therefore events detected simultaneously by individual telescopes are combined into one system event. The *central trigger system* is the electronical unit, which provides these system events and coordinates the individual telescope triggers. A detailed description of the central trigger system is given in Funk et al. (2004).

In the near future the H.E.S.S. array will be extended by a fifth Čerenkov telescope and thus upgraded to H.E.S.S. phase II. This requires an upgrade of the central trigger system, which has been prepared in the course of the present thesis. Technical details and test procedures of the central trigger for H.E.S.S. II are described in chapter 3.

3 The H.E.S.S. central trigger system

In the previous section the working principle of the IACT technique and the individual parts of the H.E.S.S. instrument have been presented. As already the Whipple detector has shown (Weekes et al. 1989), the IACT technique is fully functional with only one Čerenkov telescope. However, by using not only one image but a stereoscopic view of the air shower it is possible to reduce the background and to lower the energy threshold of the detector. This stereoscopic approach has first been successfully employed by the HEGRA detector (HEGRA Collaboration et al. 1999). The use of several simultaneous camera images requires a central unit, which coordinates individual telescope triggers and combines them to a system-wide event.

For the H.E.S.S. experiment the central trigger system (CTS) enables the use of stereoscopy. It finds coincidences between individual telescopes and creates a system event from these. The central trigger receives all individual camera triggers and decides which of them result from the same air shower. If at least two single-telescope triggers arrive within a short time window the coincidence condition is fulfilled. The central trigger generates a global event, stores the information about participating telescopes and sends *readout* signals to all telescopes providing data for this event. A readout signal includes a *count* pulse to increment the internal *event number*. Telescopes, which cannot provide data for the actual event, receive only the count pulse. The event number is stored within the central trigger as well as at the computer farm together with the camera data. It allows to coordinate data from individual telescopes and merge them later on. The CTS has been developed for phase I, the current configuration of the H.E.S.S. experiment. It is suitable for the use of up to 8 identical telescopes. A detailed description can be found in Funk et al. (2004).

The trigger rate of the individual Čerenkov telescopes is $\mathcal{O}$(400-800 Hz). Among those, the fraction of random triggers due to night sky background as well as single-telescope triggers resulting from muons is very high. Furthermore, the time to store the camera data associated to an event is up to 450 μs. If the data from all triggers were to be stored, the camera would be busy reading data most of the time and miss many γ-ray events. The use of stereoscopy has therefore proven to be very successful, as it removes single-telescope triggers already at the hardware level. Requiring the coincidence of at least two telescopes allows to reduce the rate of data storage by a factor of ~4 and to lower the energy threshold of the entire detector. The trigger threshold of a single telescope is related to the energy of the γ-ray and is defined by the number of illuminated pixels necessary for the detection of an air-shower. It has been shown by Funk et al. (2004) that this number and therefore the energy threshold of the individual telescope can be reduced when introducing a coincidence condition of at least two telescopes.

For phase II of the H.E.S.S. experiment a new telescope, CT 5, is currently being added to the existing array. Due to its larger mirror area of 600 m^2 air showers generated by γ-rays with energies down to ~50 GeV can be detected with this telescope, those events remain undetected by the other telescopes. To obtain data from γ-ray events of such low energies, single triggers from CT 5 are not to be rejected but should result in a system event with a readout of CT 5 and count pulses for all other telescopes. CT 5 will therefore be allowed to circumvent the coincidence requirement and generate single-telescope events at the level of the central trigger. With the γ-ray spectrum following the steep cosmic-ray spectrum, the trigger rate from CT 5 is expected to be much higher than for the H.E.S.S. phase I telescopes and can reach up to 5 kHz. An additional hardware-based threshold to reduce the data rate is implemented in the camera of CT 5, as described by Tluczykont (2005). It is based on a simple pattern recognition, which allows to exclude night sky background and hadronic background at a hardware level and to support γ-ray-induced air showers. The use of single-telescope events from CT 5 as well as multi-telescope events from the entire array requires changes in the hardware of the CTS. The present work describes the functionality of the CTS for the use within phase II of the experiment. Required changes and tests of the hardware as well as first test results are presented.

3.1 Trigger system phase I

This section briefly describes the characteristics of the CTS as used for phase I of the H.E.S.S. experiment. It consists of three main interacting parts, which are illustrated in Fig. 3.1. Each telescope camera contains the camera electronics and an interface module, which is connected to the central trigger electronics in the control building with two optical fibers. The central trigger receives all individual telescope triggers via the first fiber. If within 50 ns at least two telescopes trigger, the required coincidence condition is fulfilled and the central trigger assigns a unique event tag to the event and stores it together with a GPS time stamp and the pattern of the participating telescopes on an event-by-event basis in a FIFO memory. The information is later on used for book-keeping of events and dead-time calculations. Via the second optical fiber the central trigger distributes its decision to the interface modules of all telescopes. The signal from the central trigger includes two different transmission types. One is the readout decision including the count pulse for each event. The other signal is sent every ∼4 s and consists of a serial data word containing the *bunch number* and the *node number*. The node number changes from 0 to 20 and indicates the node on the computer farm where the data are to be stored after readout. Whenever a new bunch number is sent the event number is reset, ensuring the smallest possible event loss in case of confused event numbers.

The electronics of each camera continuously records the current induced by the light detected with the photomultiplier tubes (PMTs) and looks for connected pixels above a certain illumination, defined by the *sector* and *pixel threshold* (Vincent et al. 2003). If these thresholds are exceeded the camera sends a trigger signal to the interface module, consisting of a trigger pulse and the *busy level*, which signalizes that the camera has started the readout process. While the camera is in the process of storing data from a previous event, air showers can occur. Although no data of these events is available during this dead time, they have to be taken into account to correctly determine the total number of events during the accumulated observation time. Therefore the camera generates a *busy trigger*, which does not contain data but is counted as a valid camera trigger and can also fulfill the coincidence requirement.

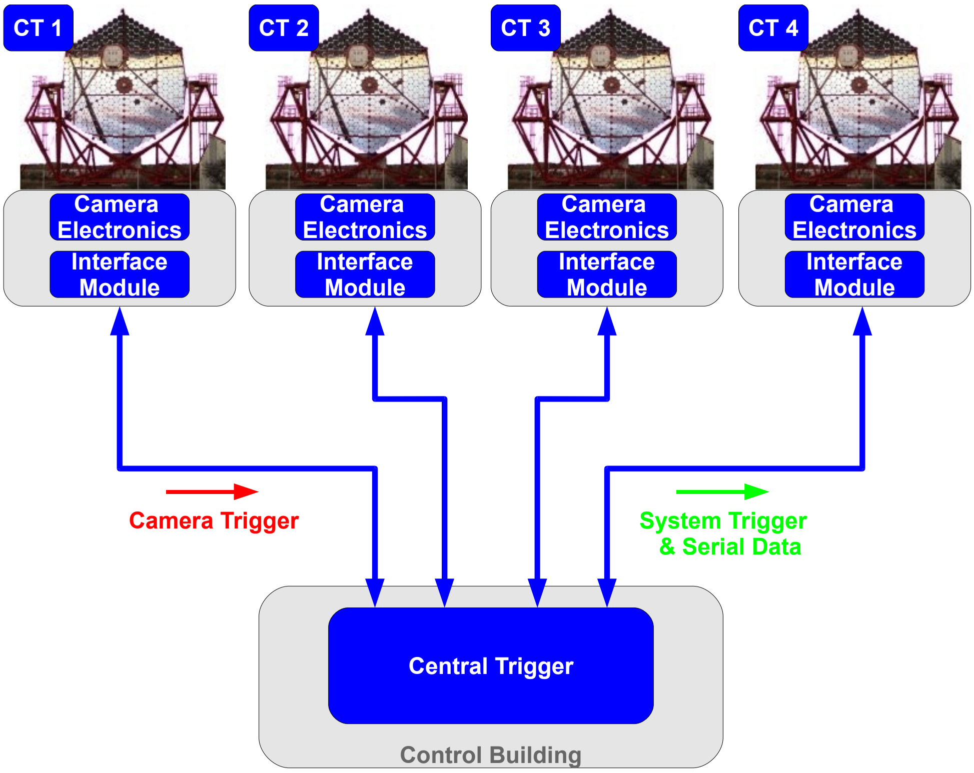

Figure 3.1: The central trigger system consists of the interface module, which is located in the camera and the central trigger electronics in the control building. Each interface module is connected with the central trigger via two optical fibers, one for sending camera triggers, the other to receive readout or count pulses and serial data containing the bunch and node number.

In the interface module each camera trigger is converted into a width-encoded pulse. The pulse width is of length 100 ns for an *active trigger*, when the camera can provide data for the actual event, and of length 50 ns for a busy trigger, when the camera is currently processing data from a previous event and cannot provide any data. This signal from the interface module is sent via optical fiber to the central trigger module where the central trigger decides whether the individual telescope triggers belong to the same event. This decision is taken based on the difference in arrival times of the individual telescope triggers, which has to be smaller than 50 ns. The optical pulses arriving at the central trigger are first converted into electrical pulses. Differences due to the azimuth-dependent arrival time of the Čerenkov light front at the respective telescope and due to differing lengths of the fibers between the telescopes and the control building are continuously adjusted by a programmable delay board. The final trigger decision is transmitted via the second optical fiber. Therefore the electrical pulses are reconverted into optical pulses and sent to the interface modules. If despite incoming camera triggers no valid coincidence has occurred, the central trigger does not generate an event and sends no pulses back to the interface modules. This results in the generation of a *fast clear pulse* by the interface module, stopping the data storage and causing the discard of the camera data. In case of a valid event, the central trigger generates width-encoded pulses. Readout pulses (following active triggers) have a length of 66 ns, whereas count pulses (following busy triggers) have a length of 33 ns, which keep the event number updated but do not lead to data storage. The entire process of the trigger decision from reception of the trigger pulse from the interface module until the generation of the readout or count pulse from the central trigger takes ∼300 ns. Table 3.1 summarizes the different pulse widths for the active/busy and readout/count pulses.

Table 3.1: Pulse widths for trigger pulses.

Pulse	Width
active camera trigger	100 ns
busy camera trigger	50 ns
readout from central trigger	66 ns
count from central trigger	33 ns

Signal path

The path of the individual camera triggers is illustrated in Fig. 3.2. The Čerenkov telescopes CT 1-4 generate trigger pulses, which are transmitted by the interface modules to the central trigger, where they are converted into digital pulses and delayed according to the actual telescope pointing. With two simultaneous triggers the lookup table generates coincidence, further telescopes are added to the trigger pattern and after re-converting the pulses into optical signals, they are sent back to the individual telescopes.

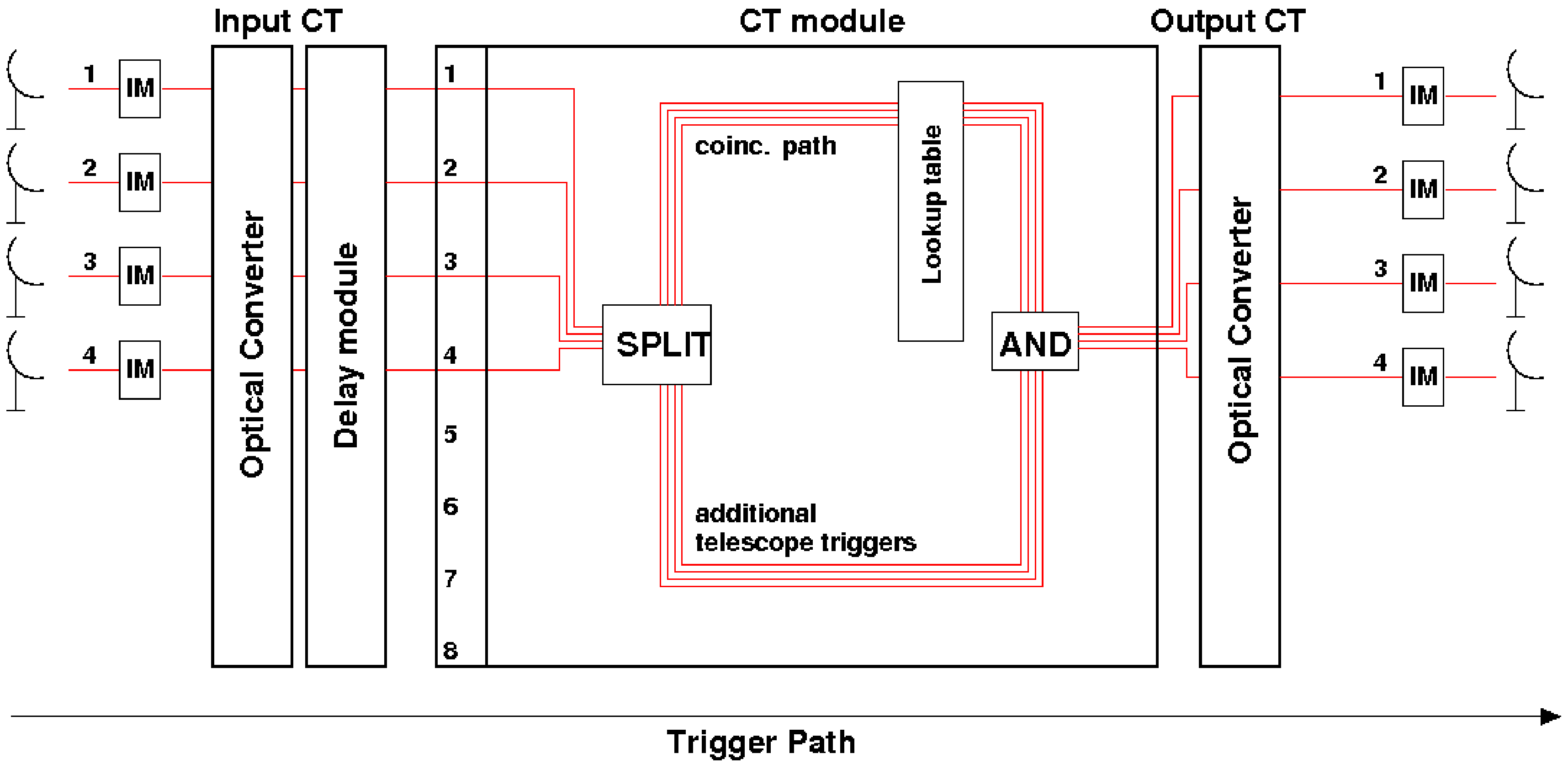

Figure 3.2: The schema illustrates the path of camera triggers within H.E.S.S. phase I. The lines highlighted in red represent the trigger channels for the telescopes. The triggers arrive from the individual telescopes, go through the trigger decision chain of the central trigger module and are returned to the telescopes. The interface modules (IM) transmit pulses between the cameras and the central trigger.

Trigger example

An example of the pulses generated by the camera, the interface module and the central trigger for both an active and a busy trigger is illustrated in Fig. 3.3. The oscilloscope image illustrates two consecutive trigger signals from the same camera, one active and one busy trigger. The first part of the image (first pulse of each color) illustrates the pulse sequence of an active pulse including the camera readout, whereas the second part of the image illustrates the busy trigger, which ends with the count pulse from the central trigger and does not result in a camera readout. The pulses shown in Fig. 3.3 and generated by the different parts of the CTS are highlighted by colors.

- Green marks the busy level, which is raised as long as the camera is busy with data storage of a previous event.
- Magenta indicates the trigger pulses generated by the camera electronics and from there sent to the interface module.
- Blue represents the width-encoded pulses sent from the interface module to the central trigger: in case of an active event 100 ns pulses are generated and in case of a busy event the pulse width is of 50 ns.
- Red marks the width-encoded pulses generated by the central trigger and sent back to the interface module: a *readout* pulse is of width 66 ns, whereas the pulse width of a *count* pulse is of width 33 ns, which only keeps the event number updated but does not lead to data storage.
- Yellow indicates the translation of the trigger decision into a readout pulse in the interface module. In case of a count pulse from the central trigger, the interface does not generate any signal, whereas a readout pulse of the central trigger results in a readout pulse to the camera.

Coincidence decision

The coincidence decision of the CTS is based on a multiplicity requirement, requesting at least two telescopes to trigger within a given time window. The programmable duration of this time window and the number of required telescopes are stored in a central database and are read during initialization of the CTS. Currently a time window of 50 ns is used, during which the coincidence condition has to be fulfilled. If no other telescope triggers within this time window after a trigger from one of the other telescopes was received, the trigger is ignored by the CTS and no readout or count signal is generated. After 4.5 μs, dictated by the roundtrip time between the telescopes and the control building, the interface module generates a fast clear signal, which clears the camera buffer. This signal stops the data storage process and allows the camera to take new data. If, however, within the time window another telescope sends a trigger (which can be active or busy) the coincidence condition is fulfilled and a second time window of again 50 ns duration is opened in the central trigger. All telescopes sending active triggers within this second time window can participate in the same event and also receive readout pulses.

In case of a valid event (i.e. when the coincidence is fulfilled within the first coincidence window) the central trigger stores an absolute time stamp (provided by a GPS clock with a

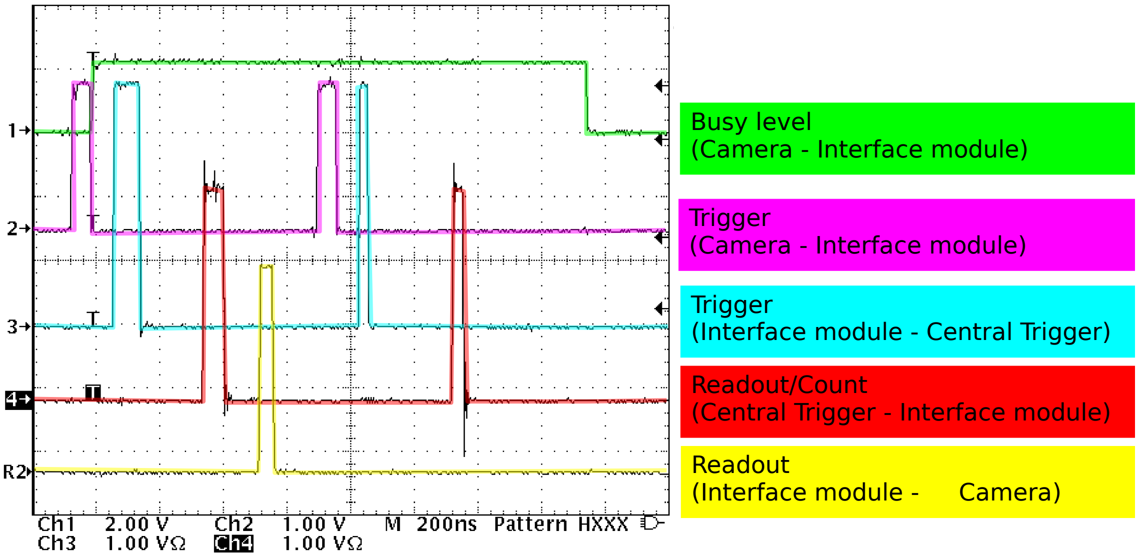

Figure 3.3: The oscilloscope image illustrates the sequence of pulses in the trigger system of a valid multiplicity-1 event for an active and a busy camera trigger. In case of an active trigger (first pulse in magenta) the central trigger generates a readout pulse (first pulse marked in red) and in case of a busy trigger (second pulse in magenta and the raised busy level in green) the interface module receives a count pulse (second pulse in red). The readout pulse is forwarded to the camera (yellow pulse), whereas the count pulse is not.

precision of 100 ns), the pattern of participating telescopes, and the global event tag on an event-by-event basis in a FIFO memory. The event tag consists of an *event number*, which is increased for each event and a *bunch number*, which is increased every ∼4 s together with a reset of the event number. When the interface module receives a readout pulse from the central trigger it internally stores the event tag and writes it to an *output register* from where the information is retrieved by the camera. In case of a count pulse for a busy telescope, the serial data is only stored internally in the interface module but not latched to the output register.

Importance of the busy level

The setup of the CTS currently operational in Namibia correctly generates all necessary pulses. When conducting tests of the central trigger in a laboratory, it is important to simulate not only camera triggers but also to take into account the readout time of the camera of ∼450 μs. An active trigger from the camera consists of the trigger pulse and the busy level, which is raised as long as the process of data storage takes. It is essential for the camera to always raise the busy level together with a trigger pulse because a missing busy level leads to a fast clear pulse and final rejection of the data despite a valid event. Figs. 3.4 (a) and (b) illustrate the pulse sequence of two consecutive events. In (a) the busy level has been raised by the first camera trigger (analog to Fig. 3.3), whereas in (b) the busy level is missing. In the second case the fast clear pulse (highlighted in orange) is generated in the interface module. It stops the actual data storage and discards the camera data. The time interval presented in Fig. 3.4 is of 10 μs, whereas Fig. 3.3 shows a time window of 2 μs only.

Dead time

The dead time describes the time during which the telescope cannot take data and is “blind” for air showers. The higher the readout rate of a telescope is, the higher is its dead time. The coincidence condition as well as pixel and sector thresholds set by the camera hardware help to keep the dead time at an acceptable value. The current dead-time fraction is about 10 %. The dead time results from two different effects. The *single-telescope dead time* is the fraction of time during which one camera has detected an air shower but is busy reading out data from a previous event. This time is 446 μs and results from the digitization and transfer of the camera data to a global FIFO memory. The *central-trigger dead time* is the time during which the central trigger is occupied processing the previous event and ignores new incoming camera triggers. This time window results from the trigger decision and the storage of the serial data in the local FIFO memory. It amounts to 330 ns and is negligible compared to the single-telescope dead time. The combined *system dead time* can be estimated by the fraction of system triggers with only busy telescopes and is used to correct the measured event rate resulting in the real event rate during data taking.

3.2 Trigger system phase II

The CTS is designed such that an extension of telescopes of the same type is possible without changes of the central trigger module. However, the operation of a larger Čerenkov telescope, which one wants to read out independently of a coincidence with one of the other telescopes, requires an upgrade of the CTS.

The requirements for the upgrade of the CTS include

- ensuring the trigger system functionality at high trigger rates,
- allowing single-telescope events to be accepted from CT 5 and initiating the readout of CT 5 only, including the activation of the additional hardware threshold in CT 5,
- accepting multi-telescope events from arbitrary combinations of all five telescopes excluding the activation of the second-level trigger.

The CTS of H.E.S.S. has been designed for trigger rates of up to 10 kHz, which is sufficient also for phase II. Within this thesis, the functionality of the central trigger for H.E.S.S. phase II has been tested employing statistically distributed camera triggers at high rates to ensure the operation of the detector with the expected trigger rates of CT 5.

The acceptance of single-telescope events from CT 5 is not straightforward and requires changes in the central trigger module. For the updated central trigger module the coincidence condition of at least two camera triggers is still valid for phase II of the experiment. However, if CT 5 is the only telescope sending a trigger within the coincidence time window the central trigger shall still generate a system event, a *mono event* in this case, and send a readout pulse to CT 5 only. Together with this readout signal, all other telescopes

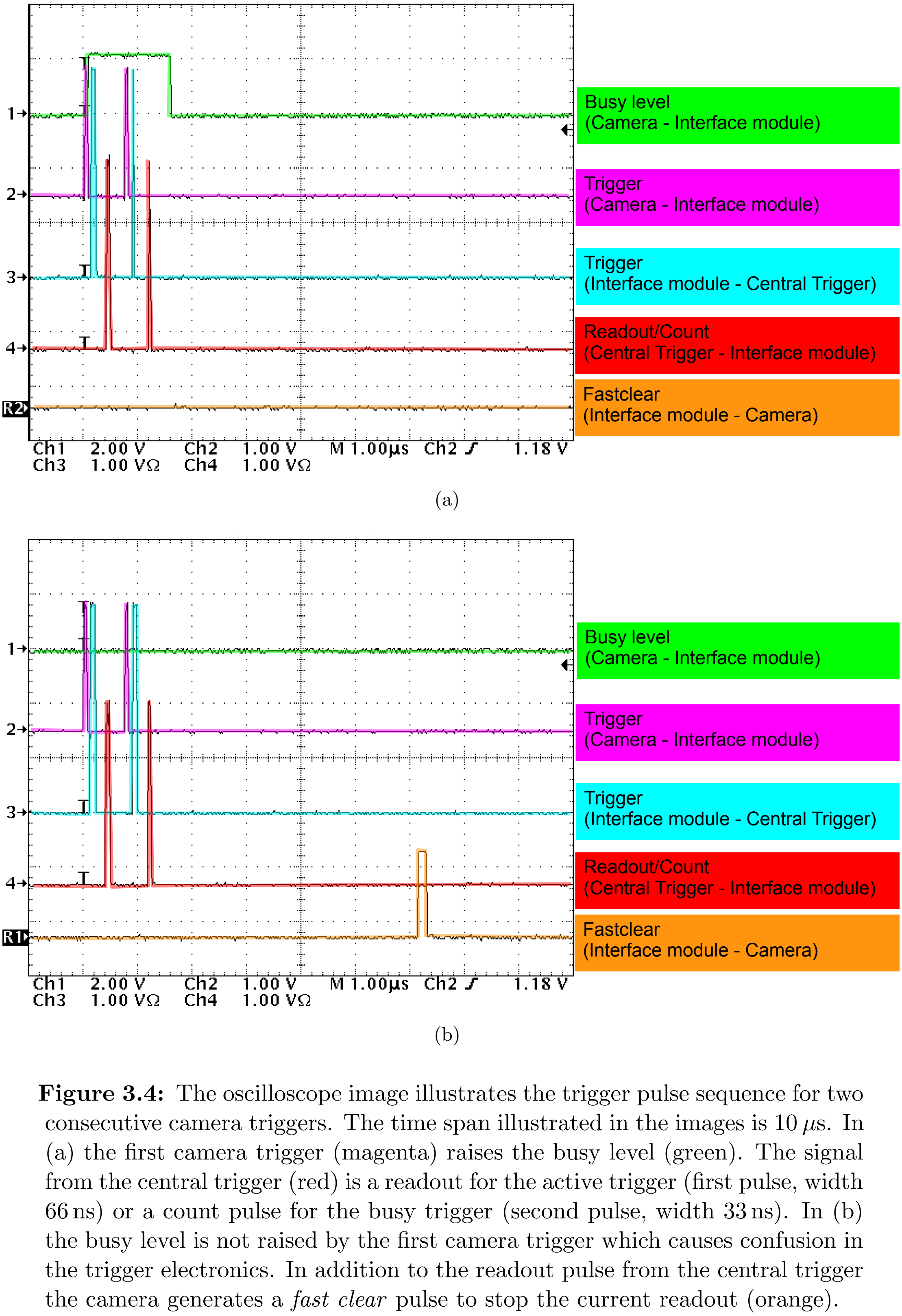

Figure 3.4: The oscilloscope image illustrates the trigger pulse sequence for two consecutive camera triggers. The time span illustrated in the images is 10 μs. In (a) the first camera trigger (magenta) raises the busy level (green). The signal from the central trigger (red) is a readout for the active trigger (first pulse, width 66 ns) or a count pulse for the busy trigger (second pulse, width 33 ns). In (b) the busy level is not raised by the first camera trigger which causes confusion in the trigger electronics. In addition to the readout pulse from the central trigger the camera generates a *fast clear* pulse to stop the current readout (orange).

receive a count pulse to keep the event numbers synchronized. In case of such a mono event, the readout signal for CT 5 activates the *second-level trigger* in the camera of CT 5. This second-level trigger is the additional hardware threshold implemented in the camera of CT 5 selecting events based on the quality of the camera image and hence reducing the data storage rate and the dead time of CT 5. The second-level trigger performs a quick parametrization of the camera image and compares the values to those obtained from Monte-Carlo simulations. Images resulting with high probability from night sky background or hadron-induced air showers are rejected.

The activation of the second-level trigger requires the additional signal sent to CT 5. Within the trigger logics it is not possible to simply generate an additional readout signal for the second-level trigger but the output signal can only be generated after an incoming signal. Therefore, the trigger pulse of the CT 5 camera is split into two identical pulses at the input of the trigger module. Both pulses are considered as single-telescope triggers within the central trigger module. This allows to fulfill the coincidence condition with an active trigger from CT 5 alone. Thus, in case of a mono event, both CT 5 channels receive a readout pulse. One of the pulses is used for the readout of the camera data from CT 5. The other is transmitted to CT 5 via an additional optical fiber, which connects the central trigger and an additional interface module in CT 5. Whenever a mono event occurs, a readout signal is sent via both optical fibers, one activating the data storage, the other activating the second level trigger in CT 5. In case of a *stereo event*, however, including at least two telescopes, the second-level trigger is not to be activated and the additional interface module in CT 5 must receive a count pulse only.

The trigger decision taken in the central trigger is based on a programmable *lookup table* including all possible combinations of individual telescope triggers, which is filled during the initialization of the central trigger. The use of the CTS with H.E.S.S. phase II requires changes of this lookup table in order to allow CT 5 mono events as well as stereo events with or without CT 5. However, the generation of mono events does not only require software changes in the lookup table, but also hardware changes of the central trigger electronics. As described earlier, the coincidence is fulfilled when a second telescope sends a camera trigger within 50 ns after the first trigger. All additional telescopes sending triggers are simply added to the event without again checking the lookup table for valid coincidence. This causes a problem for H.E.S.S. phase II. If CT 5 triggers as a third telescope, the coincidence has already been fulfilled by two other telescopes. Therefore both trigger signals from CT 5 are added to the event and receive readout pulses. One of these readout pulses is correct, since it starts the data storage of CT 5. The second pulse, despite the stereo event, also receives a readout pulse, which activates the second-level trigger during this stereo event. This has to be prevented and for stereo events a count pulse only must be sent to the additional interface module of CT 5. The distinction between mono events and stereo events including CT 5 can be accomplished by different possibilities. One of them is the integration of a XOR gate in the circuit of the central trigger electronics. It tests the readout pulses which are to be sent to all telescopes. If CT 5 together with any H.E.S.S. phase I telescope participate in the same event and are scheduled for a readout pulse, the XOR gate discards the readout pulse of the additional interface module of CT 5 and turns it into a count pulse.

Fig. 3.5 illustrates the chain of pulses from the camera trigger until the readout or count pulse. The pulses (marked in red) from all telescopes are converted into electrical signals and delayed according to their respective elevation. When entering the central trigger module, the trigger from CT 5 is split up into two pulses, which further on act like individual camera triggers. Within the central trigger module, all signals follow two paths: one goes through the lookup-table, where at least two trigger pulses have to arrive within the first time window of 50 ns to fulfill the coincidence condition. If this is the case, all additional telescopes which arrive within the second time window of 50 ns are added to the telescope pattern (illustrated by the logical AND). To distinguish between CT 5 mono events or stereo events an additional logical XOR tests whether other than the two CT 5 pulses participate in the event. If only CT 5 triggered, the additional interface module in the CT 5 camera receives a readout. If any of the other telescopes participate in the event, only one readout pulse is sent to CT 5 and the additional interface module receives a count pulse.

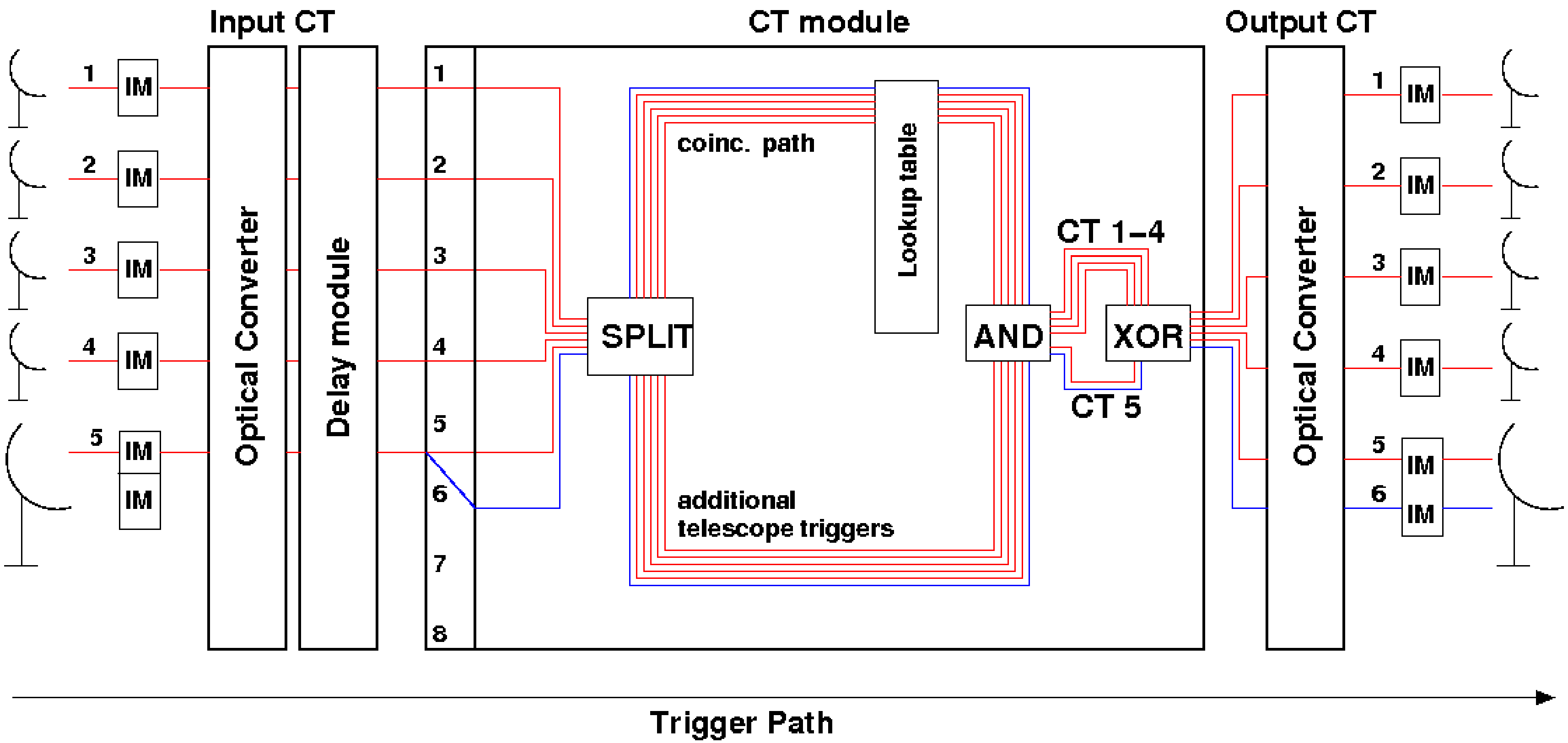

Figure 3.5: The schema illustrates the path of camera triggers within H.E.S.S. phase II. The lines highlighted in red represent the channels for the camera triggers of the telescopes CT 1-5, whereas the line highlighted in blue represents the channel used for the additional interface module of CT 5, which activates the second-level trigger. The triggers arrive from the individual telescopes, go through the trigger decision chain of the central trigger module and are returned to the telescopes. The interface modules (IM) transmit pulses between the cameras and the central trigger. The final readout pattern (after the lookup-table) is tested for stereo events by the XOR, which would discard the readout pulse of the additional CT 5 channel.

3.3 Tests for the central trigger upgrade

Within this thesis the central trigger has been tested under circumstances which are expected to be realistic for the operation of the full array including CT 5. The tests include the stability of the trigger system at high trigger rates and for statistically distributed triggers and different telescope trigger patterns for stereo events as well as for mono events. Interface tests with a camera module from a H.E.S.S. I camera and a prototype camera module for CT 5 have been conducted. The test setup simulates the complete trigger chain using exact copies of the modules employed on site including the interface module, the optical converter module, the delay module and the central trigger module. Camera triggers are generated by a frequency generator or by statistically distributed pulses from a PMT.

3.3.1 Stability at high frequencies

The functionality of the central trigger module has been tested up to frequencies of up to 10^6 Hz. At these high trigger rates the central trigger module works as designed and returns correct trigger decisions analog to Fig. 3.3. For tests, where serial data (event, bunch and node number) are stored to disk eventwise and the speed of file access is limited, lower frequencies of $\mathcal{O}(10^3\,\mathrm{Hz})$ are used. During the tests, the serial data from the central trigger FIFO memory as well as from the interface module are stored to disk and tested for synchronization. The real camera data, however, cannot be simulated with the used setup.

During operation of the detector it is essential that the serial data is synchronized between the central trigger module and the camera electronics at all times, otherwise the camera data cannot be merged and is unusable. Therefore interface tests have been conducted between the central trigger on one side and the interface module and camera electronics on the other side. During the tests triggers at a rate of $\sim$3 kHz have been generated by a prototype of the camera module of CT 5. This module has been provided by H.E.S.S. collaborators from the institute LPNHE in Paris, where the CT 5 camera has been designed and built. During the tests two CPUs manage the data flow and initiate the readout of the serial data from the FIFO memory in the central trigger module and from the camera module. As a result, two data files are written: one containing the serial data from the central trigger FIFO memory and the other containing the serial data from the camera module.

The interface tests have shown that the serial data stored in the camera module of CT 5 correspond to the data stored in the central trigger FIFO memory for trigger rates of up to 1 kHz but are corrupt when using higher trigger rates of $\sim$3 kHz. This is due to the limited speed of the camera module reading the serial data from the interface module or writing the data to the file. This explanation is supported by cross-checks realized with a camera simulator module, whose serial data match the central trigger data at all tested frequencies. The solution to this problem requires hardware changes of the electronics within the camera module, which are currently being implemented but could not be tested during the time of this thesis. Therefore further interface tests to prove the correct functionality of the entire CTS will be necessary before commissioning of CT 5.

3.3.2 Acceptance of mono and stereo events

As mentioned earlier, the idea for the generation of mono events within the CTS is to use an additional channel on the central trigger module for the monobit, which activates the second-level trigger in the camera of CT 5. Altogether the operation of H.E.S.S. phase II allows three different event classes, which have to be tested after completing the update of the trigger module:

- H.E.S.S. phase I stereo event
- H.E.S.S. phase II mono event
- H.E.S.S. phase II stereo event

These event classes will be described in the following, discussing required changes in the trigger electronics.

H.E.S.S. phase I stereo event

This event class includes individual telescope triggers from at least two H.E.S.S. I telescopes. It represents the current setup of the H.E.S.S. array. Tests have shown that the CTS shows the expected behavior. Therefore this event class is not further discussed here.

H.E.S.S. phase II mono event

Contrary to single triggers from H.E.S.S. I telescopes, single triggers from CT 5 are not to be rejected but should result in a system event with a readout of CT 5 and count pulses for all other telescopes. However, the central trigger does not distinguish between triggers received from H.E.S.S. phase I telescopes and triggers from CT 5 on an electronics level and would, using the current design of the trigger module, also reject CT 5-only triggers. This rejection is avoided by splitting the input signal of CT 5 into two independent signals and applying both as independent triggers to the lookup table, thereby occupying an unused channel of the 8 possible trigger channels of the central trigger module. Thus CT 5 alone evokes coincidence and generates a valid event, which results in readout pulses for both splitted CT 5 channels and count pulses for all other telescopes. The two CT 5 readout pulses are then forwarded separately to the camera of CT 5: one supports the data storage of the mono event, whereas the other activates the second-level trigger. During tests this behavior could be verified during tests with the CTS and mono triggers from CT 5.

H.E.S.S. phase II stereo event

While the generation of a mono event requires only the splitting of the input signal of CT 5, the necessary changes of the central trigger electronics are more substantial when also considering stereo events with CT 5. This new event class includes at least one H.E.S.S. I telescope together with CT 5. It is essential that for phase II stereo events the second-level trigger in the camera of CT 5 is not activated. As pointed out earlier, telescopes triggering during the second time window of the central trigger are simply added to the event without further consideration of the lookup table and also receive readout pulses. At the time of completion of this thesis the correct handling of H.E.S.S. phase II stereo events could not be achieved and further tests are necessary.

Fig. 3.6 shows three different scenarios of H.E.S.S. phase II stereo events, which illustrate the problematics of the monobit generation for stereo events. Using the current design of the central trigger electronics a phase II stereo event would be generated together with a monobit in all three cases, thus activating the second level trigger. In (a) the coincidence is fulfilled by CT 1 and CT 2. The incoming CT 5 trigger arrives during the second time window and, since the lookup table is not further considered in this case, both CT 5 channels receive a readout and hence the second-level trigger is activated. In (b) the result is the same, but here the coincidence is fulfilled by CT 1 and CT 5. Also (c) results in the activation of the second-level trigger, as the coincidence is fulfilled by the splitted signals of the CT 5 trigger and CT 1 is added to the event. Thus, both channels of CT 5 as well as the CT 1 channel receive readout pulses.

To solve this problem different approaches have been investigated. The solution suggested from these investigations is the implementation of an XOR operation (exclusive or), which is to be applied to the final readout pattern, including all channels of CT 1-4 and the two pulses generated for CT 5, as illustrated in Fig. 3.5. This allows to distinguish between CT 5 being part of a stereo event or representing a mono event. In case of a mono event the output of the XOR gate would be two readout pulses for CT 5 and count pulses for all other telescopes. In case of a phase II stereo event the output would be a readout pulse for the CT 5 data channel, a count pulse for the CT 5 second-level trigger and readout or count pulses to all other telescopes according to their participation in the event.

3.4 Conclusion

The implementation of the CTS allows the use of stereoscopy, which reduces the dead time of the individual cameras and lowers the detector's energy threshold. The use of the CTS during H.E.S.S. phase II requires changes on the hardware and software level of the central trigger. With the operation of the new telescope, CT 5, not only stereo events with at least two telescopes are allowed, but also mono events with data from CT 5 only. Within this thesis the general functionality of the CTS has been tested and confirmed. The upgrade of the central trigger including necessary changes has been prepared. For the correct generation of mono and stereo events with H.E.S.S. phase II a solution has been suggested, requiring an XOR operation in the central trigger module. Further steps are interface tests with the camera of CT 5 and confirmative tests of the mono and stereo event generation according to the developed solution.

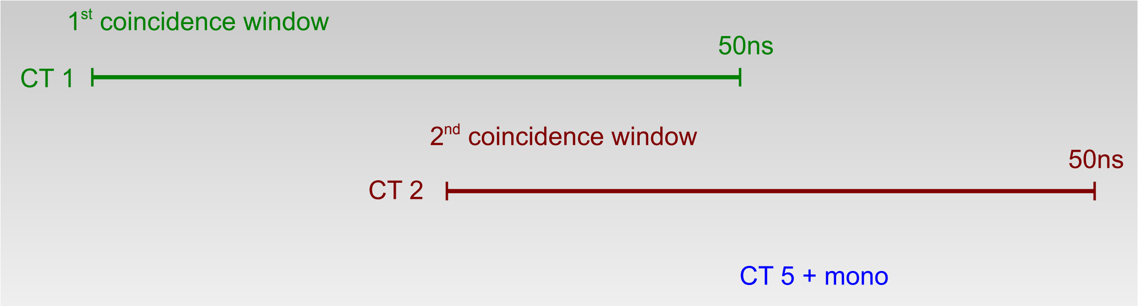

(a) At least two H.E.S.S. I telescopes trigger first, CT 5 triggers during the second coincidence window. Using the current setup of the central trigger, a wrong monobit is generated.

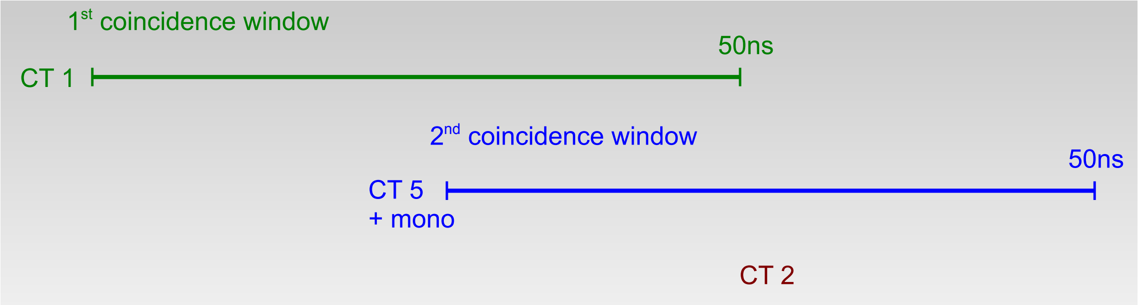

(b) A H.E.S.S. I telescope triggers first, CT 5 triggers during the first coincidence window.

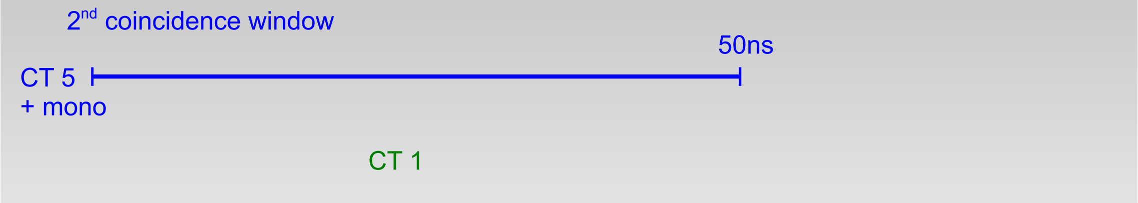

(c) CT 5 triggers first and immediately fulfills the coincidence requirement, any H.E.S.S. I telescope triggers during the second coincidence window. This scenario also results in a wrong monobit.

Figure 3.6: Illustration of possible trigger scenarios, which result in a H.E.S.S. II stereo event but at present activate the second-level trigger in CT 5. In the images CT 1 and 2 have been used as examples for H.E.S.S. I telescopes.

4 The H.E.S.S. data analysis

To determine whether a region in the sky emits VHE γ-rays the images of the Čerenkov light showers have to be analysed. The raw image recorded with the Čerenkov telescopes only contains information about the charge generated in the photomultiplier tubes (PMTs) of the cameras, integrated over the readout time window and converted into a digital signal. To extract the direction and the energy of the incident γ-ray, an analysis procedure has to be applied. First, the charge values are converted by a calibration procedure into the number of photoelectrons (p.e.) generated by a recorded event. The resulting camera images are cleaned, γ-ray-like events selected, and background events rejected based on the shape of the images. This allows to reconstruct individual air showers. The source spectrum is derived from the number and energy of signal and background events. The main steps of the analysis procedure are described in this chapter, following Aharonian et al. (2006a).

4.1 Image parametrisation and direction reconstruction

A cleaning procedure is applied to the shower images excluding pixels with signals caused by night sky background or electronic noise in the PMT. This is achieved by a cut on the minimum intensity recorded in a pixel: the camera image is reduced to pixels with at least 10 p.e. that have a neighbouring pixel with at least 5 p.e. and vice versa. The remaining image of a γ-ray-induced air shower can be approximated by an ellipse and is parametrised using six parameters suggested by Hillas (1985). These are the centre of gravity, the length of the major and minor axes, the orientation and the size of the image, i.e. the total number of p.e. in the cleaned image. Figure 4.1 exemplarily shows the parametrisation of two ellipses measured from a single shower in two different telescopes. The shape of the shower images depends on the zenith angle of the shower, its distance to the telescope, its offset from the camera centre, and the energy of the primary particle, which initiates the particle cascade.

The direction of the incident particle can be reconstructed using the orientation of the Hillas ellipse. The directional ambiguity is broken by the stereoscopic approach as used by the H.E.S.S. instrument. Thereby not only one ellipse is parametrised but all shower images are considered in a common coordinate system. The intersection of the individual major axes allows to reconstruct the origin of the incident particle and the impact position of the shower core on the ground.

Using Monte Carlo simulations with given direction of origin the accuracy of the reconstructed direction can be determined, which defines the *point spread function* (PSF) of the instrument. For observation angles close to zenith, the PSF of the H.E.S.S. array is $\sim$0.1 °. To ensure an accurate reconstruction of the total light yield and thus of the energy of the incident VHE γ-ray, the *impact parameter* has to be reconstructed. It is defined as the distance between the shower impact point on the ground and the camera centre. For

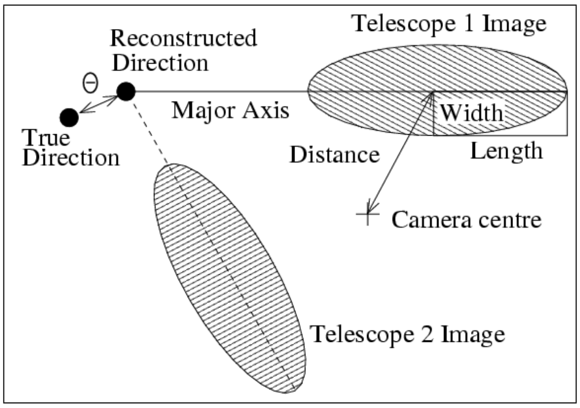

Figure 4.1: Sketch illustrating the Hillas parametrisation of a γ-ray-induced air shower detected in two telescopes. Width and length as well as the distance between camera centre and centre of gravity are later used in the analysis to select γ-ray-like events. Intersecting the major axes in a common coordinate system allows to reconstruct the shower direction on the sky as well as the shower impact point on the ground. The image has been taken from Aharonian et al. (2006a).

showers that are within a radius of 200 m of the centre of the array the accuracy of the impact parameter is ~10 m.

4.2 Event selection

For the detection of a VHE γ-ray-signal from a certain position in the sky it is crucial to determine the level of γ-ray-like cosmic ray background at the source position. For the raw data the signal-to-noise ratio is above $1 : 10^4$. The background is mainly due to air showers generated from charged particles, like protons, heavy nuclei, electrons and positrons. However, not all air showers look identical due to different interaction processes taking place in the atmosphere. While electrons, positrons, and VHE γ-rays generate purely electromagnetical air showers, protons aand heavier nuclei have a larger scattering cross section and induce extensive air showers (EAS) with electro-magnetical subshowers mainly from π^0 decay leading to an irregular shape of the camera image compared to a VHE γ-ray-induced event. Figure 4.2 shows the difference between a VHE γ-ray event with an energy of 300 GeV and a proton with an energy of 1 TeV.

To select γ-ray induced air showers and suppress hadron-like events various selection cuts are applied to the image parameters. A *size cut* is applied as a minimum required total image amplitude, a *nominal-distance cut* suppresses events with images only partly contained in the camera. In order to use stereoscopic reconstruction at least two telescopes have to fulfill these requirements for each event. The width and length parameters can be used to suppress the numerically dominant hadronic events. As explained by Aharonian et al. (2006a), a cut is applied on the *mean reduced scaled width / length* (MRSW, MRSL). Thereby the measured width W and length L of the shower images are compared to the expected values from γ-ray Monte Carlo simulations, $\langle \mathrm{W} \rangle$ and $\langle \mathrm{L} \rangle$, generated with the

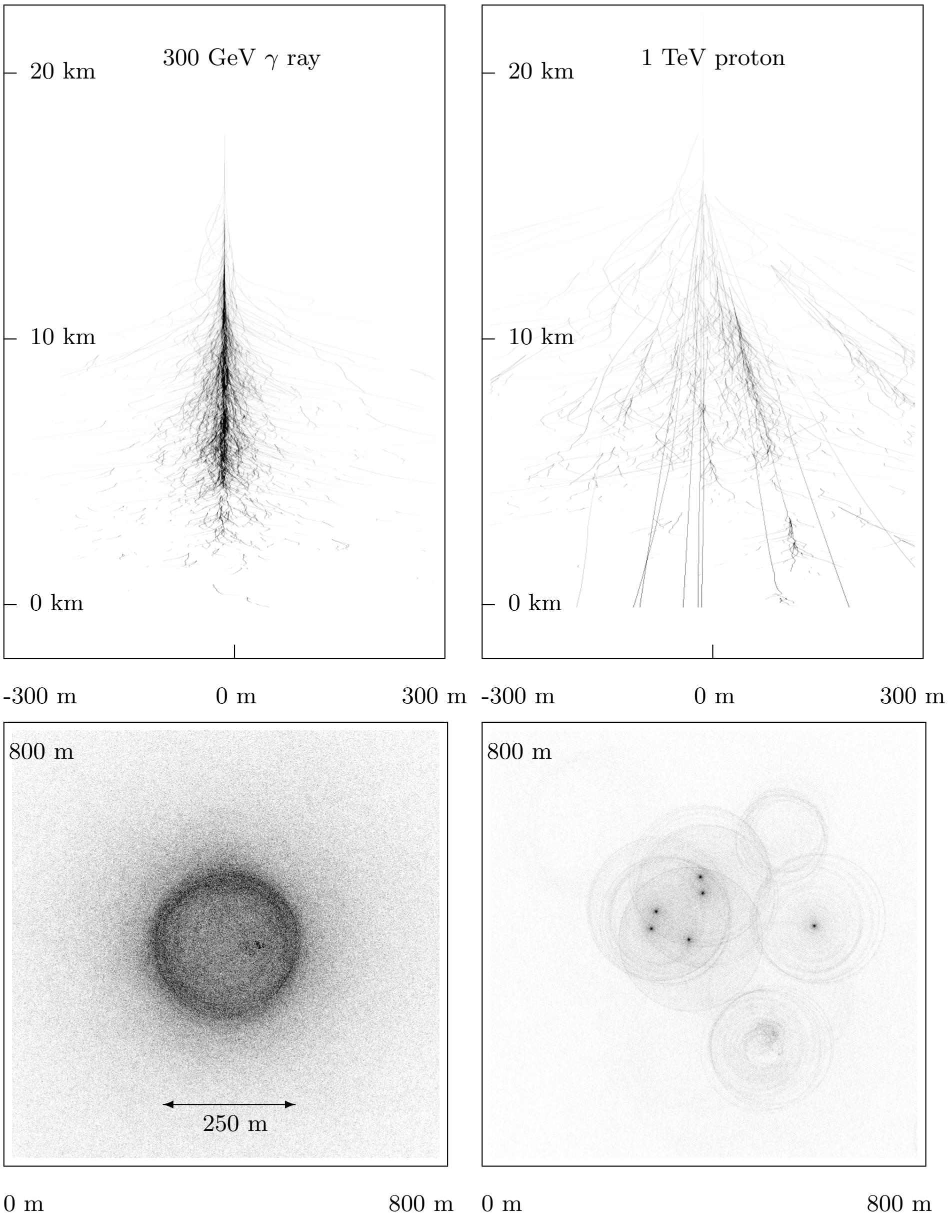

Figure 4.2: Lateral and longitudinal projections of air showers induced by a VHE γ-ray with an energy of 300 GeV on the left side and a proton with an energy of 1 TeV on the right side (by courtesy of K. Bernlöhr).

same image amplitude, impact point, zenith angle and offset from the pointing direction. The difference is given in units of standard deviation σ_w and σ_l. A weighting factor ω_i defined as $\omega_i =< W_i >^2 / \sigma_i^2$ is used to average over participating telescopes i. The MRSW is given by

$$\mathrm{MRSW} = \frac{1}{\sum\limits_{i=1}^{N_{tel}} \omega_i} \cdot \sum_{i=1}^{N_{tel}} \left(\frac{W_i - \langle W \rangle_i}{\sigma_{w,i}} \cdot \omega_i \right) \tag{4.1}$$

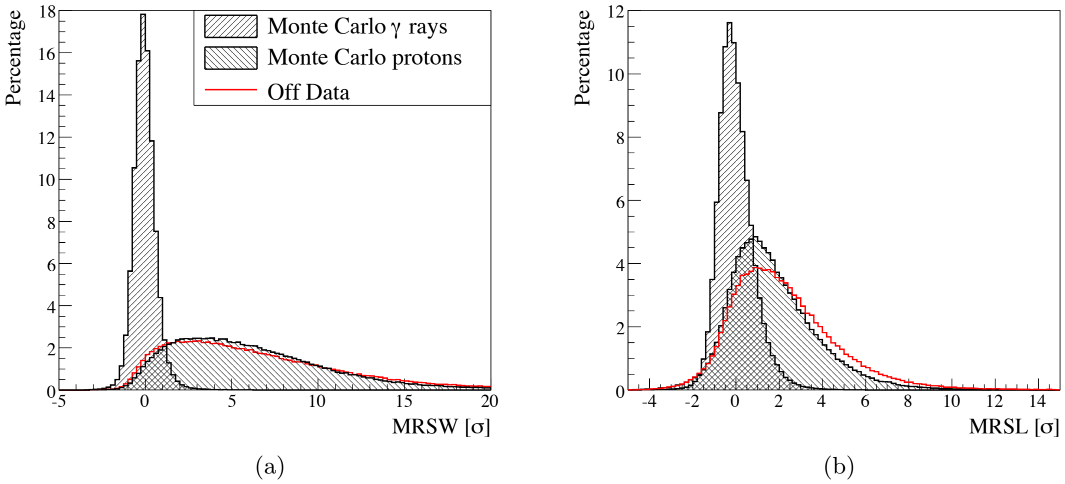

Figure 4.3: (a) MRSW and (b) MRSL distribution of Monte Carlo γ-rays and Monte Carlo protons simulated at a zenith angle of 20° compared to OFF data at zenith angles of $15^\circ - 25^\circ$. Shown are all events that pass the size cut and the distance cut of the *standard* configuration in the H.E.S.S. Standard Analysis. The image has been taken from Ohm (2010).

and similarly for the MRSL. Figure 4.3 shows the MRSW and MRSL parameter distributions for Monte Carlo γ-rays, Monte Carlo protons and data obtained from observations of sky regions without any γ-ray sources. This *Off data* consists of mainly hadronic cosmic rays, thus background events. The different selection cuts have to be optimised simultaneously for different types of sources with their characteristic fluxes and energy spectra in order to account for specific source properties and to maximise the detection significance. The optimisation of the selection cuts is done with respect to the Crab nebula, which is the strongest known VHE γ-ray source and serves as a standard candle in VHE γ-ray astronomy (Weekes et al. 1989; Aharonian et al. 2006a; Meyer et al. 2010). For example, *standard cuts* have been optimised for sources with a flux of 10% of the Crab flux and a similar spectral index of ~2.6, whereas *hard cuts* are optimised for point sources with 1% flux of the Crab above 200 GeV and a spectral index of ~2.0. A more detailed description of the optimisation process can be found in Aharonian et al. (2006a).

Configuration	*MRSW* Max σ	*MRSL* Max σ	θ^2_{cut} Max (deg^2)	Size Min (p.e.)
standard	0.9	2.0	0.0125	80
hard	0.7	2.0	0.01	200

Table 4.1: Selection cuts optimised for the *standard* (strong, steep spectrum sources) and *hard* (weak, hard spectrum sources) configuration. Minimum cuts for *MRSW* and *MRSL* of -2.0 are applied to both configurations (Aharonian et al. 2006a).

4.3 Background estimation

After stereoscopic reconstruction, image cleaning, and cuts on image parameters the hadron-induced air showers are reduced by a factor of ∼100. Still, the remaining background is of mainly hadronic origin. To eliminate these hadron-induced events and also air showers generated by electrons or positrons, which cannot be distinguished from γ-ray-induced events using the shower shape, an analysis-based background estimation has to be applied.

All background methods mentioned here have in common that the showers detected from a signal region (ON) in the field of view are compared to showers detected from another region defined as background region (OFF). The difference between the background methods lies in the construction of the OFF regions. It is crucial that the OFF regions are not contaminated with any γ-ray signal connected to a source. Therefore *exclusion regions* are defined around all known γ-ray sources and cut out from the OFF regions. It is necessary to ensure a comparable *system acceptance* for γ-ray-like events. The acceptance is energy dependent and drops radially with increasing distance to the camera centre. Two background rejecting methods, which have been used for this thesis are sketched in Figure 4.4 and are presented in the following.

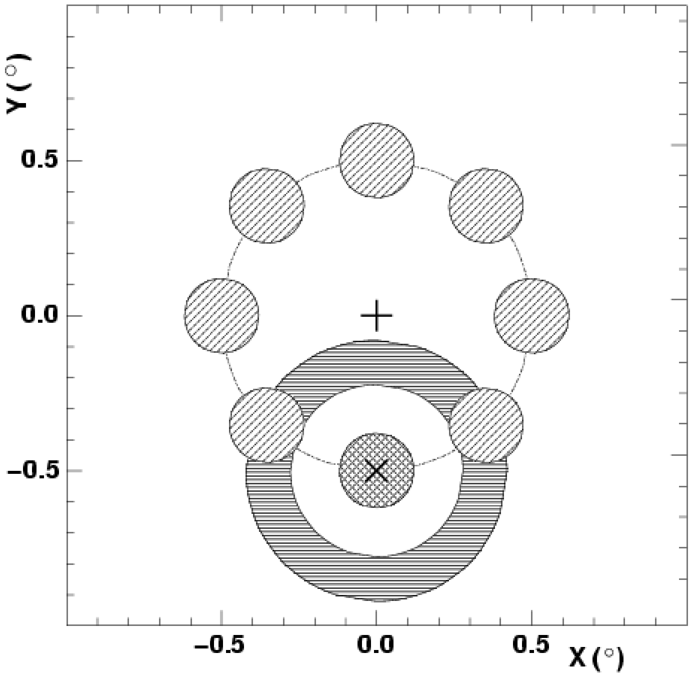

Figure 4.4: The image illustrates the ring background method with the ON region with the surrounding ring (horizontally hatched) and the reflected background method with the circularly distributed ON and OFF regions (diagonally hatched). A cross and a plus sign mark the centre of the ON region and the pointing position of the telescopes, respectively, and indicate the *wobble offset* between the target and the observation position. The image has been taken from Aharonian et al. (2006a).

4.3.1 Ring background method

The horizontally hatched parts in Figure 4.4 illustrate the ring background method. The ON region is defined around the source position. The radius is chosen such that practically the entire signal from the γ-ray source is enclosed in the ON-region. The OFF region is then defined by a ring around the observation position such that the *inner ring radius* is clearly remote from the ON region. To improve the background statistics the area of the OFF region is chosen larger (usually seven times) than the ON region. The number of OFF events is later scaled to the difference in area between the ON and OFF regions and to the different radial acceptance curve to estimate the γ-ray-like cosmic ray background. Using the ring background method one can calculate the number of γ-ray events exceeding the background level for each position in the FOV. The method is therefore suitable for creating sky maps. However, the ring background method cannot be applied for spectral reconstruction since the acceptance is energy dependent.

4.3.2 Reflected background method

The diagonally hatched parts in Figure 4.4 illustrate the reflected background method. This method can only be applied in the so-called *wobble mode* where the pointing position of the detector is offset from the target position (from where the γ-ray signal is expected). The ON region is defined around the target position such that it includes the complete emission region but is distant enough from the observation position, which is at the camera centre. OFF regions are mirrored around the observation position in a way that the total OFF area is several times the size of the ON area. Since the ON and OFF regions all have the same radial distance to the camera centre, no acceptance correction has to be considered. Therefore the reflected background method is suitable for the spectral reconstruction of the observed γ-ray source.

4.3.3 Significance determination

The number of *excess* events $\mathrm{N_{excess}}$ determines the number of γ-ray-like events from an observed target above the γ-ray-like background. It is calculated using the number of γ-ray-like events counted in the ON and OFF region ($\mathrm{N_{ON}}$ and $\mathrm{N_{OFF}}$, respectively) and the scaling factor α, which accounts for the differences in solid angle, exposure time and acceptance between ON and OFF regions.

$$\mathrm{N_{excess}} = \mathrm{N_{ON}} - \alpha \cdot \mathrm{N_{OFF}} \tag{4.2}$$

The scaling factor α takes into account the differences in size of the ON and OFF areas, as well as the different radial acceptance of the ON and OFF regions.

From the number of excess events the significance S of the γ-ray signal above the background is calculated following the approach suggested by Li & Ma (1983).

$$\mathrm{S} = \sqrt{2}\left(\mathrm{N_{ON}}\ \ln\left(\frac{(1+\alpha)\mathrm{N_{ON}}}{\alpha(\mathrm{N_{ON}}+\mathrm{N_{OFF}})}\right) + \mathrm{N_{OFF}}\ \ln\left(\frac{(1+\alpha)\mathrm{N_{OFF}}}{\mathrm{N_{ON}}+\mathrm{N_{OFF}}}\right)\right)^{1/2} \tag{4.3}$$

Throughout this work a significance of 5 standard deviations is required for the reliable detection of a source.

4.4 Energy reconstruction

The energy reconstruction is based on the fact that for a given zenith and offset angle and impact parameter the image amplitude measured in the camera is proportional to the energy $\mathrm{E_0}$ of the primary particle. Using Monte-Carlo simulations of γ-rays with certain energies and different sets of zenith and offset angles, ϕ_z and ψ_offset, two-dimensional lookup-tables containing reconstructed image amplitudes and simulated impact parameters are filled. From these lookup tables the reconstructed energy can be extracted. For an individual event, the energy estimate is done for each participating telescope separately. The reconstructed energy is averaged over all participating telescopes and the individual energies are weighted with their deviation from the average value.

The energy resolution is defined as the difference between the simulated and the reconstructed energy $(\mathrm{E_{sim}} - \mathrm{E_{reco}})/\mathrm{E_{sim}}$ and is ~15 % for zenith angles up to 55 °. A *safe energy threshold* $\mathrm{E_{safe}}$ is defined as the energy above which the bias in the reconstructed energy is less than 10%. A detailed description of the energy reconstruction and the error estimation is given in Berge (2006).

4.5 Spectrum determination

The determination of source spectra is of particular importance for the study presented here as SNRs are widely believed to be able to accelerate particles up to TeV energies. The systematic study of the γ-ray fluxes provides valuable information about the acceleration processes taking place in the observed SNRs. The source spectrum, which is derived from the differential γ-ray flux, is commonly defined by the number of excess γ-rays N_γ per energy E, observation time T and effective area A_{eff}. The effective area A_{eff} allows to calculate the γ-ray flux during the observation time given the count rate of γ-ray events. In the following the basic procedure for the spectrum determination is described.

4.5.1 Effective detection area

The differential flux of a γ-ray source is estimated using the number of collected γ-rays which pass the applied selection cuts N_γ, the corresponding effective γ-ray collection area A_{eff} for the given data set and the live time of the observation t. The differential flux is calculated from the number of γ-ray excess events according to equation (4.2), per reconstructed energy E and time t, weighted by A_{eff}:

$$F(E) = \frac{1}{A_{eff}(E, \phi_z, \theta_{az}, \psi_{offset}, \epsilon, \varepsilon_{opt})} \frac{d^2 N_\gamma(E)}{dEdt} \; . \tag{4.4}$$

A_{eff}, the area to which the instrument is sensitive for the detection of incoming particles, is a function of the event energy E and furthermore depends on the zenith and azimuth angles ϕ_z and θ_{az}, the offset between the pointing and the source ψ_{offset}, on the cut efficiency ϵ (determined by cuts on image parameters), as well as on the optical efficiency ε_{opt} varying with time. The dependency of the effective area on each of the parameters has been studied in detail by Hoppe (2008). The size cuts on the images result in few events with low energies, which sets a lower energy threshold, for which the energy of the incoming VHE γ-ray can be reconstructed. For each run only those events are considered which have an energy above the safe energy threshold.

4.5.2 Flux calculation

The number of γ-rays per energy bin E_i is given by the number of ON and OFF counts in this energy bin, scaled by the factor α and weighted with the inverse of the bin width $\triangle_i$, the observation time T, and the effective area A^i_{eff} summed over the number of runs.

$$\left(\frac{dN}{dE}\right)_i = \frac{N^i_{on} - \alpha_i N^i_{off}}{\triangle_i \sum\limits_{runs} T A^i_{eff}} \tag{4.5}$$

Throughout this work a power-law is assumed for all observed targets and fitted to the differential energy spectrum: $F(E) = F_0 \; E^{-\Gamma}$ with the normalization F_0 and the spectral index Γ. More details on different approaches to the generation of spectra can be found in Berge (2006).

Knowing the source spectrum, the integral flux can be calculated within the chosen energy limits. Throughout this work, the integral is calculated above the energy threshold $E = 1\,\mathrm{TeV}$.

5 Supernovae and their remnants

This chapter gives a brief introduction into supernova explosions, their progenitors, and their remainders. A detailed study of the latter, supernova remnants (SNRs), has been conducted using very-high-energy (VHE) γ-ray data and is presented in the next chapter. A supernova (SN), which is among the most energetic phenomena in the universe, represents the death of a star. For several weeks after the explosion the light of a SN can even outshine its entire galaxy. During the explosion, huge amounts of matter are ejected into the surroundings of the star. The ejecta contains many heavy elements, generated through nucleosynthesis during the life of the star as well as during the explosion. This makes SNe the main source of heavy elements in the universe. The explosion energy of a SN is partly released in the kinetic energy of the progenitor star's ejecta. The expanding material moves with supersonic speed and drives a shock front into the interstellar medium (ISM). In these shock fronts the acceleration of cosmic particles is possible up to energies of 10^{14} TeV and above. Assuming one SN every $\sim$30 years, an acceleration efficiency of 10-30 % is necessary to explain the flux of cosmic rays measured on Earth, as discussed by Drury et al. (1994). Many different classes of SNe can be distinguished, historically defined by the emission of characteristic spectral lines. SNe exhibiting hydrogen lines in their spectra are called type II, those without hydrogen lines are of type I. However, based on the initial mass of the progenitor star, two fundamental types of SNe occur, which follow different physical processes. One is characterized by the thermonuclear disruption of a white dwarf in a binary system (type Ia) and the other is the result of the core collapse of a massive star (type II). In the following, based on textbook descriptions (Longair 1994; Carroll & Ostlie 1996; Unsöld & Baschek 1999), these two SN scenarios are presented.

5.1 Thermonuclear supernovae

A star with an initial mass $M_{init} < 8\,M_{\odot}$ can develop into a white dwarf with a mass of $M_{WD} < 1.4 M_{\odot}$ at the end of its lifespan after having suffered from high mass losses during earlier stages. The energy released during nuclear reactions prevents the star from gravitational collapse. After the fusion of light elements like hydrogen and helium the core contracts more and more under the gravitational pressure of the outer layers of the star. The increasing pressure on the core ignites the fusion of light elements in the layers next to the core as well. The low initial mass of the star is not sufficient to generate a pressure large enough to go beyond the production of oxygen. The star therefore cools down without any perturbations in the core. However, a white dwarf in a binary system can accrete mass from a companion star, increasing its own mass and eventually exceeding the Chandrasekhar limit of $M_{chand.} \approx 1.4\,M_{\odot}$. Due to the Fermi pressure from the completely degenerate electron gas the core cannot contract any further. However, beyond the Chandrasekhar mass limit the core cannot withstand the gravitational pressure of the accumulated mass. The high pressure regime ignites further fusion stages and results in the total disruption of the white dwarf as a type Ia SN. The amount of energy released is of $\mathcal{O}(10^{51}\,\text{erg})$.

5.2 Core-collapse supernovae

Stars with an initial mass of $M_{\text{init}} > 8M_{\odot}$ undergo the same initial stages as a white dwarf. The higher mass, however, allows for nuclear fusion beyond oxygen, always starting the next fusion stage with increasing pressure onto the core exerted by the outer layers. The fusion chain continues until reaching iron, where fusion to still heavier nuclei becomes endothermic. The missing radiative pressure from the fusion together with the extremely high gravitational pressure from outer layers make the core unstable. Photodisintegration of heavy nuclei removes thermal energy from the gas, that would otherwise have provided the necessary pressure to support the core. The electron capture by heavy nuclei and protons further results in the loss of the electron degeneracy pressure (Carroll & Ostlie 1996). If the mass of the iron core is $M_{\text{core}} > 1.4M_{\odot}$, the core collapses and core densities of up to $3 \cdot 10^{17}\,\text{kg m}^{-3}$ at temperatures of $\sim 10^{12}\,\text{K}$ develop. The neutron degeneracy pressure finally halts the collapse, but infalling outer layers are suddenly stopped, which creates a shock front moving radially away from the core and blowing apart outer layers. The amount of energy released during this type II SN explosion is of $\mathcal{O}(10^{51} - 10^{52}\,\text{erg})$.

5.3 Stages of a supernova

During a SN explosion, the progenitor star emits huge amounts of masses on the order of several solar masses into the interstellar medium (ISM). Driven by high pressure force, the ejecta expands into the ISM at supersonic speed and therefore forms a shock front in the interstellar gas. With time this shock wave slows down by the increasing amount of swept up ISM. With decreasing temperatures also radiative cooling of the shock becomes effective. Finally, having swept-up large amounts of matter, the velocity of the shell approaches the random motion of interstellar clouds and the shell dissipates into the ISM (Woltjer 1972). The evolution of SNe can be described by four phases, assuming the ambient medium to be uniform with low pressure and density.

Free expansion

The beginning of the SN explosion is characterized by free expansion of the ejecta. The progenitor star's material moves away from the star into the ISM, resulting in a supersonic blast wave with speeds of $\mathcal{O}(10^4\,\text{km s}^{-1})$. For several hundred years, the temperature and the expansion speed of the shock wave remain nearly constant. The interaction of the shock front with the ISM generates an inward-facing reverse shock moving through the already shocked material.

Adiabatic phase (Sedov phase)

With the swept-up mass approaching the mass of the ejected material, the shock wave begins to slow down. The internal energy of the shock is still very large compared to radiative energy losses, resulting in a nearly adiabatic expansion. This phase lasts about 10^4 years and the evolution of the shock front depends entirely on the initial explosion energy and the surrounding ISM. The self-similar solution proposed by Sedov (1946) and Taylor (1950) describes the evolution of the density, the pressure, the temperature and the expansion velocity within the shock. Rayleigh-Taylor instabilities mix shocked material inside the main shell with SN ejecta, leading to an enhanced magnetic field and strong X-radiation.

Radiative phase (snowplow phase)

As the temperature behind the shock wave cools down below $10^6\,\mathrm{K}$, radiative cooling becomes more efficient than further expansion. The cooling leads to an additional pressure loss and thus the shock front slows down more rapidly. The energy is mainly radiated through optical line emission after recombination of electrons forming heavier elements, which is more efficient than thermal X-ray and synchrotron emission. The cooling of the shock leads to a dense cool shell, which keeps expanding with constant momentum and sweeping up the ISM, giving this stage of SN evolution the name ”snowplow phase”.

Dispersion phase

When the expansion velocity of the shell becomes comparable to the random motion of the ISM of $\mathcal{O}(10\,\mathrm{km\,s^{-1}})$, the shell loses its identity and after millions of years the remnant is absorbed into the ISM (Woltjer 1972).

5.4 Supernova remnants

Whatever remains from the SN explosion is called the SNR. If the entire explosion energy was deposited equally in all directions, SNRs would all have the same appearance. Due to differences in the progenitor star and the explosion conditions, density variations in the ISM and Rayleigh-Taylor instabilities, SNRs can be categorized into three different types based on their appearance.

- **Shell-type SNRs** emit most of their radiation from a thin shell. When looking at the edges of the three dimensional shell limb brightening makes this appear like a bright ring for the observer.
- **Filled-center SNRs** are also called plerions or Crab-like SNRs, as the Crab nebula is the most famous example. They are powered by a central pulsar and emit most of their radiation from within the expanding shell. The radiation is generated from high-energy electrons, which emit synchrotron radiation from the radio to the X-ray waveband.
- **Composite SNRs** appear as shell-type or Crab-like depending on the observation wavelength. *Thermal* composite SNRs exhibit a shell in radio and appear Crab-like in the X-ray waveband, whereas *plerionic* composite SNRs appear Crab-like at both radio and X-ray wavelengths but still have a shell.

5.5 Particle acceleration in shock fronts

To explain the measurable cosmic ray flux, energies of about 10^{50} erg have to be spent on particle acceleration. This energy can be provided during a SN explosion. Therefore SNRs are widely believed to accelerate particles up to energies of 10^{14} eV, if 10-30 % of the released explosion energy go into the acceleration process. The presentation of mechanisms possibly leading to efficient particle acceleration follows the discussion presented by Longair (1994).

Second order Fermi acceleration

An explanation of cosmic ray (CR) production has been proposed by Fermi (1949). He suggested the acceleration of charged particles by randomly moving molecular clouds, which act as 'magnetic mirrors' due to their individual magnetic field. The particles undergo multiple head-on and following collisions with the magnetic mirrors, where they gain and lose energy, respectively. With head-on collisions being more frequent and assuming the particles remains within the acceleration region for some time, they can reach energies in the TeV range following a power-law distribution. The average energy gain for a relativistic particle with an initial velocity v close to the speed of light is

$$\left\langle \frac{\Delta E}{E} \right\rangle = \frac{8}{3} \left(\frac{V_{mirror}}{c} \right)^2 . \tag{5.1}$$

The energy gain during this acceleration process, however, is only of second order, from where the name *second order Fermi acceleration*. Objections against this acceleration scenario are the low velocities of the molecular clouds (of about 10^{-4} of the speed of light c), the long mean free path length of the cosmic rays in the ISM of ~1 pc resulting in about one collision per year and the neglect of energy losses, which influence the acceleration process. Therefore it is unlikely that significant particle acceleration results from this initial Fermi acceleration process.

First order Fermi acceleration

Based on the second order Fermi acceleration another acceleration mechanism has been discovered independently by Krymskii (1977), Axford et al. (1977), Blandford & Ostriker (1978), and Bell (1978), which allows in the presence of strong shocks to consider head-on collisions only. High-energy particles ahead of and behind the shock are assumed to be isotropically distributed. Instead of considering a shock wave moving with velocity U through the gas at rest with density ρ_1, temperature T_1 and pressure p_1 and leaving it behind at ρ_2, T_2 and p_2, calculations are done within the rest frame of the shock front. From mass conservation follows

$$\rho_1 v_1 = \rho_2 v_2, \tag{5.2}$$

where 1 and 2 denote the upstream and downstream regions, respectively. In case of a strong shock, the difference in density depends on the ratio γ of specific heats of the gas with

$$\frac{\rho_2}{\rho_1} = \frac{(\gamma + 1)}{(\gamma - 1)}. \tag{5.3}$$

For a monoatomic or fully ionized case as considered here, $\gamma = 5/3$ and therefore $\rho_2/\rho_1 = 4$, which leads to

$$v_2 = \frac{1}{4}v_1. \tag{5.4}$$

A particle moving from the upstream region through the shock receives a small increase in energy from the head-on collision with the downstream gas, which moves at a velocity $3/4U$ relative to the upstream gas. However, when considering a particle diffusing from the isotropic gas behind the shock to the upstream region, it encounters gas moving towards the shock front also at a speed of $3/4U$. This again represents a head-on collision, resulting in an increase of energy. The energy gain per collision is calculated from a Lorentz transformation of the particles energy into the rest frame of the shock and by averaging over all arrival angles of the particle with respect to the shock front (Bell 1978) and yields $\left\langle \frac{\Delta E}{E} \right\rangle = \frac{2}{3}\frac{V}{c}$. The fractional energy increase for a round trip across the shock and back again is therefore given by

$$\left\langle \frac{\Delta E}{E} \right\rangle = \frac{4}{3}\frac{V}{c}. \tag{5.5}$$

The energy increase being of first order in terms of shock velocity gives the mechanism its name *first order Fermi acceleration*. The resulting spectrum of accelerated particles is derived from the energy after one shock crossing cycle $E = E_0\beta$ with β being the mean energy gain per cycle and the probability P of a particle to stay within the acceleration region. The escape probability η given by Bell (1978) is $\eta = 4v_2/v_{particle}$, which results in $P = 1 - 4v_2/v_{particle}$. The number of particles after k collision cycles is then given by $N = N_0P^k$ with an energy of $E = E_0\beta^k$. From equation (5.5) results the energy gain factor $\beta = 1 + \frac{4}{3}\frac{V}{c}$. Eliminating k yields

$$\frac{\ln(N/N_0)}{\ln(E/E_0)} = \frac{\ln P}{\ln \beta} \tag{5.6}$$

and

$$\frac{N}{N_0} = \left(\frac{E}{E_0}\right)^{\ln P/\ln \beta}. \tag{5.7}$$

The total differential of N is given by a power-law

$$N(E)dE = \text{const} \cdot E^{-1+(\ln P/\ln \beta)}dE. \tag{5.8}$$

In case of a strong shock $\ln P/\ln \beta = -1$, which results in the differential energy spectrum of the accelerated particles

$$N(E)dE \propto E^{-2}dE. \tag{5.9}$$

This simple model of the acceleration mechanism allows to explain the general particle acceleration in strong shocks as occurring in SNRs. However, the acceleration mechanism still describes a slow process which requires the particles to diffuse through the shock multiple times. As Bell (1978) pointed out, particles penetrating the shock into the upstream region return across the shock, whereas particles travelling downstream tend to convect away from the accelerating region. Due to the finite time of the acceleration phase in a SN shock, Lagage & Cesarsky (1983) derive an upper limit to the energy of the accelerated particles in a typical SN of $\sim 10^{14}$ eV. Since the spectrum of cosmic rays extends far beyond this limit, the time-scale of acceleration has to be increased or other acceleration mechanisms than shock acceleration in SNe must exist (K. Gaisser 1990). Including effects of diffusion of the CR particles while travelling trough the ISM, the theoretically derived spectral index meets the measured index of CRs of $2.5 - 2.7$ at $1 - 10^3\,\mathrm{GeV}$.

Within this thesis particle acceleration in SNRs only is investigated via the observation of VHE γ-rays in the energy range between 100 GeV and 100 TeV, whose generation requires cosmic rays of at least the same energy. They allow to map the origin of particle acceleration since γ-rays are not deflected in galactic magnetic fields. Several processes generating γ-radiation are presented in the following section.

5.6 Production of γ-rays

The CR spectrum extends to extremely high energies. This suggests that the radiation mechanisms in the VHE range cannot be of purely thermal nature. Radiative processes for the entire γ-ray spectrum are described in detail by Aharonian (2004). Here only a short summary of the essential γ-ray production mechanisms is given. For the emission of radiation of VHE photon energies ($10^{11} - 10^{14}\,\mathrm{eV}$), two main production mechanisms are known. They are based on leptonic interactions, described by the interaction of high-energy electrons with low energy photon fields and the Galactic magnetic field and and on hadronic interactions, resulting from the decay of neutral pions generated in proton–proton interactions.

5.6.1 Hadronic interaction

Through the inelastic interaction between relativistic protons and nuclei, mesons are generated. For kinetic proton energies above $\sim 0.3\,\mathrm{GeV}$ the production of π^0 mesons is possible, which decay immediately into two γ-rays and represent the dominant channel for hadronic γ-ray production. The γ-ray emissivity through the π^0 channel can be estimated by

$$q_\gamma(E_\gamma) = 2 \int_{E_{min}}^{\infty} \frac{q_\pi(E_\pi)}{\sqrt{E_\pi^2 - m_\pi^2 c^4}}\, dE_\pi \ , \tag{5.10}$$

where $E_{min} = E_\gamma + m_\pi^2 c^4 / 4E_\gamma$, m_π is the π^0-meson restmass and q_π represents the emissivity of secondary particles created during from proton-proton interactions (Aharonian et al. 1997). The maximum of the π^0-induced γ-ray spectrum is at $E_\gamma \sim 70\,\mathrm{MeV}$, independent of the parent π_0 and proton population. The total cross section of proton-proton collisions σ_{pp} in the GeV to TeV energy region is given by

$$\sigma_{pp}(E_p) \approx 30 \left[0.95 + 0.06 \cdot \ln\left(\frac{E_{kin}}{1\mathrm{GeV}}\right)\right] \mathrm{mb} \ , \tag{5.11}$$

showing that above $E_{kin} \sim 2\,\mathrm{GeV}$ the cross section increases only weakly logarithmically with the energy. Therefore the characteristic cooling time due to inelastic proton-proton interactions for initial protons with energies of $E > 1\mathrm{GeV}$ is almost independent of the energy, given by

$$t_{pp} \simeq 5.3 \cdot 10^7 \left(\frac{n}{\mathrm{cm}^{-3}}\right)^{-1} \ , \tag{5.12}$$

with the density of the ambient medium n. With energy losses from nuclear interactions dominating over ionization processes, the initial proton spectrum remains unchanged. Furthermore the γ-ray spectrum repeats the parent proton spectrum. Therefore, the observation of VHE γ-rays yields direct information on the parent proton population.

5.6.2 Leptonic interaction

Inverse Compton scattering

Via inverse Compton (IC) scattering low-energy photons can be up-scattered by high-energy electrons reaching energies in the entire γ-ray range. The most abundant seed particle of low-energy photons is the cosmic microwave background (CMB) 2.7 K radiation. The process is governed by the Klein-Nishina cross section

$$\sigma_{\mathrm{K-N}} = \pi r_e^2 \frac{1}{\xi} \left\{ \left(1 - \frac{2(\xi+1)}{\xi^2}\right) \ln(2\xi+1) + \frac{1}{2} + \frac{4}{\xi} - \frac{1}{2(2\xi+1)^2} \right\} \tag{5.13}$$

with the classical electron radius r_e and the product of the energies of the electron and the up-scattered photon $\xi = \frac{E_e E_{ph}}{m_e^2 c^4}$. In the Thomson regime ($\xi \ll 1$) the cross section can be approximated by

$$\sigma_{IC} \simeq \sigma_T = \frac{8\pi}{3} r_e^2 \simeq 665\,\mathrm{mb}\ . \tag{5.14}$$

In the case of ultra-relativistic electrons ($\xi \gg 1$), the inverse Compton cross section is described by

$$\sigma_{IC} = \pi r_e^2 \frac{mc^2}{\hbar\omega} \left(\ln\left(\frac{2\hbar\omega}{mc^2}\right) + \frac{1}{2} \right)\ , \tag{5.15}$$

In the Thomson limit, the relation between the initial electron and photon energy, E_e and E_{ph}, and the energy of the resulting γ-ray is given by

$$E_{IC} \simeq \frac{4}{3} E_{ph} \left(\frac{E_e}{m_e c^2}\right)^2 \simeq 5 \cdot 10^{-3} \left(\frac{E_{ph}}{10^{-3}\,\mathrm{eV}}\right) \left(\frac{E_e}{1\,\mathrm{TeV}}\right)^2 \mathrm{TeV}\ . \tag{5.16}$$

Synchrotron radiation

Electrons traversing a magnetic field of strength B spiral around the magnetic field lines and emit electromagnetic radiation, which can be in the radio, optical or X-ray wavebands. Assuming an isotropic distribution of pitch angles and a mono-energetic population of electrons with energy E_e, the energy of the emitted synchrotron photons E_{sy} after Aharonian et al. (1997) is given by

$$E_{sy} \simeq 0.2 \left(\frac{B}{10\,\mu\mathrm{G}}\right) \left(\frac{E_e}{1\,\mathrm{TeV}}\right)^2 \mathrm{TeV}\ . \tag{5.17}$$

In the more realistic case of a power-law shaped electron distribution, the synchrotron radiation follows a power law as well, which allows to derive the underlying electron energy spectrum from the observed synchrotron spectrum (Blumenthal & Gould 1970). The synchrotron spectrum reaches its maximum at keV energies.

If both synchrotron and IC photons are emitted by the same electron population, their spectra are strongly correlated. Combining the expressions for the photon energy in equations 5.16 and 5.17 yields an expression for the relation between photon energies from synchrotron E_{sy} and IC E_{IC} processes

$$\frac{E_{sy}}{1\,\mathrm{keV}} \simeq 0.07 \frac{E_{IC}}{1\,\mathrm{TeV}} \frac{B}{10\,\mu\mathrm{G}} \ , \tag{5.18}$$

where B is the strength of the magnetic field. The ratio of synchrotron and IC photon fluxes, f_{sy} and f_{IC}, is then given by Aharonian et al. (1997)

$$\frac{f_{IC}(E_{IC})}{f_{sy}(E_{sy})} \simeq 0.1 \left(\frac{B}{10\,\mu\mathrm{G}} \right)^{-2} \ . \tag{5.19}$$

From equation (5.19) follows that for magnetic field strengths of $B > 10\mu$G the synchrotron component dominates over the IC component.

5.7 Theoretical γ-ray flux prediction

Assuming that CRs are accelerated and VHE γ-rays produced in SNRs, the flux of VHE γ-rays depends on explosion and acceleration parameters, the properties of the ambient medium, and the distance of the SNR. Drury et al. (1994) propose a theoretical model to predict the flux of VHE γ-rays from SNRs generated from hadronic CR interactions above a given energy threshold:

$$F_\gamma(> E) \approx 9 \cdot 10^{-11} \theta \left(\frac{E}{1\,\mathrm{TeV}} \right)^{-1.1} \left(\frac{E_{SN}}{10^{51}\mathrm{erg}} \right) \left(\frac{d}{1\,\mathrm{kpc}} \right)^{-2} \left(\frac{n}{1\,\mathrm{cm}^{-3}} \right) \mathrm{cm}^{-2}\mathrm{s}^{-1}, \tag{5.20}$$

where E is the energy threshold, θ the efficiency of the particle acceleration, E_{SN} the total energy released during the supernova explosion, d the distance from Earth to the SNR and n the density of the interstellar medium surrounding the SNR. Drury et al. (1994) also discuss possible values of the different parameters. For the present work, the γ-ray flux of the individual SNRs is calculated using the following values:

$$\begin{aligned} E &= 1\,\mathrm{TeV} \\ \theta &= 0.1 \\ E_{SN} &= 10^{51}\,\mathrm{erg} \\ n &= 1\,\mathrm{cm}^{-3} \end{aligned}$$

The distance of the SNRs is either known from observations in other wavebands or derived using the $\Sigma - D$ relation proposed by Case & Bhattacharya (1998). Thereby the distance of a SNR is estimated from its surface brightness and apparent size in the radio waveband.

6 Supernova remnants in γ-rays

As described earlier, supernova remnants (SNRs) are widely believed to be VHE γ-ray emitters due to the large amount of energy released during a supernova explosion. This hypothesis is supported by the results of detailed studies of individual objects such as *RX J1713.7-3946* (Aharonian et al. 2004, 2006b, 2007b), *RCW 86* (Aharonian et al. 2009b) and *SN 1006* (Naumann-Godó et al. 2008).

In the present work a systematic approach to test this hypothesis is presented using Green's catalog of SNRs detected by radio telescopes (Green 2009). The advantage of using Green's catalog is the large number of 274 SNRs with their exact positions compared to the few SNRs detected in VHE γ-rays. The catalog also provides a collection of results from other wavelengths, which is useful for further studies on individual objects. Using a large sample of SNRs allows not only to investigate many individual objects but to find general laws for the SNR population and to deduce implications for further observations of SNRs in VHE γ-rays. The results of this systematic study of radio SNRs are presented in this chapter. Details on Green's catalog are given in section 6.1. For all SNRs in the field of view of H.E.S.S. the VHE γ-ray signal is investigated and presented in section 6.2. For the first time, upper limits on the flux of VHE γ-rays are derived for 137 SNRs known in radio. The theoretical model proposed by Drury et al. (1994) predicting the VHE γ-ray flux is investigated. Using measured flux values described in section 6.3, constraints on model parameters are given for 55 SNRs. The hypothesis of spatial correlations between known VHE γ-ray emission regions and radio SNRs is tested in section 6.4 by comparing the positions of Green's radio SNRs as well as positions of a simulated sample of SNRs to known H.E.S.S. sources.

6.1 Green's Catalog of Radio SNRs

This supernova remnant study is based on the catalog assembled by Dave Green containing 274 galactic radio SNRs (Green 2009). The main information given in the catalog that is used for the presented study are the SNRs' positions in the sky, their angular size and their flux density in radio. Furthermore the type of remnant is known for most SNRs, being either *filled-center*, *composite* or *shell-type*. The distribution of SNRs in the sky is shown in Fig. 6.1.

The SNRs are distributed over the entire Galaxy in galactic longitude and latitude. However, most SNRs are located close to galactic plane. Furthermore the concentration of SNRs within 100 ° in galactic longitude around the galactic center is much larger than at higher galactic longitudes. The SNR distribution follows the distribution of regions with higher density within the Galaxy, as SNRs are the remainders of stars, which are found at a higher concentration in regions with high densities. On the other hand, observations of many instruments focus on the galactic plane, which introduces a selection effect. Small, faint, and distant SNRs have a lower detection probability due to the limited sensitivity

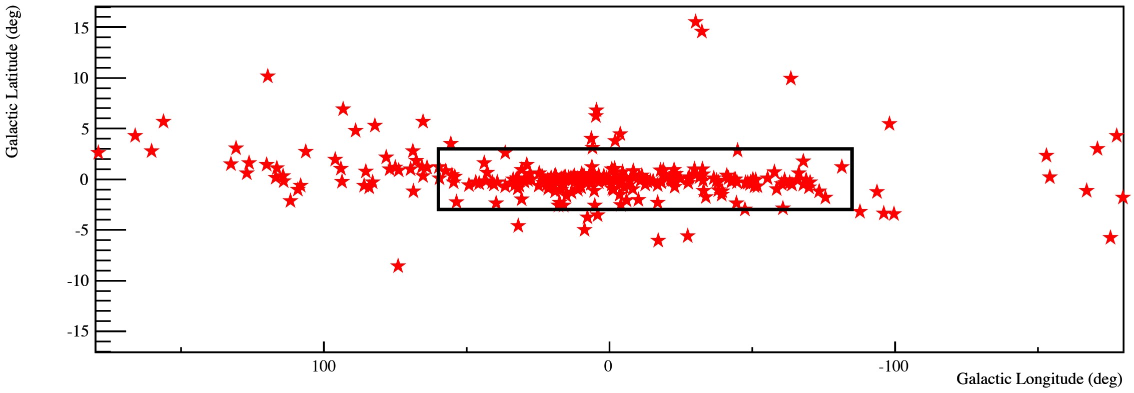

Figure 6.1: Distribution of 274 radio SNRs from Green's catalog in the sky. The black box indicates the region of the H.E.S.S. Galactic Plane Survey. During the study only those 203 SNRs within this box will be considered.

of all instruments. Other SNRs cannot be observed due to the restricted accessible field of view in our Galaxy. These selection effects can also influence the search for correlations between radio and VHE γ-ray emission from SNRs since the search for γ-radiation uses only positions with known radio SNRs. SNRs which have not been detected in the radio waveband are ignored during this study. Further details on the selection effects are given in Green (2009).

The black box in Fig. 6.1 indicates the region of the H.E.S.S. Galactic Plane Survey (GPS). Within this region, ranging from -85 to 60 degrees in galactic longitude and from -3 to 3 degrees in galactic latitude, the coverage of both radio and γ-ray observations is quite balanced. Inside this region a systematic search for VHE γ-ray emitters has been performed (Aharonian et al. 2006d). Outside this region the H.E.S.S. observation time varies too strongly, which results in a coordinate-dependent sensitivity of the detector and does not allow a systematic search. Therefore the sample of radio SNRs is reduced to those 203 SNRs being located within the H.E.S.S. Survey region. A list of these SNRs can be found in the appendix in Table A.2. From now on, all investigations refer to these 203 SNRs within the GPS region only.

Fig. 6.2 illustrates the accumulated acceptance-corrected observation time within the GPS region and shows the positions of 203 SNRs indicated by circles according to their size. The map is truncated at a maximum of 80 hrs. The difference in observation time shows where past H.E.S.S. observations have been focused on. Major goals have been the detection of TeV γ-rays originating from the Galactic Center and later of the precise determination of the position of the VHE source in the Galactic Center (van Eldik et al. 2008), excluding the SNR Sagittarius A East as the origin of the γ radiation and attributing it to Sagittarius A*. Further noticeable efforts in terms of observation time have been made for the binary pulsar PSR B1259-63 (HESS J1302-638) and the pulsar wind nebulae MSH 15-52 (HESS 1514-591) and HESS J1825-137, the latter possibly being powered by the pulsar PSR B1823-13 (Aharonian et al. 2005e,f,g). The positions of radio SNRs show that except for few SNRs detected in the past the amount of H.E.S.S. observation time does not show any correlation with the SNRs' positions. The distribution of the galactic

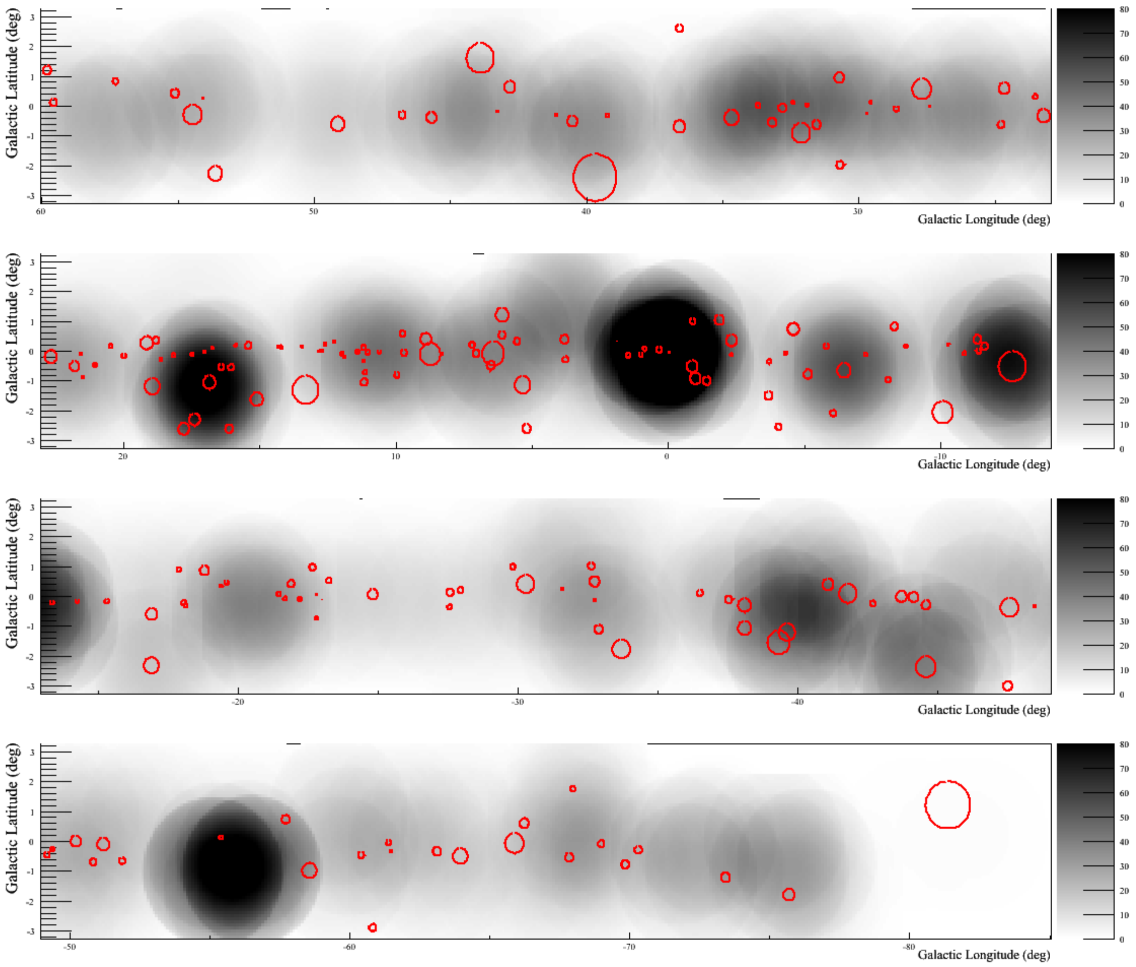

Figure 6.2: The figures show the entire region of the H.E.S.S. Galactic Plane Survey from 60 ° to -85 ° in galactic longitude and from -3 ° to 3 ° in galactic latitude. Red circles represent the positions and sizes of the SNRs from Green's catalog (Green 2009). The underlying skymap in a grey colorscale shows the acceptance-corrected livetime of all SNRs in the skymap, truncated at 80 h.

longitude and latitude of the studied SNRs is illustrated in Fig. 6.3. Green's catalog allows to directly access SNR positions and use H.E.S.S. data for a general study of γ-rays emitted by SNRs. Green's catalog lists basic parameters, which are relevant for radio observations, such as the flux density and the spectral index in radio. For the application of VHE γ-ray data it is necessary to extend the catalog by several values needed for H.E.S.S. data analysis and the population study.

6.1.1 SNR Radius

In the catalog the size of the SNRs is given as the major and minor axes of an ellipse. From these diameters a radius is calculated, approximating all SNRs with a circular shape. The mean radius R_{mean} is given by the quadratic mean of the minor and major angular

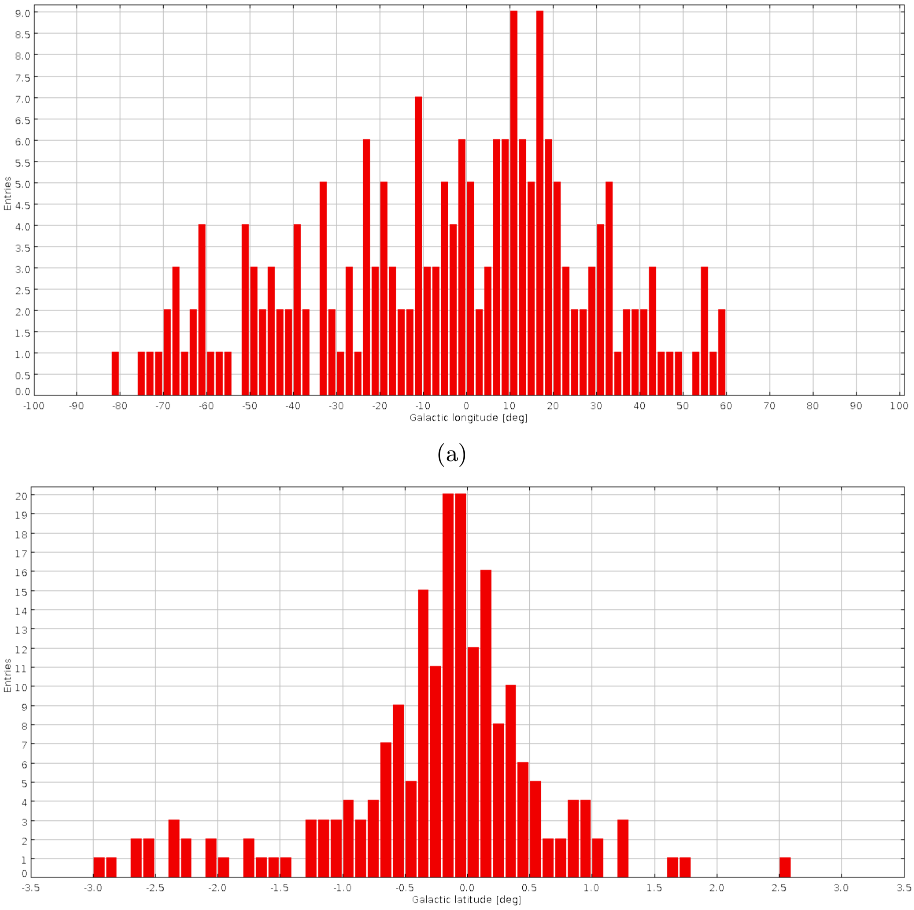

(a)

(b)

Figure 6.3: Distribution of (a) galactic longitude and (b) galactic latitude of radio SNRs listed in Green's catalog.

radius R_{min} and R_{maj}

$$R_{mean} = \sqrt{\frac{1}{2}\left(R_{min}^2 + R_{maj}^2\right)} \tag{6.1}$$

Instead of using the mean radius it is also possible to keep the area of the circularly shaped SNRs equal to the area of original elliptic shape. This would require the calculation of the radius $R = \sqrt{R_{min} \cdot R_{maj}}$. Comparisons have shown that the difference between radii obtained from the two methods is negligible. For the investigation of the SNRs the radius calculated with Equation 6.1 has been used. Fig. 6.4 illustrates the distribution of SNR radii.

6.1.2 SNR Distance

The distance of a radio SNR can only be determined under very particular conditions, for example when a nearby molecular cloud permits direct distance measurements. In this case either kinematic methods assuming a galactic rotation model are applied or the distance is estimated using the extinction of light within the line of sight or via trigonometric

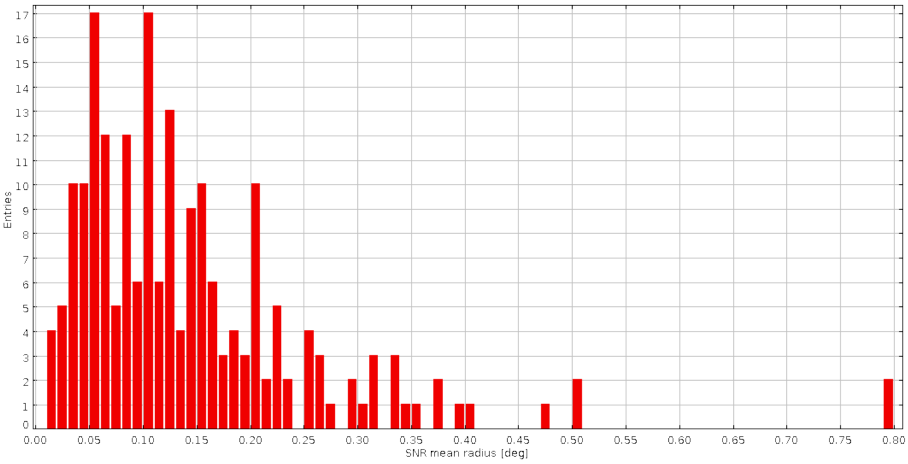

Figure 6.4: Distribution of mean SNR radii derived from Equation 6.1.

parallax measurements (Stead & Hoare 2010). Since this is possible for few SNRs only, a calculation based on accessible parameters is desirable. For shell type SNRs, Case & Bhattacharya (1998) have investigated the correlation between the surface brightness in the radio waveband Σ_{1GHz} and the surface diameter D of the SNR and have proposed the so-called $\Sigma - D$ relation.

$$\Sigma_{1GHz} = 2.07^{+3.10}_{-1.24} \cdot 10^{-17} \cdot D^{-2.38\pm0.26} \quad \mathrm{Wm^{-2}Hz^{-1}sr^{-1}}. \tag{6.2}$$

The $\Sigma - D$ relation is derived from SNRs with distances derived from radio and X-ray observation. The errors in the relation therefore take into account the typical errors occurring in the experimental distance estimation. Case & Bhattacharya (1998) state errors of up to 30 % of distances derived from kinematic methods or from modeling of X-ray emission.

The surface brightness is defined as the flux per unit area and can be calculated from the radio flux density (in units of *Jansky*) and the angular diameter θ (in units of *arcmin*) given in the catalog

$$\Sigma_{\mathrm{calculated}} = 1.505 \cdot 10^{-19} \cdot \frac{\text{flux density[Jy]}}{\theta^2[\text{arcmin}^2]} \quad \mathrm{Wm^{-2}Hz^{-1}sr^{-1}} \tag{6.3}$$

where the factor $1.505 \cdot 10^{-19}$ accounts for the conversion of the units into $\mathrm{Wm^{-2}Hz^{-1}sr^{-1}}$. Using $D \sim \theta \cdot d$ the distance d can be calculated.

The $\Sigma - D$ relation has been derived from 36 shell-type SNRs with known distances (Case & Bhattacharya 1998). Recalculating the distance for SNRs with known distance using the $\Sigma - D$ relation shows large deviations. Therefore the relation has to be used with care. Still, with current understanding, it is the only way to estimate the distance of SNRs. Fig. 6.5 shows the spread of the calculated distance for the 36 SNRs with known distance. For distances up to 5 kpc the $\Sigma - D$ relation gives a good estimate of the distance. However, for distances above 6 kpc the relation introduces a systematic bias. The easier detection of radio-bright SNRs leads to an underestimation of the distance. Interpolating the calculated distance (Fig. 6.5) results in a second-order polynomial. The corrected

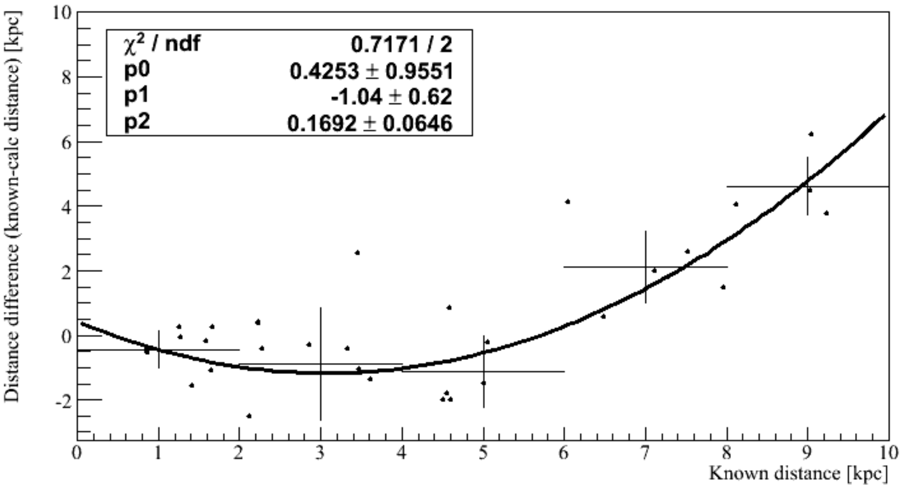

Figure 6.5: The data points indicate the differences between known and calculated distances for 36 shell type SNRs with known distance. The sample is restricted to known distances between 0 kpc and 10 kpc. The manually set 5 bins are fitted by a second-order polynomial with parameters p_0, p_1, and p_2. The interpolation is later on used to correct for the bias of the $\Sigma - D$ relation.

distance d_{corr} is given by:

$$\begin{aligned} d_{corr} &= p_0 + p_1 \cdot d_{uncorr} + p_2 \cdot d_{uncorr}^2 & (6.4) \\ &= \frac{0.4253}{(1\,\mathrm{kpc})^{-1}} - \frac{1.04}{(1\,\mathrm{kpc})^{0}} \cdot d_{uncorr} + \frac{0.1692}{(1\,\mathrm{kpc})^{1}} \cdot d_{uncorr}^2 & (6.5) \end{aligned}$$

Out of 203 SNRs within the GPS region, 157 are of shell type. For this reduced sample a distance is provided for 17 SNRs and for 137 more the distance can be calculated using the $\Sigma - D$ relation. The missing 3 SNRs lack information on the radio flux, which is needed for the distance calculation. Fig. 6.6(a) illustrates the distribution of calculated distances without correction. Since the correction on the distance derived from Fig. 6.5 is valid for distances up to 10 kpc only, SNRs with calculated distance greater than 10 kpc are excluded from the sample. The corrected distance distribution for calculated distances is shown in Fig. 6.6(b). The list of the remaining 55 SNRs is given in the appendix in Table A.1. In addition to the second order polynomial given in equation 6.5, an error is determined for each bin in Fig. 6.5, used later on to calculate the error on the calculated distance for the respective bin. The values and errors of each bin are listed in Table 6.1.

6.2 Observations with H.E.S.S.

Using data taken during the GPS and also from dedicated observations in the same field of view it is possible to study individual targets and search for TeV γ-ray emission from SNRs. In the following two different approaches are presented. First an individual analysis of H.E.S.S. data has been performed for each SNR position. The analysis follows the procedure described in chapter 4. The second approach is the use of skymaps in the range

Table 6.1: Bin values and errors extracted from Fig. 6.5.

Bin	Value	Error
1	-0.434226	± 0.575727
2	-0.88219	± 1.72913
3	-1.13615	± 1.10276
4	2.10558	± 1.09878
5	4.6171	± 0.889833

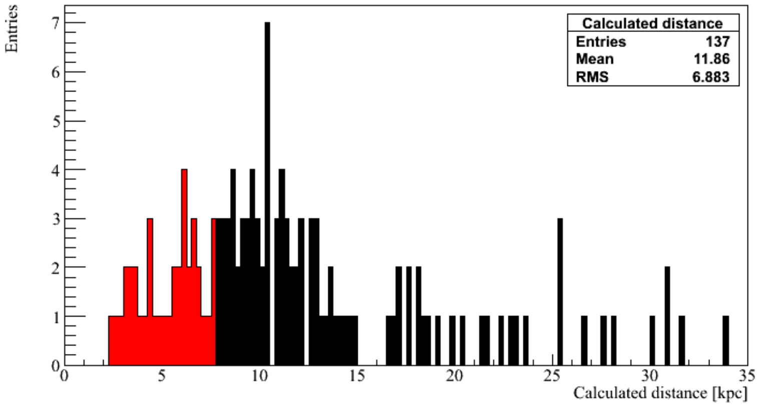

(a)

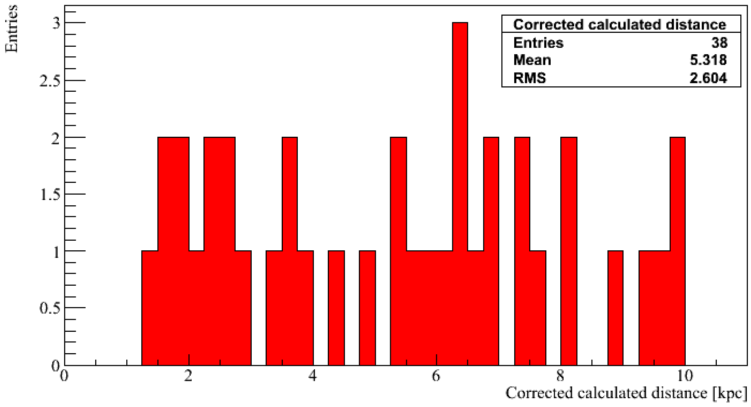

(b)

Figure 6.6: (a) The distribution of distances calculated for 137 shell type SNRs using the $\Sigma - D$ relation without correction and (b) with the correction derived from Fig. 6.5. The SNRs marked in red in (a) are those for which a correction can be given in (b).

of the GPS from which the significance of the γ-ray excess at the target positions can directly be extracted.

6.2.1 Analysis parameters for individual target analysis

In order to automatize the search for γ-rays from SNRs all necessary analysis parameters are set equal except for the integration radius, which is adapted individually. In detail the parameters are the following:

- **Maximum offset:** For each SNR only those runs, which are at most 2.5 ° away from the SNR position, are considered.
- **Selection cuts:** In order to keep the analysis automated and unbiased, the same selection cuts are applied to all SNRs. As described in section 4.2, *hard cuts* are optimized for point sources with a spectral index of 2.0 and a flux of ~1 % of the flux of the Crab pulsar. The SNRs in Green's catalog are expected to be weak sources in VHE γ-rays and to follow the overall cosmic ray spectrum of ~2.1. As shown in Fig. 6.4, most have a radius of less than 0.2 °. This justifies the use of hard cuts for the entire sample.
- **Integration radius θ^2:** It defines the size of signal integration. If the integration radius is chosen too large or too small compared to the size of the γ-ray emission region, the signal-to-noise ratio is not optimal. Therefore the integration radius of each SNR is determined individually for each SNR. The γ-ray emission region of SNRs is expected to be of the same size than the radio emission region. Therefore the integration radius is chosen as the remnant's radius adding 0.1 °, taking into account the point spread function (PSF) of the H.E.S.S. instrument.
- **Background method:** For each SNR position both the ring and the reflected background method are applied. These methods are described in section 4.3. The combination of the different background methods provides skymaps and spectra which are both necessary for the population study. Furthermore the use of two independent background methods provides a cross-check of the results, such as the number of excess events and the resulting significance.
- **Inner ring radius:** For regions with strong γ-ray emission the inner ring radius has to be chosen such that the ring is clearly outside the emission region, otherwise the background cannot be calculated and no signal can be extracted. To avoid too small inner ring radii for large SNRs, it is set to 0.9 ° for all SNRs.

6.2.2 Results of individual SNR analyses

The results of the individual analyses are summarized in the appendix in Table A.2. For each SNR the table lists the name, its type and radius, the duration of H.E.S.S. observations, the measured γ-ray flux and its derived upper limit, the measured γ-ray excess above the background with its significance as well as theoretical predictions of the γ-ray flux. Fig. 6.7 illustrates the significance distribution of all SNRs.

The distribution can be described by the sum of a Gaussian distribution centered at $1.21\,\sigma$ and a tail extending towards higher significances. In total, out of the 203 SNRs within the survey region, 47 show a signal with an excess of more than $5\,\sigma$ above the background. For each of these SNRs the nearest source or potential source from the H.E.S.S. database and its distance to the SNR together with the size of the SNR and

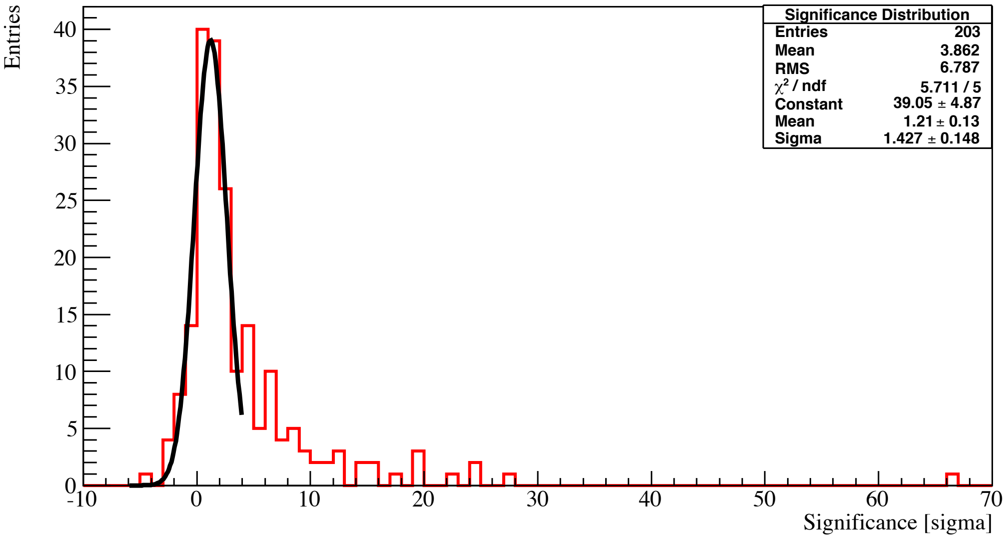

Figure 6.7: The significance distribution of the individual SNRs can be described by the sum of a Gaussian distribution centered around 1.21 σ and a tail extending towards higher significances. The highest significances correspond to detections of γ-ray sources at the Galactic Center, HESS J1713-397, HESS J1514-591, HESS J1813-178a, and HESS J1640-465.

the significance of the γ-ray excess at the SNR's position are listed in Table 6.2. The γ-ray emission regions listed in the H.E.S.S. database are *exclusion regions*, which are defined very conservatively around positions with significant γ-ray emission and do not always denote an actual γ-ray source but can also be due to statistical fluctuations. The distances between SNRs and these exclusion regions is defined as the angular distance between their centers.

Table 6.2: SNRs with a significance of the excess above 5σ. The distance between the SNR and the closest H.E.S.S. source is defined as the angular distance between their centers.

SNR	Name of closest H.E.S.S. source	H.E.S.S. gal. long. [deg]	H.E.S.S. gal. lat. [deg]	SNR Radius [deg]	Distance SNR – H.E.S.S. [deg]	Significance [σ]	Type of counterpart identified with closest H.E.S.S. source
G000.0+00.0	Galactic centre	0.0	-0.02	0.03	0.05	66.6	PWN
G000.3+00.0	Galactic centre	0.55	-0.05	0.1	0.24	12.6	–
G000.9+00.1	HESSJ1747-281	0.94	0.06	0.07	0.07	19.9	PWN
G001.0-00.1	Galactic centre	1.1	0.0	0.07	0.16	11.5	–
G001.4-00.1	Galactic centre	1.1	0.0	0.08	0.39	6.5	–
G006.4-00.1	HESSJ1801-233	6.66	-0.27	0.4	0.29	5.5	SNR W28
G008.3-00.0	HESSJ1804-216	8.36	-0.06	0.04	0.07	14.6	–
G008.7-00.1	HESSJ1804-216	8.36	-0.06	0.38	0.38	17.8	SNR/PSR
G011.0-00.0	HESSJ1809-193	11.04	-0.1	0.08	0.05	14.8	PWN
G011.1+00.1	HESSJ1809-193	11.04	-0.1	0.09	0.25	10.4	–
G011.2-00.3	HOTSJ1811-194	11.13	-0.25	0.03	0.11	5.5	–
G012.7-00.0	HESSJ1813-178	12.81	-0.03	0.05	0.09	19.3	–
G012.8-00.0	HESSJ1813-178	12.85	-0.02	0.02	0.02	24.3	PWN/SNR shell
G016.8-01.1	HESSJ1826-148	16.88	-1.28	0.23	0.24	19.8	X-ray bin. LS 5039
G017.0-00.0	HESSJ1825-137	17.48	-0.56	0.04	0.69	6.6	PWN

Continued on next page

Table 6.2 – continued from previous page

SNR	Name of closest H.E.S.S. source	H.E.S.S. gal. long. [deg]	H.E.S.S. gal. lat. [deg]	SNR Radius [deg]	Distance SNR – H.E.S.S. [deg]	Significance [σ]	Type of counterpart identified with closest H.E.S.S. source
G017.4-00.1	HESSJ1825-137	17.48	-0.56	0.05	0.44	12.6	PWN
G018.1-00.1	HESSJ1826-130	18.48	-0.42	0.07	0.42	6.9	–
G021.5-00.9	HESSJ1833-105	21.51	-0.88	0.03	0.03	6.4	PWN
G022.7-00.2	HOTSJ1832-093	22.51	-0.12	0.22	0.17	6.1	–
G023.3-00.3	HESSJ1834-087	23.24	-0.32	0.22	0.03	15.6	SNR
G024.7-00.6	HESSJ1837-069	25.18	-0.11	0.12	0.64	7.7	PWN
G027.4+00.0	HESSJ1841-055	26.82	-0.16	0.03	0.6	6.0	–
G028.6-00.1	HESSJ1843-033	28.99	0.15	0.09	0.45	7.1	–
G029.7-00.3	HESSJ1846-029	29.71	-0.24	0.02	0.01	10.1	PSR, SNR Kes75
G040.5-00.5	HESSJ1908+063	40.38	-0.79	0.18	0.31	8.0	PSR/SNR
G284.3-01.8	HESSJ1018-589	-75.69	-1.7	0.2	0.08	6.2	–
G292.2-00.5	HESSJ1119-614	-67.87	-0.56	0.15	0.04	6.4	PWN/SNR shell
G315.4-02.3	HESSJ1442-623	-44.55	-2.29	0.35	0.08	12.1	SNR, RCW 86
G318.2+00.1	HOTSJ1457-594	-41.65	-0.44	0.31	0.55	7.1	–
G320.4-01.2	HESSJ1514-591	-39.67	-1.2	0.29	0.05	27.2	PWN MSH 15-52
G320.6-01.6	HESSJ1514-591	-39.67	-1.2	0.4	0.49	8.6	–
G332.4+00.1	HESSJ1616-508	-27.58	-0.16	0.12	0.28	11.3	–
G332.4-00.4	HESSJ1616-508	-27.58	-0.16	0.08	0.2	9.9	–
G336.7+00.5	HESSJ1634-472	-22.91	0.2	0.1	0.47	5.5	–
G337.0-00.1	HESSJ1634-472	-22.91	0.2	0.01	0.35	6.2	–
G337.2+00.1	HESSJ1634-472	-22.91	0.2	0.02	0.17	7.7	–
G338.3-00.0	HESSJ1640-465	-21.7	-0.04	0.07	0.04	24.5	–
G338.5+00.1	HESSJ1641-462	-21.48	0.05	0.08	0.02	8.8	–
G343.1-02.3	HESSJ1708-442	-16.85	-2.37	0.27	0.08	5.9	PSR
G344.7-00.1	HESSJ1702-420	-15.3	0.1	0.08	0.26	5.4	(PWN)
G347.3-00.5	HESSJ1713-397	-12.78	-0.42	0.5	0.17	22.7	SNR
G348.5+00.1	HESSJ1714-385	-11.64	0.02	0.12	0.14	8.8	SNR CTB37A
G348.7+00.3	HESSJ1713-381	-11.35	0.4	0.14	0.01	9.1	SNR CTB37B
G353.6-00.7	HESSJ1731-347	-6.44	-0.71	0.25	0.06	15.6	SNR shell
G358.5-00.9	HESSJ1745-303	-1.54	-0.84	0.14	0.2	8.2	–
G359.0-00.9	HESSJ1745-303	-1.18	-0.82	0.19	0.21	6.6	–
G359.1-00.5	HESSJ1745-303	-1.15	-0.36	0.2	0.31	9.4	–

The SNRs showing a significant γ-ray signal can be divided into two groups. One group are those SNRs, which have been associated or even identified with the VHE γ-ray emission in the past, while the remaining SNRs have not been associated with any nearby γ-ray emission region. A firm identification based on a timing characteristic as required by Abdo et al. (2010) is not possible with H.E.S.S.. However, the morphological agreement between data from different wavelengths like in the case of shell-type SNRs like RX J1713.7-3946 (G347.3-00.5) and HESS J1731-347 (G353.6-00.7) supports an identification of the VHE γ-ray emission with the SNR. In other cases the positional coincidence and the comparable angular size of the VHE γ-ray emission region with the SNR radius suggest an association, like in the case of HESS J1714-385 (CTB 37A), HESS J1713-381 (CTB 37B), and HESS J1846-029 (SNR G029.7-00.3). Table 6.3 summarizes the SNRs that are presented in the following sections.

with SNR association	without SNR association	
G000.9+00.1	G000.0+00.0	G040.5-00.5
G006.4-00.1	G000.3+00.0	G318.2-00.1
G021.5-00.9	G008.7-00.1	G320.4-01.2
G023.3-00.3	G011.0-00.0	G332.4-00.4
G029.7-00.3	G012.8-00.0	G332.4+00.1
G284.3-01.8	G016.8-01.1	G337.2+00.1
G292.2-00.5	G017.4-00.1	G343.1-02.3
G315.4-02.3	G024.7-00.6	G344.7-00.1
G338.3-00.0	G027.4+00.0	G359.0-00.9
G347.3-00.5	G028.6-00.1	G359.1-00.5
G353.6-00.7		

Table 6.3: The H.E.S.S. sources with and without SNR association are further described in the following sections.

For each SNR the VHE γ-ray emission at the SNRs' positions is presented. Based on published H.E.S.S. results possible counterparts are discussed. The skymap derived from the analysis is presented, showing positions and sizes of the considered SNRs (red circles), nearby γ-ray emission regions (blue circles) and pulsars from the ATNF catalog (magenta circles). Only pulsars with a spin-down energy flux $\dot{E}/d^2 > 10^{32}\,\mathrm{erg\,s^{-1}\,kpc^{-2}}$ are considered here (Manchester et al. 2005).

The correlation radius is 0.1° for all skymaps. The green contour lines represent the excess level of the VHE γ-radiation in steps of 100 between 200 and 1100 events. The chosen scale and detail of the skymap has been adapted individually. The blue circles represent not only the source region of the respective H.E.S.S. source but illustrates the exclusion region used during the analysis, which includes the entire VHE γ-ray emission region.

6.2.3 H.E.S.S. detections associated with SNRs

HESS J1747-281, SNR G000.9+00.1, Fig. 6.8

HESS J1747-281 is one of the two γ-ray sources detected in the Galactic Centre region and shows a significance of the excess of ~20 σ after ~97 h of observation time. It has been presented by Aharonian et al. (2005a) and identified with the composite SNR G000.9+00.1. The point-like nature of the γ-ray emission and missing non-thermal X-ray emission from the SNR shell make the γ-radiation likely to originate from the pulsar wind nebula in G000.9+00.1.

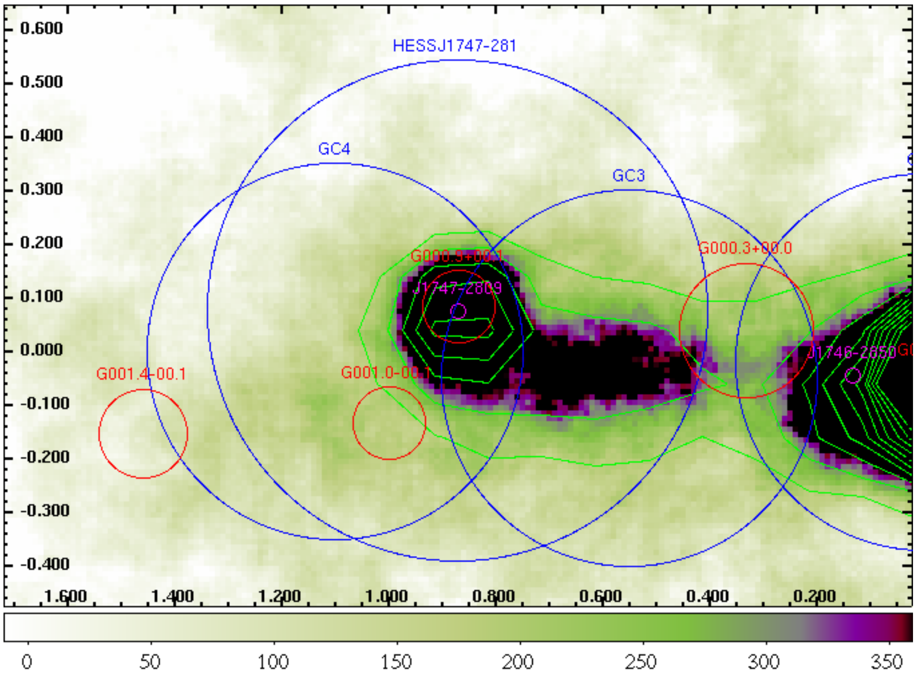

Figure 6.8: Excess map of G000.9+00.1. The detected γ-ray emission from the SNR is associated with the H.E.S.S. source HESS J1747-281.

HESS J1801-233 (W28), SNR G006.4-00.1, Fig. 6.9

In the complex field of view of the composite SNR G006.4-00.1 two H.E.S.S. sources and other SNRs are visible. The γ-ray emission from HESS J1801-233 has been reported by Aharonian et al. (2008d), where it has been associated with the old SNR W 28. The interaction with molecular clouds (Claussen et al. 1999) and high-density shocked gas (Reach et al. 2005) indicate a hadronic origin of the γ-radiation. The significance of the excess of G006.4-00.1 after ~20 h of observation time is 5.5 σ.

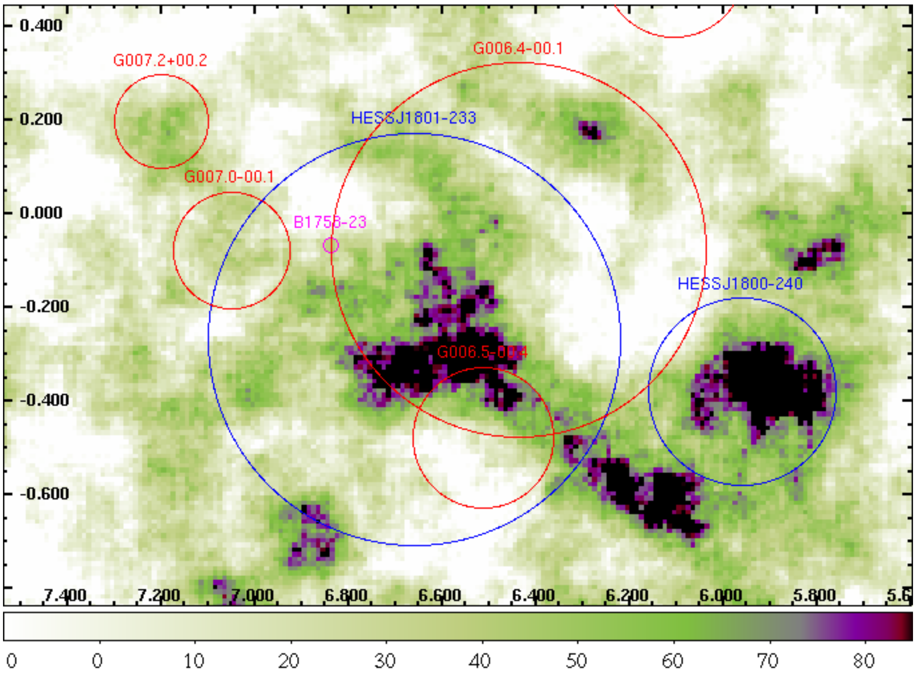

Figure 6.9: Excess map of G006.4-00.1. The γ-ray emission has been associated with the composite SNR G006.4-00.1, also known as W 28, and the interaction of the remnant with molecular clouds and high-density shocked gas. The nearby SNR G006.5-00.4 is too small to be a plausible counterpart for the VHE γ-ray emission.

HESS J1833-105, SNR G021.5-00.9, Fig. 6.10

The VHE γ-ray emission from the analysis of HESS J1833-105 has been reported by Djannati-Atai et al. (2007), where the association with the composite SNR G021.5-00.9 and a pulsar wind nebula powered by the coincident X-ray pulsar PSR 1833-1034 has been discussed. Current data at the position of the SNR yields a significance of the excess of 6.4σ after $\sim$27 h of observation time.

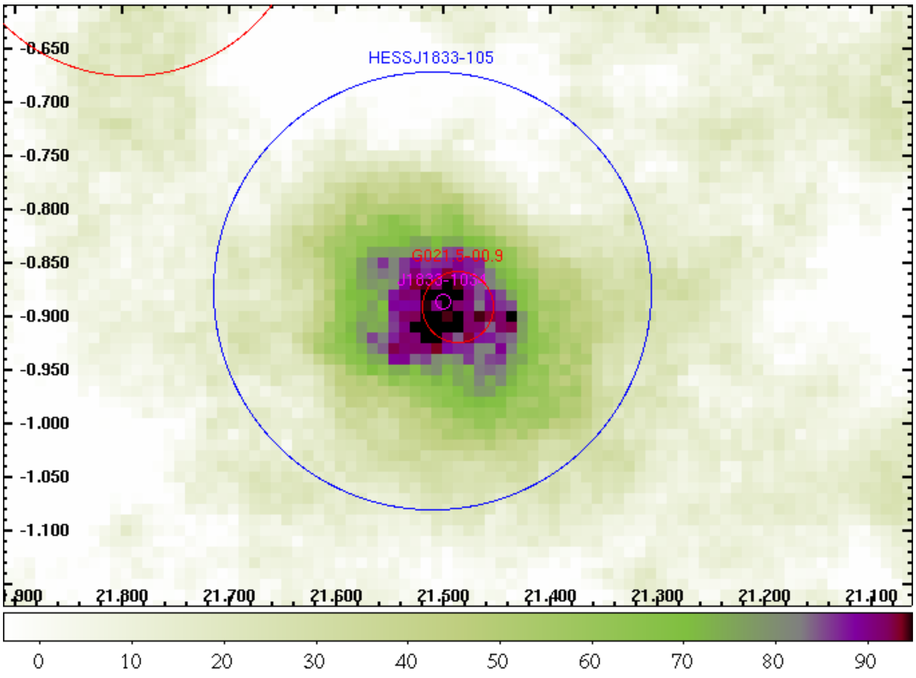

Figure 6.10: Excess map of G021.5-00.9. The composite SNR and the pulsar wind nebula powered by the pulsar PSR 1833-1034 have been associated with the γ-ray emission.

HESS J1834-087, SNR G023.3-00.3, Fig. 6.11

The analysis of the SNR G023.3-00.3 (also called W41) shows a significance of the excess of 15.6 σ after ~19 h of observation time. The discovery of the VHE γ-ray source HESS J1834-087 and the association with the SNR have been reported by Aharonian et al. (2005c) and Aharonian et al. (2006d)

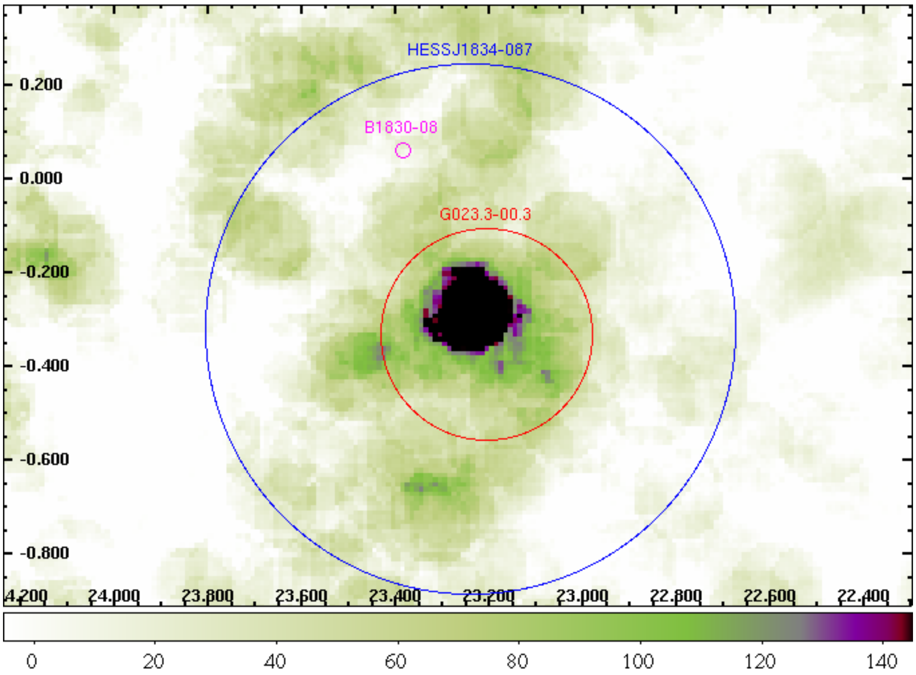

Figure 6.11: Excess map of G023.3-00.3. The VHE γ-ray source HESS J1834-087 (W 41) has been identified with this SNR.

HESS J1846-029, SNR G029.7-00.3, Fig. 6.12
The VHE γ-ray source HESS J1846-029 has been presented by Djannati-Atai et al. (2007). It is positionally coincident with the SNR Kes 75 (also known as G029.7-00.3). The γ-ray emission has been associated with the pulsar PSR J1846-258 Gotthelf et al. (2000). The significance of the γ-ray excess is 10 σ after ~36 h of observation time.

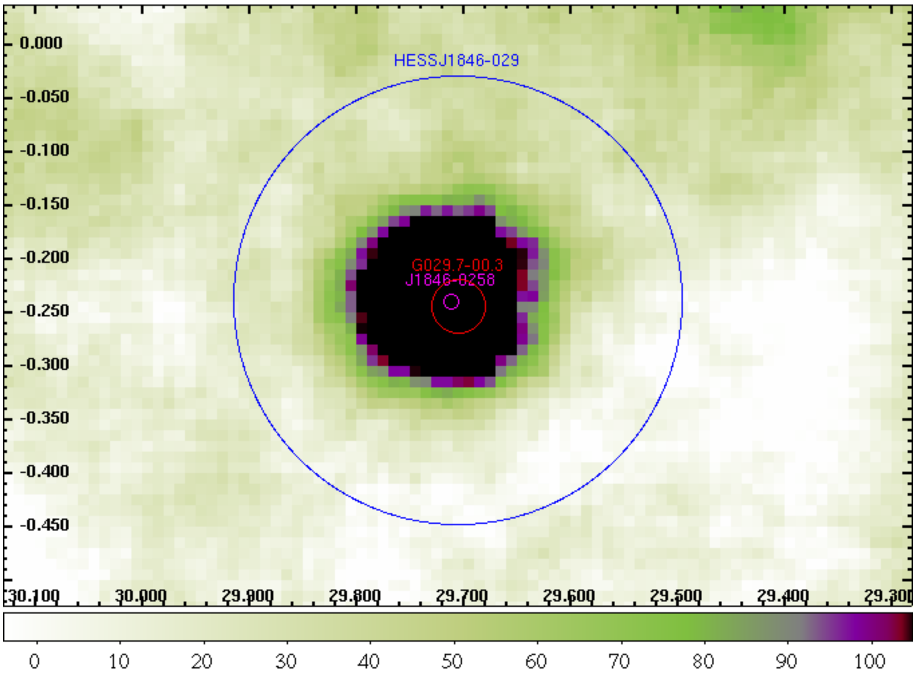

Figure 6.12: Excess map of G029.7-00.3. The SNR, also known as Kes 75, is associated with the pulsar PSR J1846-258.

HESS J1018-589, SNR G284.3-01.8, Fig. 6.13
The γ-ray source HESS J1018-589 is positionally coincident with the shell type SNR G284.3-01.8. Associations with the X-ray pulsar PSR J1016-5857 and its nebula (Camilo et al. 2001, 2004), the XMM Newton source XMMU J101855.2-58570, and the Fermi/LAT source 1FGL J1018.6-5856, which overlaps with the SNR (Abdo et al. 2010), have been discussed by (Wilhelmi et al. 2010). The significance of the γ-ray excess in the current data is $6.2\,\sigma$ after ~29 h of observation time.

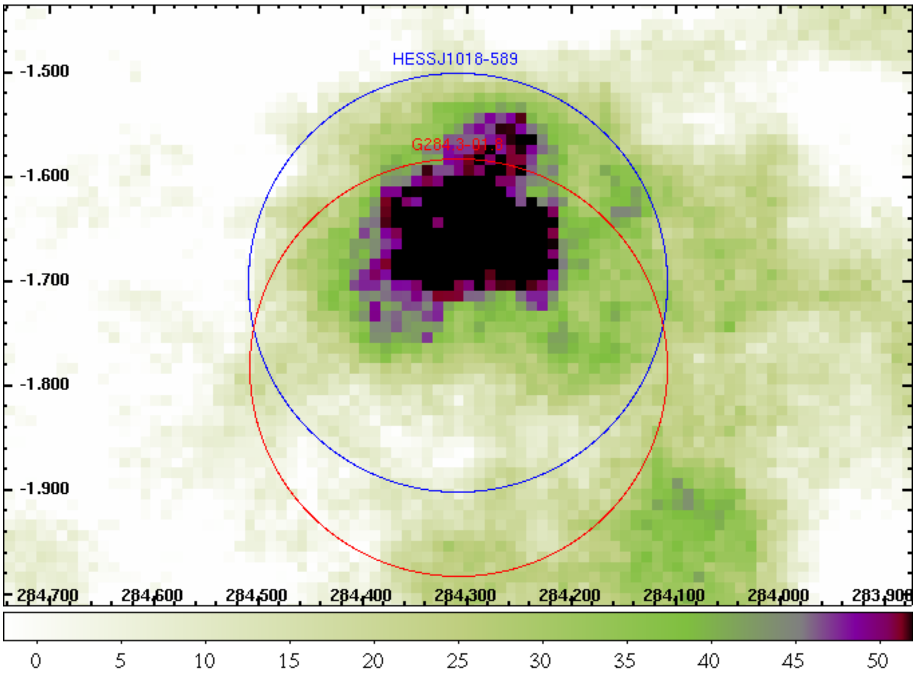

Figure 6.13: Excess map of G284.3-01.8. The shell type SNR and the pulsar wind nebula powered by the pulsar PSR 1016-5857 as well as the XMM Newton source XMMU J101855.2-58570 have been discussed as possible counterparts for the γ-ray emission.

HESS J1119-614, SNR G292.2-00.5, Fig. 6.14
During the Galactic Plane Survey with the H.E.S.S. detector, VHE γ-ray emission has been detected from HESS J1119-614 and an extended source coincident with the X-ray pulsar PSR J1119-6127 (Camilo et al. 2000) and the composite SNR G292.2-00.5 was confirmed. Possible scenarios of the origin of the TeV emission are an offset pulsar wind nebula or particles accelerated within the shell of the SNR, which interact with ambient gas. Analysis of H.E.S.S. data at the position of G292.2-00.5 yields a significance of the excess of 6.4σ after $\sim$27 h of observation time.

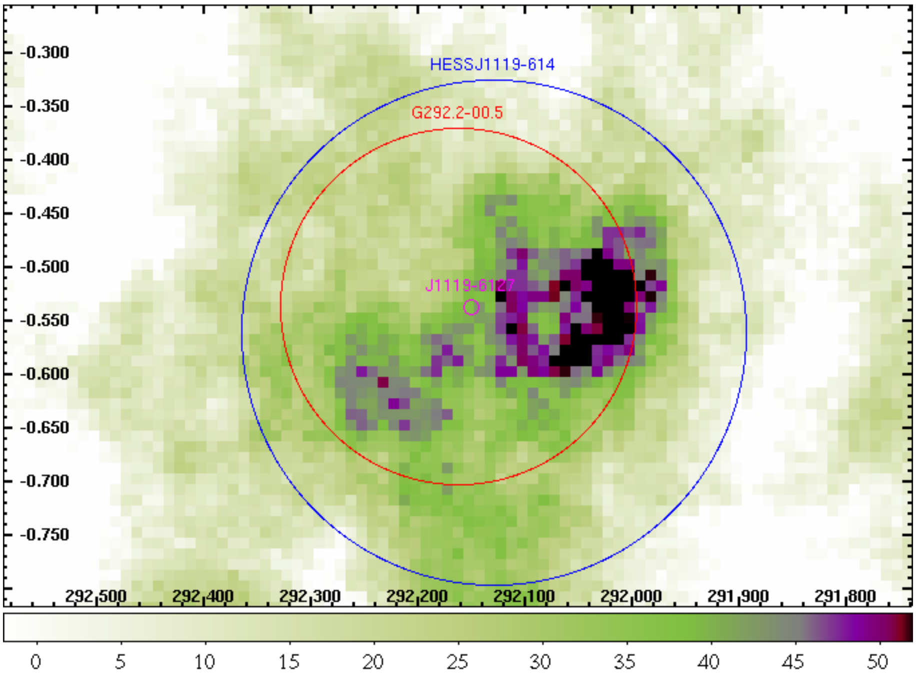

Figure 6.14: Excess map of G292.2-00.5. The composite SNR has been associated with the γ-ray emission from HESS J1119-614, which originates from an offset pulsar wind nebula or from particles accelerated within the shell.

HESS J1442-623 (RCW 86), SNR G315.4-02.3, Fig. 6.15

The shell type SNR RCW 86 has been observed in radio, optical and X-rays, where it shows a complete shell-like morphology, before being detected in VHE γ-rays (Aharonian et al. 2009b). The γ-ray emission also shows signs of a shell but does not correlate perfectly with the X-ray emission. After ∼40 h of observation time the significance of the excess amounts to 12σ.

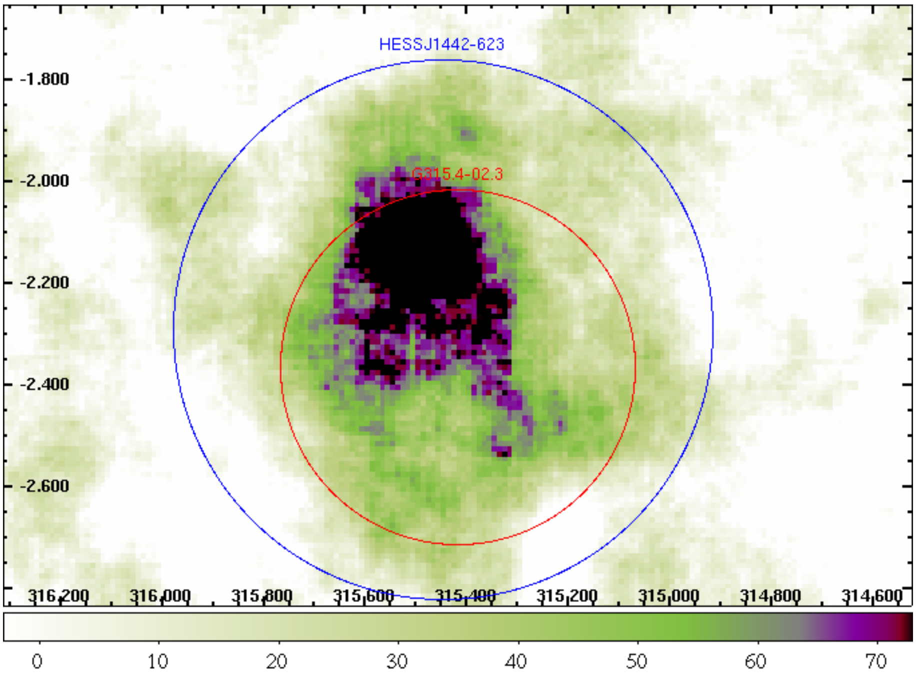

Figure 6.15: Excess map of G315.4-02.3. The shell type SNR is also named RCW 86 and has been detected in the radio, optical, and X-ray waveband and in γ-rays.

HESS J1640-465, SNR G338.3-00.0, Fig. 6.16

The γ-ray emission from HESS J1640-465 has been reported by Aharonian et al. (2005c). The significance of the excess after ~28 h of observation time is $24.5\,\sigma$. The γ-ray source has been associated with the source AX J164042-4632, detected during the Galactic plane survey of the ASCA satellite (Sugizaki et al. 2001b). The position of HESS J1640-465 is also compatible with the position of the unidentified EGRET source 3EG J1639-4702 (Hartman et al. 1999) and lies at the edge of a compact HII region, which has been observed during the Molonglo Galactic plane survey (Green et al. 1999). Another SNR, which also shows a significant excess is G338.5+00.1. It is positionally coincident with the VHE γ-ray source HESS J1641-462.

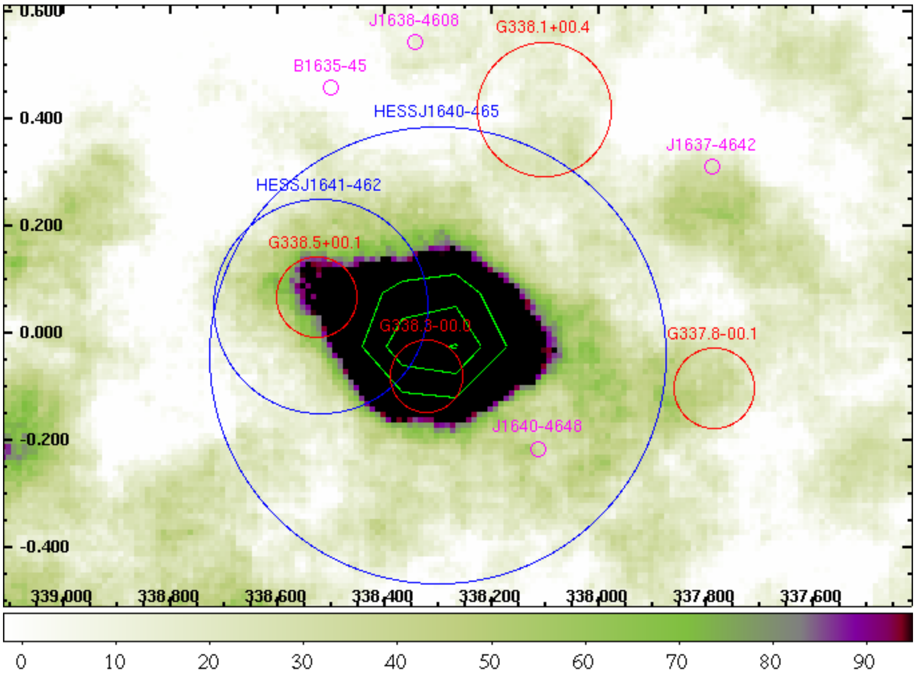

Figure 6.16: Excess map of G338.3-00.0. The γ-ray source HESS J1640-465 has been associated with this SNR.

HESS J1713-397, SNR G347.3-00.5, Fig. 6.17

The detection of VHE γ-rays from HESS J1713-397 is one of the most spectacular results of VHE γ-ray astronomy (Aharonian et al. 2004). After the detection of X-rays originating from the shell of the SNR by the X-ray satellite ROSAT (Voges et al. 1999) the spatial coincidence of the γ-ray emission region with the X-ray signal demonstrates the acceleration of VHE particles in the shell. Further observations provide a high precision on the morphological structure and the spectrum extends over almost three orders of magnitude with significant γ-ray emission approaching 100 TeV. Formally this implies the acceleration of primary particles up to this energy, however for realistic scenarios of VHE γ-ray production the measured gamma-ray energies imply that efficient acceleration of primary particles to energies exceeding 100 TeV is taking place in the shell of the SNR RX J1713.7-3946 (Aharonian et al. 2006b, 2007b). The significance of the excess at the position of G347.3-00.5 after ~5 h of observation time is 22.7 σ.

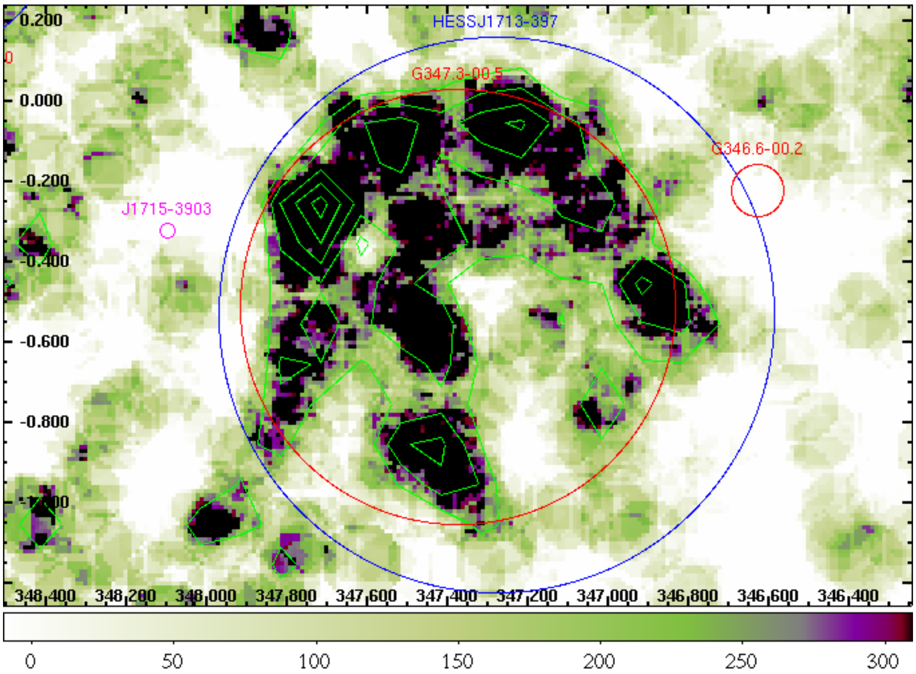

Figure 6.17: Excess map of G347.3-00.5. The γ-ray emission originates from the shell of the SNR as the spatial coincidence of the shell-like morphology of the γ-ray emission region with X-ray observations demonstrates.

HESS J1714-385 (CTB 37A), SNR G348.5+00.1 and HESS J1713-381 (CTB 37B), SNR G348.7+00.3, Fig. 6.18

In the vicinity of the SNR RX J1713.7-3946 are two more SNRs, CTB 37A and CTB 37B. HESS J1714-385 coincides with the SNR CTB 37A, also known as G348.5+00.1, and has been reported by Aharonian et al. (2008b). Although the γ-ray emission is likely to be associated with the SNR, different scenarios explaining the γ-ray emission are possible. Radio and X-ray data reveal the interaction of the supernova blast wave with molecular clouds and the presence of OH masers. A hadronic origin of the γ-radiation is more likely, but a leptonic origin cannot be ruled out. The analysis after ∼50 h of observation time yields a significance of the excess of $8.8\,\sigma$. HESS J1713-381 was first reported by Aharonian et al. (2006d) and is positionally coincident with the SNR CTB 37B alias G348.7+0.3. Aharonian et al. (2008c) have discussed in more detail the association of the γ-ray emission with possible counterparts and the most likely hadronic origin of the γ-radiation. The significance of the excess amounts to $9\,\sigma$ after ∼54 h of observation time.

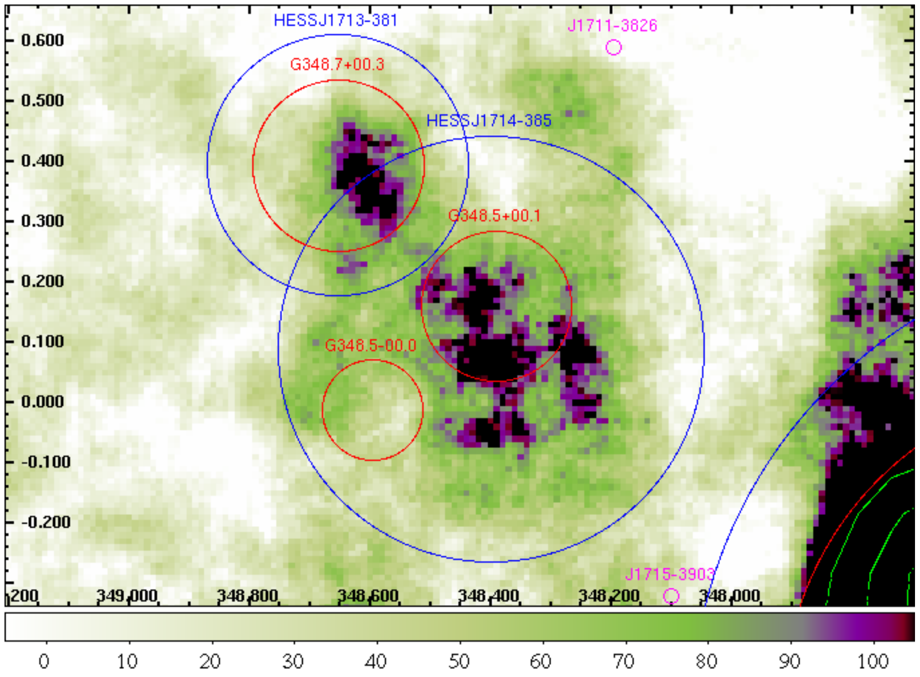

Figure 6.18: Excess map of G348.5+00.1 and G348.7+00.3. The VHE γ-ray sources HESS J1714-385 and HESS J1713-381 have been associated with these SNRs.

HESS J1731-347, SNR G353.6-00.7, Fig. 6.19

The γ-ray source HESS J1731-347, formerly presented as an unidentified H.E.S.S. source by Aharonian et al. (2008a), has been identified with the SNR G353.6-00.7 by Tian et al. (2008) in radio and X-ray data. It is the first shell-type SNR which has been discovered on the basis of VHE γ-ray observations. Since no sign of a pulsar or pulsar wind nebula has been detected in other wavelengths, the γ-radiation most likely originates from the SNR. The estimated age is of ~27000 years, which proves that an old SNR emits VHE γ-rays. The analysis of G353.6-00.7 yields a significance of the excess of 15.6σ after ~23 h of observation time.

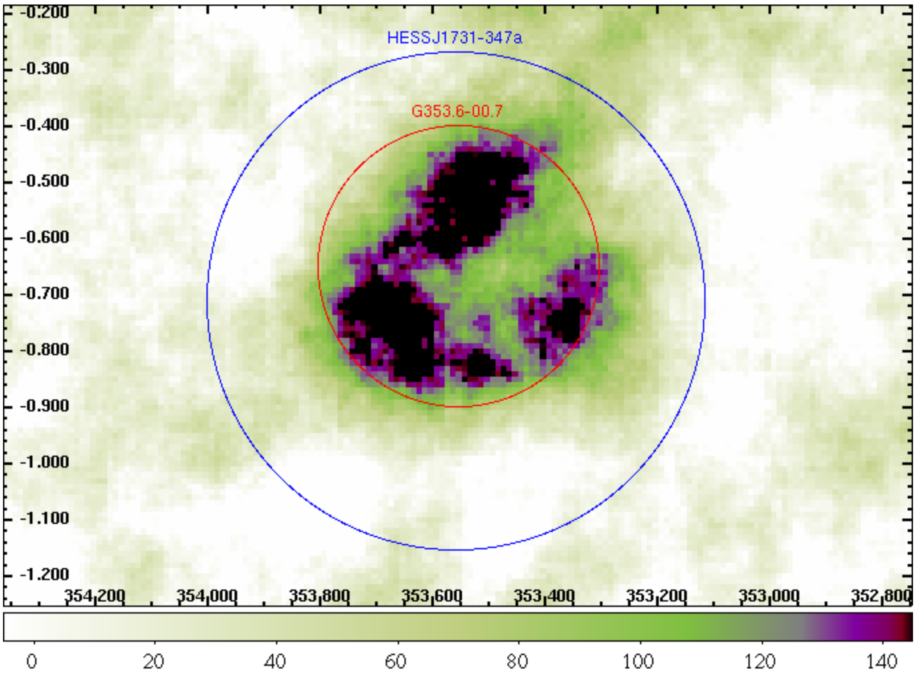

Figure 6.19: Excess map of G353.6-00.7. The SNR has first been discovered in VHE γ-rays as HESS J1731-347 and only later been detected in radio and X-ray data.

6.2.4 H.E.S.S. detections without association with SNRs

Galactic Centre, G000.0+00.0, Fig. 6.20

The large VHE γ-ray emission region associated with the Galactic Centre (GC) is spread over an area of $\sim 2^\circ \times 1^\circ$ in galactic longitude and latitude, respectively and has been observed far more than 120 h between 2004 and 2006. The detection of VHE γ-ray emission has been announced by Aharonian et al. (2006c). Within the GC region two point-like γ-ray sources have been detected by H.E.S.S.. One is associated to the SNR G000.9+00.1 and has been discussed in the previous section. The second known VHE γ-ray source HESS J1745-290 is associated with Sgr A*. The position of the γ-ray emission has been discussed by van Eldik et al. (2008) and SNR G000.00+00.0 as the source of γ-radiation could be ruled out. In the entire GC region dense and massive molecular clouds (Sgr A, B and C) provide efficient targets for diffuse cosmic rays and lead to γ-ray production via the decay of neutral pions.

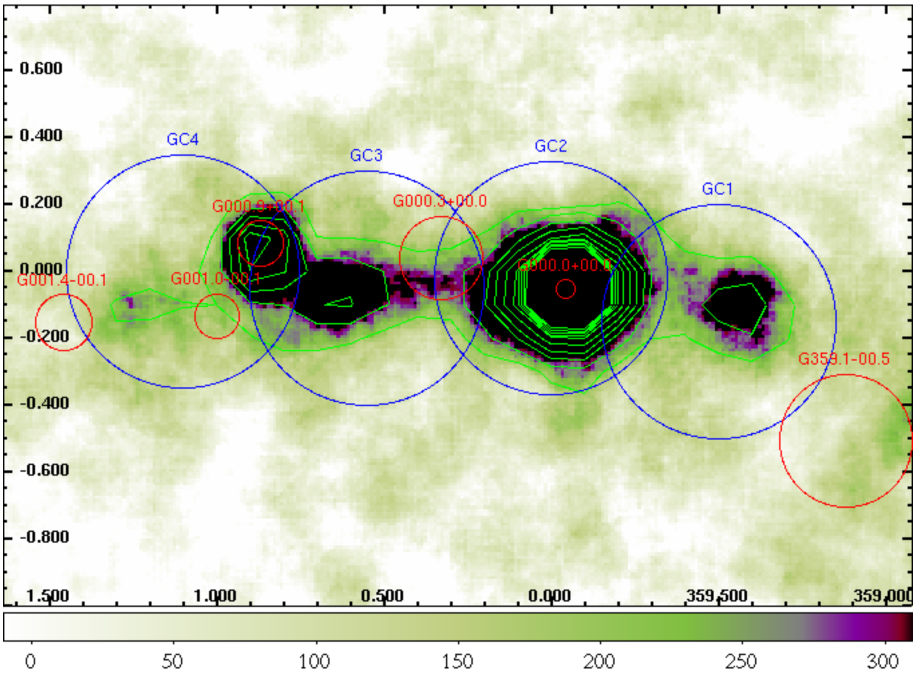

Figure 6.20: Excess map of the Galactic Centre. SNRs confused with the emission from the Galactic Centre are G000.0+00.0, G000.3+00.0, G000.9+00.1, G001.0-00.1, and G001.4-00.1. The four blue circles illustrate the exclusion regions used for the entire Galactic Centre region.

HESS J1745-303, G359.1-00.5/G359.0-00.9, Fig. 6.21

Close to the GC the H.E.S.S. source HESS J1745-303 has been associated with the unidentified EGRET source 3EG J1744-3011 (Aharonian et al. 2006d). Two exclusion regions around this source are defined, HESS J1745-303a and HESS J1745-303b. The significance obtained for the SNRs G359.1-00.5 and G359.0-00.9 is due to spill-over events from the nearby γ-ray emission region but the SNRs are not associated to the H.E.S.S. source. The significance of the excess at the SNRs' positions is $9\,\sigma$ and $6\,\sigma$ after ~91 h and ~71 h of observation time, respectively.

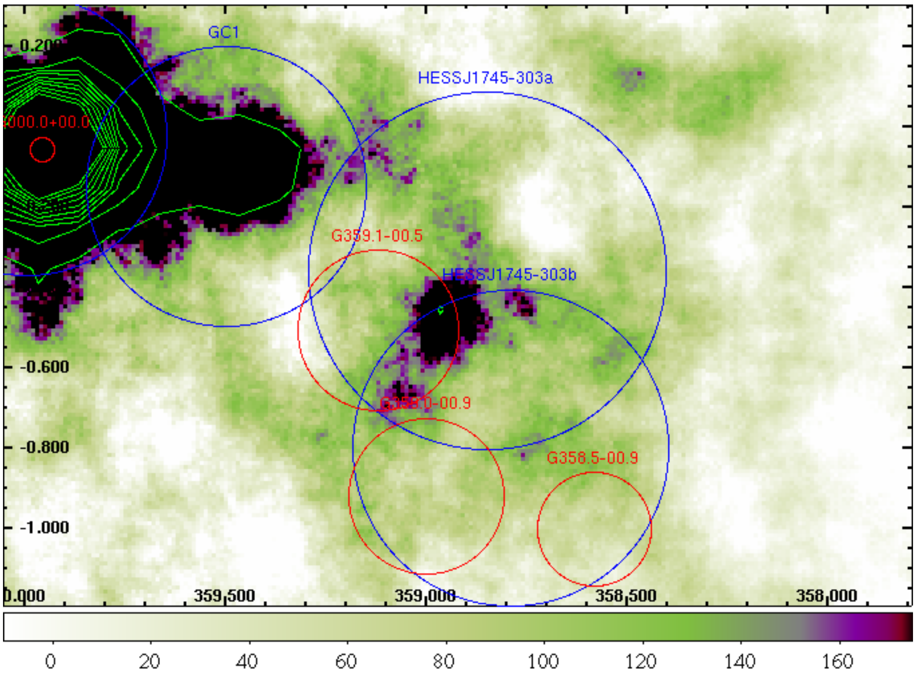

Figure 6.21: Excess map of the G359.1-00.5. The SNRs G359.1-00.5 and G359.0-00.9 are not associated with the γ-ray emission, which has been identified with the EGRET source 3EG J1744-3011.

HESS J1804-216, SNR G008.7-00.1, Fig. 6.22

The significance of the γ-ray excess at the position of the SNR G008.7-00.1 is of 17.8 σ after $\sim$ 23 h of observation time. The VHE γ-ray source HESS J1804-216 has been discussed by Aharonian et al. (2006d). It can be associated with the southwestern part of the shell of the SNR G008.7-00.1 or with the young pulsar PSR J1803-2137. Other nearby SNRs are the SNR G008.3-00.0 and the SNR G008.9+.00.4, which are too small or too far away from the γ-ray emission region for being plausible counterparts.

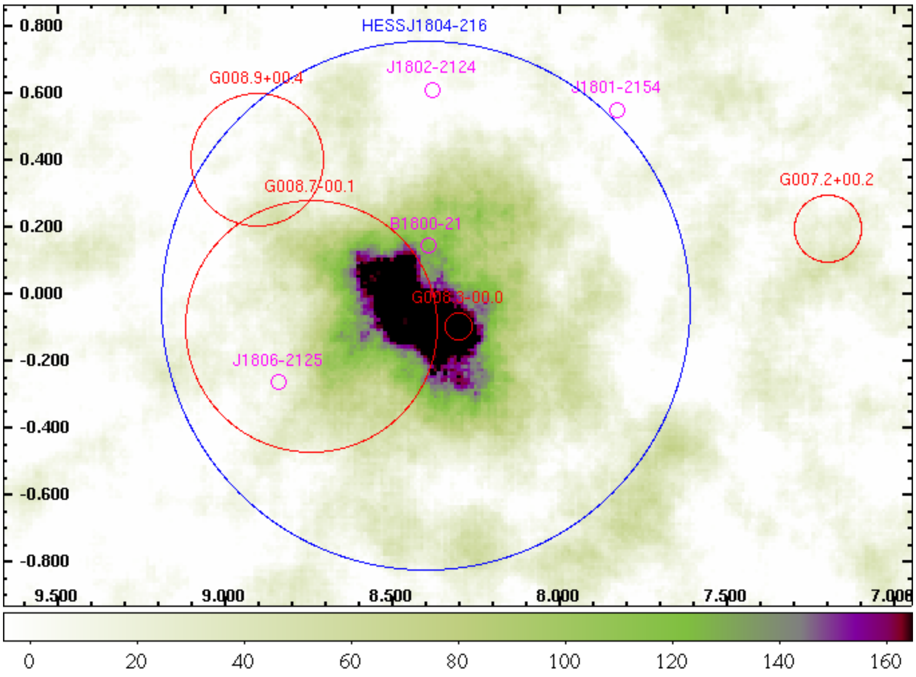

Figure 6.22: Excess map of G008.7-00.1. The nearby H.E.S.S. source HESS J1804-216 has been discussed to be associated with the southwestern part of the shell of G008.7-00.1 or with the pulsar PSR J1803-2137 (Aharonian et al. 2006d). Other nearby SNRs are G008.3-00.0 and G008.9+.00.4.

HESS J1809-193, SNR G011.0-00.0, Fig. 6.23

The detection of HESS J1809-193 has been presented by Aharonian et al. (2007a). The VHE γ-ray emission region has been associated with the pulsar wind nebula powered by the pulsar PSR J1809-1917. Several SNRs are nearby this pulsar, but the composite SNR G011.0-00.0 is stated as the most likely association. The significance of the VHE γ-ray excess at the position of the SNR G011.0-00.0 is of 14.7σ after $\sim$39 h of observation time.

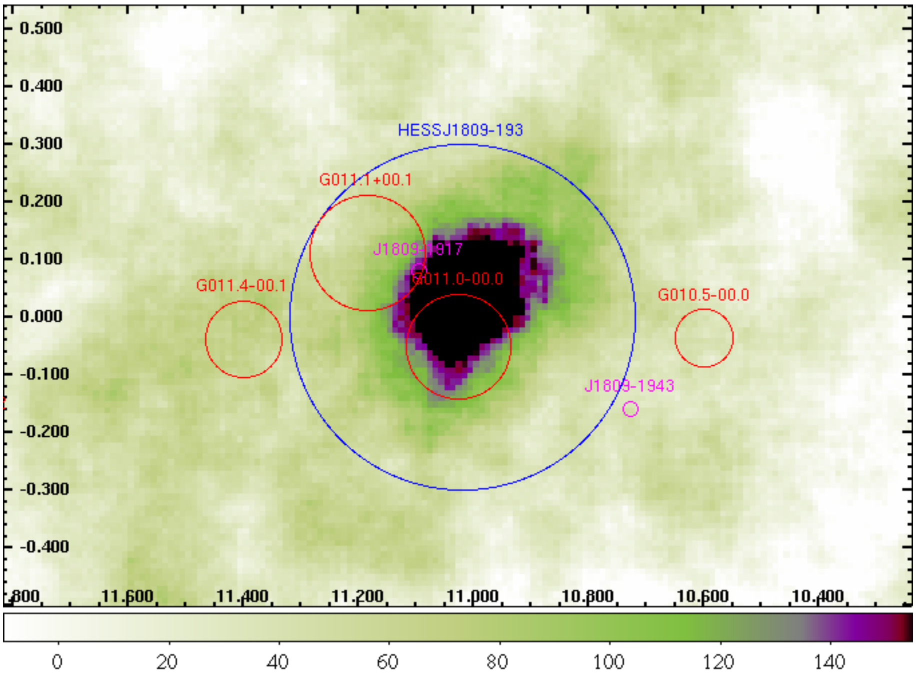

Figure 6.23: Excess map of G011.0-00.0 with a correlation radius of 0.1 ° The VHE γ-ray source HESS J1809-193 has been associated with the pulsar wind nebula of the pulsar PSR J1809-1917. The composite SNR G011.0-00.0 coincides with the peak of the VHE γ-ray emission. The other SNRs within the field of view are unlikely counterparts for the H.E.S.S. source.

HESS J1813-178, SNR G012.8-00.0, Fig. 6.24

HESS J1813-178 has been discovered by Aharonian et al. (2005c) and following the spatial coincidence has been associated with the X-ray source AX J1813-178 by Aharonian et al. (2006d). The γ-ray emission can also be associated with the shell type SNR G012.8-00.0, which is the compact radio core of the W33 region. The significance of the excess at the position of G012.8-00.0 after 19.4 h of observation time is 24.3σ.

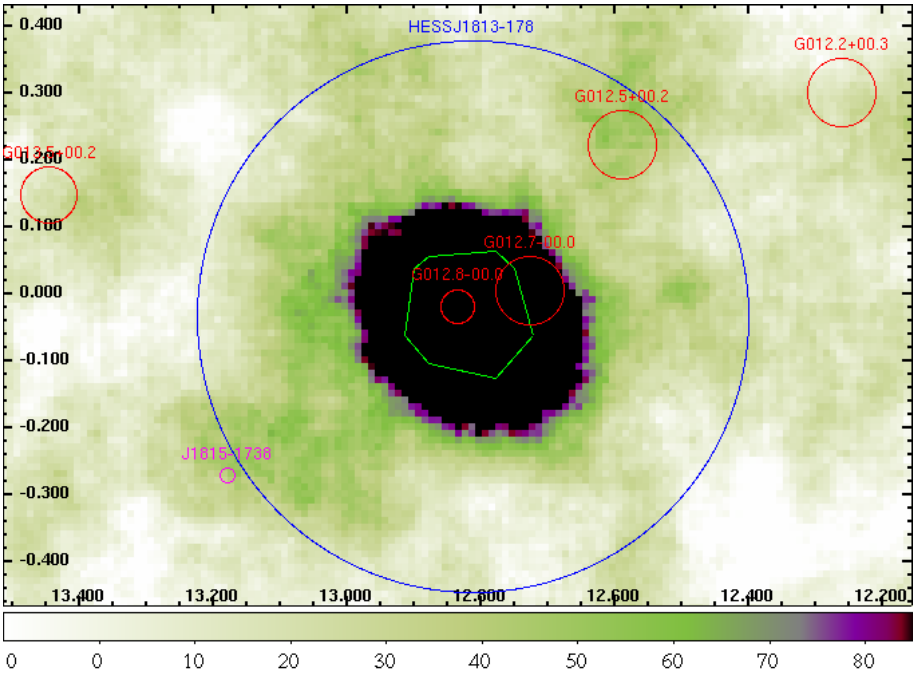

Figure 6.24: Excess map of G012.8-00.0. The γ-ray source HESS J1813-178 has been associated with the X-ray source AX J1813-178 (Aharonian et al. 2006d). The nearby SNR G012.7-00.0 also shows a significant γ-ray signal, which results from the spatial coincidence but is not associated with the H.E.S.S. source.

HESS J1826-148, SNR G016.8-01.1, Fig. 6.25

After 44.6 h of observation time the significance of the excess of HESS J1826-148 amounts to ~20 σ. The γ-ray emission has been associated to the high-mass X-ray binary LS 5039, which was discovered by Motch et al. (1997) using the cross-correlation of X-ray sources from the ROSAT catalog with OB star catalogues. In VHE γ-rays it is the first time that orbital modulation has been observed and that a periodicity of the γ-ray signal has been observed with ground-based detectors. The period is of 3.9 days. The positions of the SNR G016.8-01.1 and the pulsar PSR B1822-14, which are both plausible γ-ray sources, are inconsistent with the position of HESS J1826-148 (Aharonian et al. 2005d).

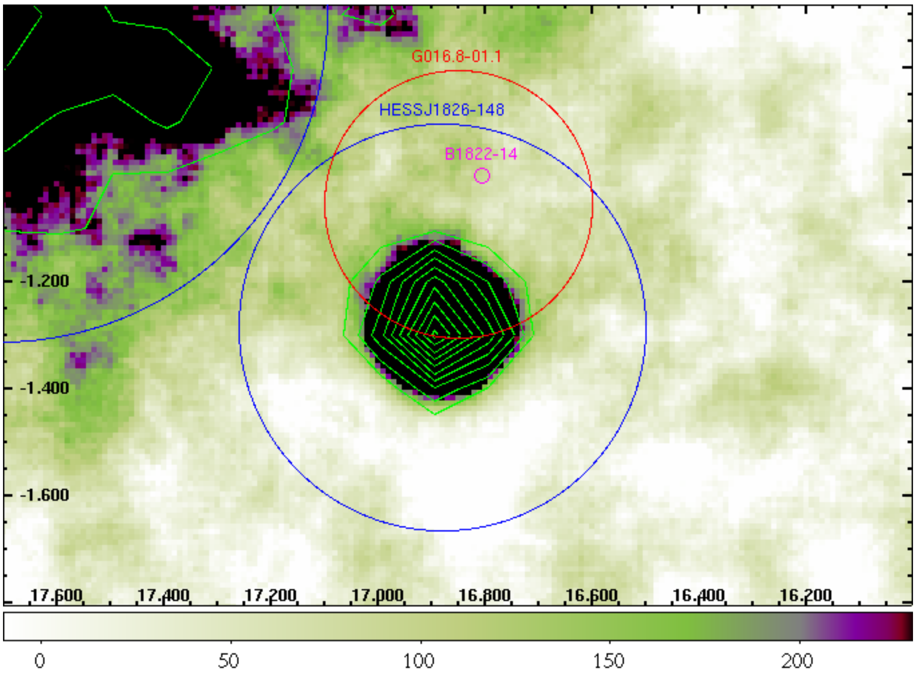

Figure 6.25: Excess map of G016.8-01.1. The γ-ray emission has been associated with the X-ray binary LS 5039 (Aharonian et al. 2006e).

HESS J1825-137, SNR G017.4-00.1, Fig. 6.26

The VHE γ-ray source HESS J1825-137 has been discovered by Aharonian et al. (2005c). The asymmetric form of the γ-ray emission region shows a tail towards the south, which is remarkably similar to the situation in X-rays (Finley et al. 1996; Gaensler et al. 2003). The most likely counterpart is the pulsar wind nebula G18.0-0.7 powered by the pulsar PSR B1823-13 (also known as PSR J1826-1334). This association has been discussed by (Aharonian et al. 2005g) and Aharonian et al. (2006f). The nearby SNRs G017.4-00.1 and G017.0-00.0, which show a significant excess, are not associated with the VHE γ-ray emission. The significance of the γ-ray excess is 12.6 σ after 51 h of observation time.

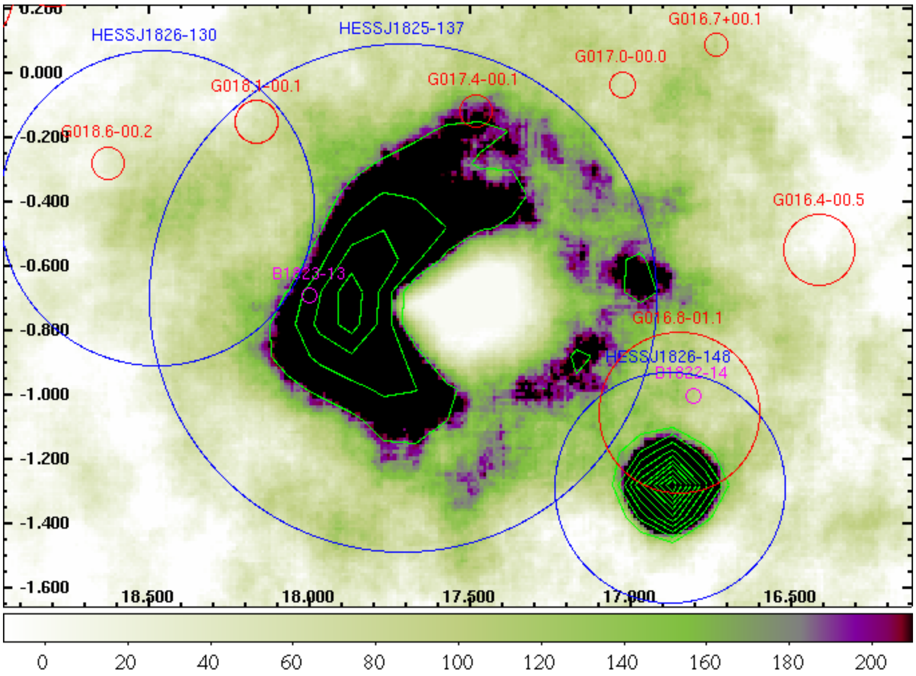

Figure 6.26: Excess map of G017.4-00.1. The VHE γ-ray source has been associated with the pulsar wind nebula G18.0-0.7 powered by the pulsar PSR 1823-13. The SNRs in the field of view are no plausible counterparts for the γ-radiation. The "hole" in the center of the emission region indicates the use of a too small ring radius, which does not allow to determine the VHE γ-ray excess in this area.

HESS J1837-069, SNR G024.7-00.6, Fig. 6.27
The extended VHE γ-ray source HESS J1837-069, which has been reported by Aharonian et al. (2006d), coincides with two X-ray sources detected in the ASCA Galactic Plane Survey (Sugizaki et al. 2001a), AX J1838.0-0655 and AX J1837.3-0.652. At the location of AX J1838.0-065 Gotthelf & Halpern (2008) find a strong X-ray point-source and an extended X-ray nebula. The search for pulsed emission lead to the discovery of the pulsar PSR J1838-0655. The significance of the excess at the position of G024.7-00.6 is 7.7 σ after ~24 h of observation time.

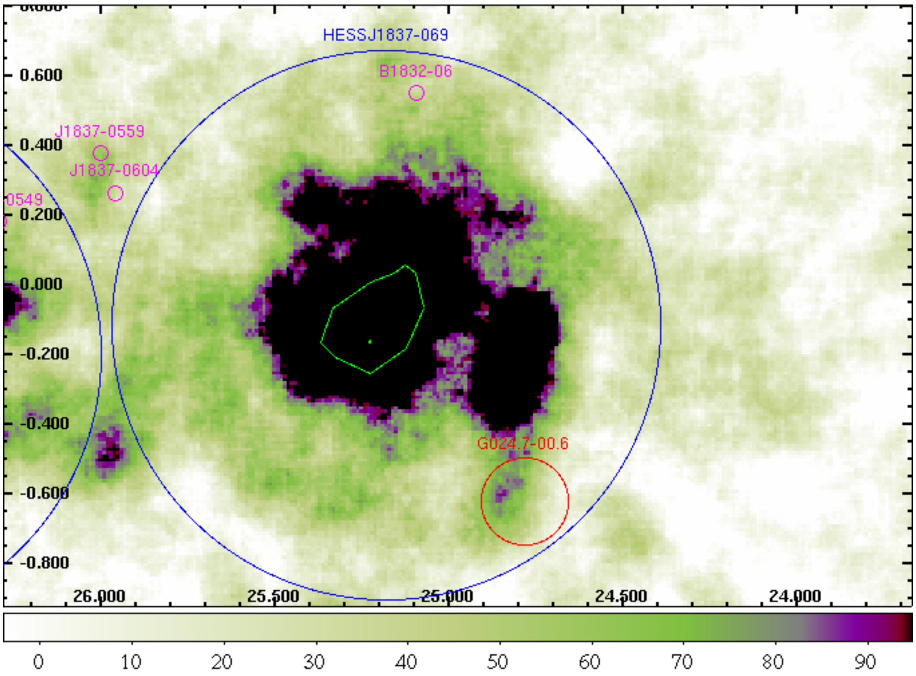

Figure 6.27: Excess map of G024.7-00.6. The γ-ray emission of HESS J1837-069 is not associated with the SNR but rather with the pulsar PSR J1838-0655 and its nebula.

HESS J1841-055, SNR G027.4+00.0, Fig. 6.28

HESS J1841-055 has been reported as an unidentified VHE γ-ray source by Aharonian et al. (2008a). Possible counterparts, such as the SNR G027.4+00.0, but also nearby pulsars, pulsar wind nebulae, an X-ray binary, and a HII region have been discussed. The significance of the excess at the position of G027.4+00.0 is 6 σ after ~25 h of observation time.

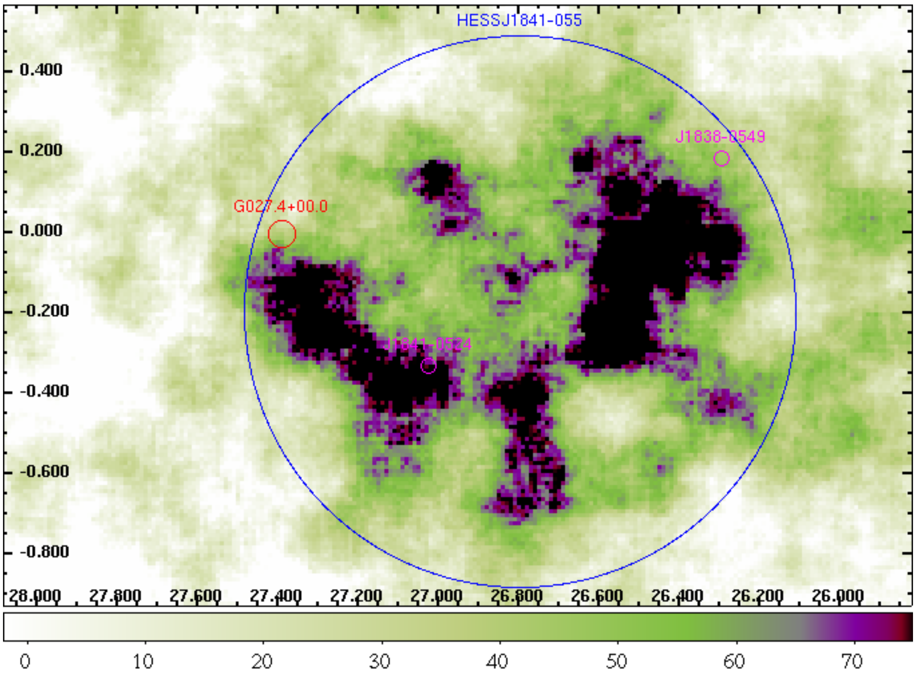

Figure 6.28: Excess map of G027.4+00.0. There has so far not been cofirmed a counterpart to the γ-ray emission of HESS J1841-055.

HESS J1843-033, SNR G028.6-00.1, Fig. 6.29

The VHE γ-ray emission region HESS J1843-033 is in the same field of view as HESS J1846-029 (Kes 75) but until now no plausible counterpart has been found for the source. The significance of the excess at the position of G028.6-00.1 is $7\,\sigma$ after 33 h of observation time.

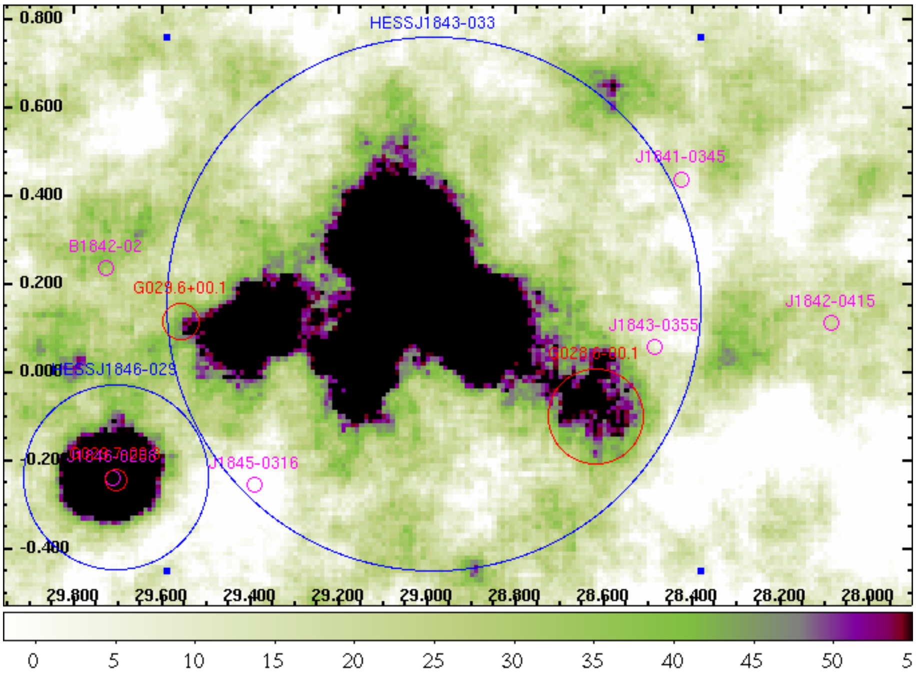

Figure 6.29: Excess map of G028.6-00.1. Until now no plausible counterpart has been found for the VHE γ-ray emission region HESS J1843-033.

HESS J1908+063, SNR G040.5-00.5, Fig. 6.30

The detection of VHE γ-rays from HESS J1908+063 (Aharonian et al. 2009a) has confirmed the discovery of MGRO J1908+06 by the Milagro collaboration (Abdo et al. 2007). Possible counterparts that have been discussed in the publication are the SNR G040.5-00.5, the γ-ray pulsar 0FGL J1907.5+0602 reported by the Fermi/LAT collaboration (Abdo et al. 2009), and the EGRET GeV source GRO J1908+0556/GEV J1907+0557 (Lamb & Macomb 1997). The significance of the excess at the position of G040.5-00.5 is 8 σ after ~29 h of observation time.

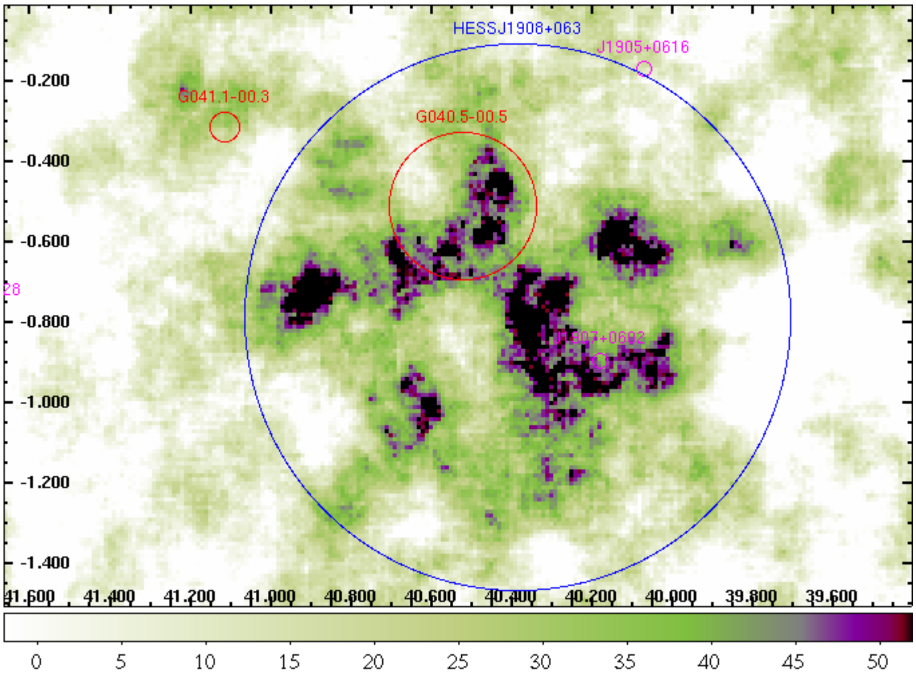

Figure 6.30: Excess map of G040.5-00.5. The H.E.S.S. source HESS J1908+063 has confirmed the discovery of the Milagro source MGRO J1908+06, but different counterparts are possible, such as the SNR G040.5-00.5, the EGRET source GRO J1908+0556 and the Fermi/LAT pulsar 0FGL J1907.5+0602.

HESS J1457-594, SNR G318.2-00.1, Fig. 6.31

The VHE γ-ray emission region HESS J1457-594 is currently under investigation. The significance of the excess at the position of G318.2-00.1 is $7\,\sigma$ after ~32 h of observation time.

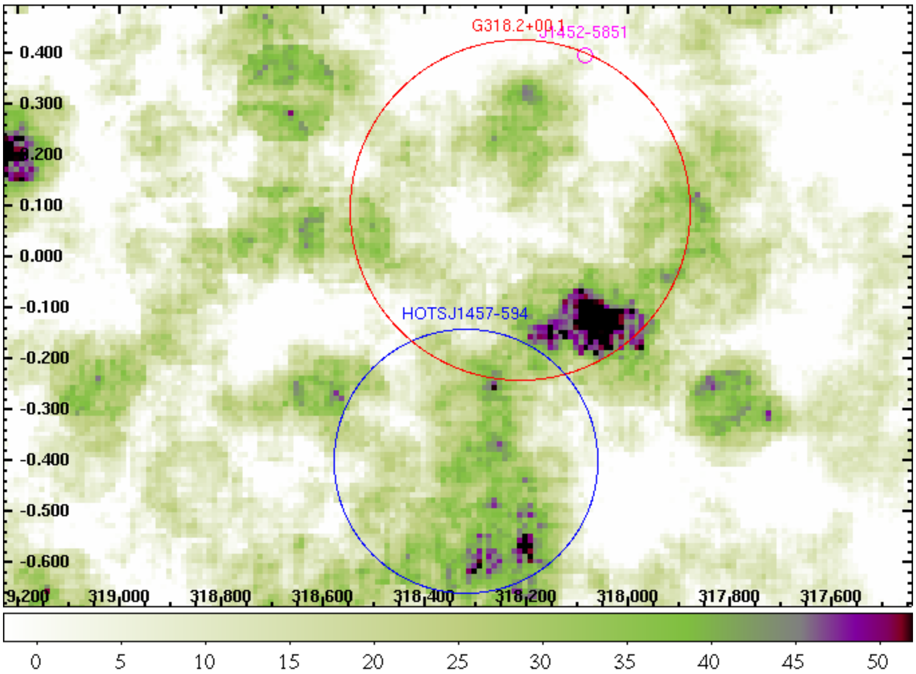

Figure 6.31: Excess map of G318.2-00.1. No counterpart of the γ-ray emission has been confirmed.

HESS J1514-591 (MSH 15-52), SNR G320.4-01.2, Fig. 6.32

HESS J1514-591 has been reported by Aharonian et al. (2005f). The morphology of the γ-ray emission region coincides with the pulsar wind nebula around PSR B1509-58, which has been observed in X-ray energies by ROSAT (Trussoni et al. 1996). The γ-ray emission, being elongated along the jet axis of the pulsar, can be explained by inverse Compton scattering of relativistic electrons on low energy photons. The SNR G320.6-01.6 is partly coincident with MSH 15-52 but is not associated with the γ-ray emission. The significance of the excess amounts to $\sim$27 σ after 25 h of observation time.

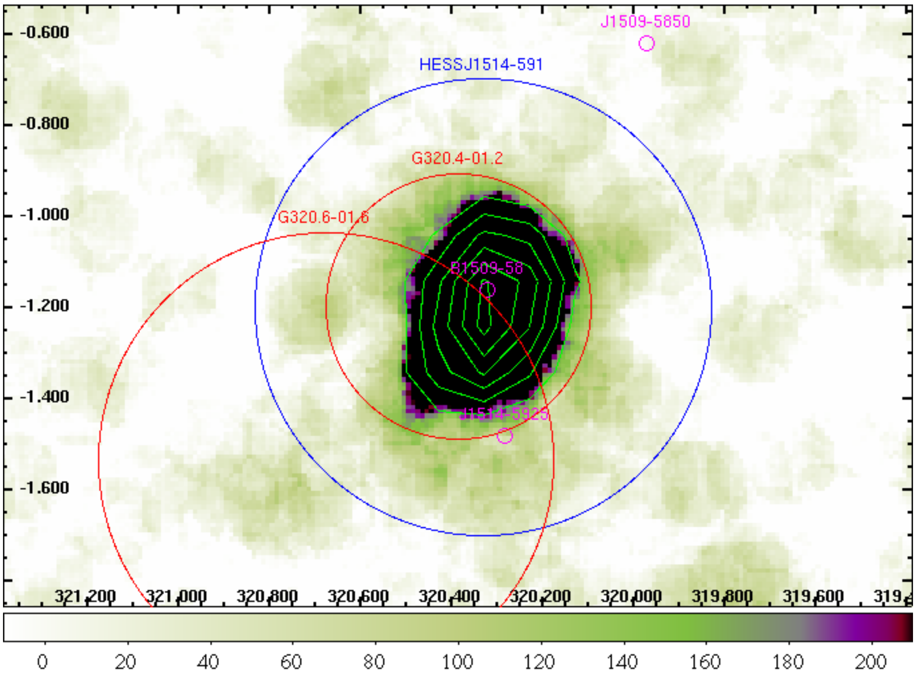

Figure 6.32: Excess map of G320.4-01.2. The extended γ-ray emission is associated with the pulsar wind nebula MSH 15-52 (HESS J1514-591 in the H.E.S.S. catalog). The analysis of the SNR G320.6-01.6 also shows significant excess, which most likely results from a spill-over from the γ-ray emission region.

HESS J1616-508, SNR G332.4+00.1/G332.4-00.4, Fig. 6.33

The VHE γ-ray source HESS J1616-508 has been reported by Aharonian et al. (2006d). Although several associations are possible, such as the SNRs G332.4+00.1 and G332.4-00.4 and the young pulsar PSR J1617-5055 (Torii et al. 1998), none of these have been confirmed as counterparts. A possible scenario is the asymmetric location of the γ-ray emission with respect to the pulsar, as has been observed in other cases. An alternative explanation for γ-ray sources without radio or X-ray counterparts can be given for old SNRs, where electron acceleration cannot compete with radiation cooling and where γ-rays are produced in proton interactions (Yamazaki et al. 2006). The significances of the γ-ray excess at the positions of G332.4+00.1 and G332.4-00.4 are 11.3 σ and 9.9 σ after 7.6 h and 7 h of observation time, respectively.

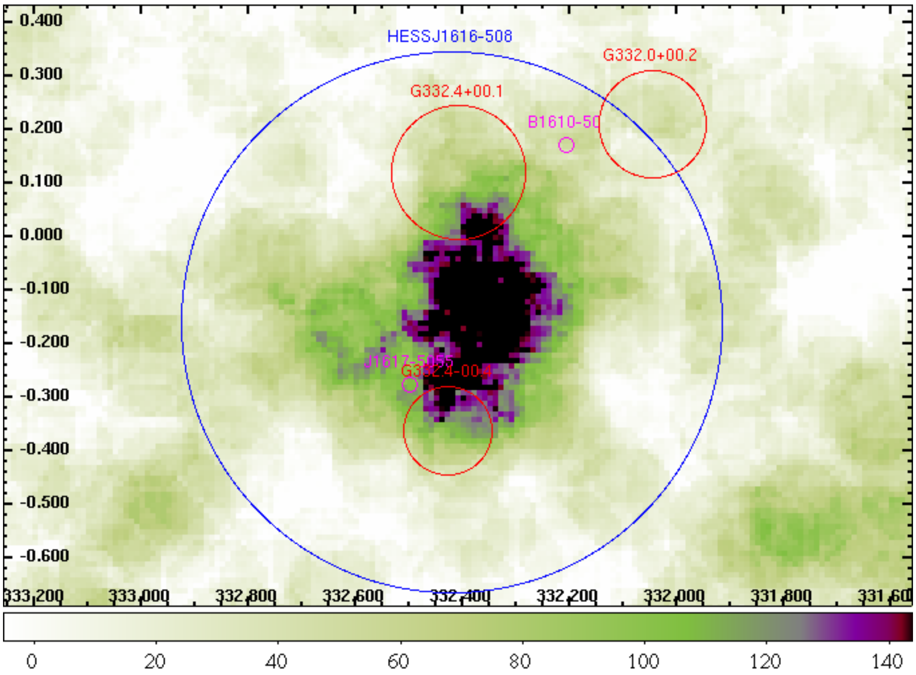

Figure 6.33: Excess map of G332.4+00.1. The SNRs G332.4+00.1 and G332.4-00.4 are nearby the γ-ray source HESS J1616-508 but are no likely counterparts for the γ-ray emission.

HESS J1634-472, SNR G337.2+00.1, Fig. 6.34

After ~12 h of observation time the significance of the γ-ray excess at the position of the SNR G337.2+00.1 amounts to 7.7σ. It is positionally coincident with the Fermi/LAT source 1FGL J1635.7-4715c (Abdo et al. 2010) and a possible counterpart to the VHE γ-ray source HESS J1634-472 as discussed by Aharonian et al. (2006d). Other discussed associations of the H.E.S.S. detection include the ASCA source AX J1635.9-4719 (Sugizaki et al. 2001b), and the INTEGRAL source IGR 16358-4726 (Tomsick et al. 2003). The nearby SNRs G337.0-00.1 and G336.7+00.5 show a significant excess, but are not associated with the γ-ray emission.

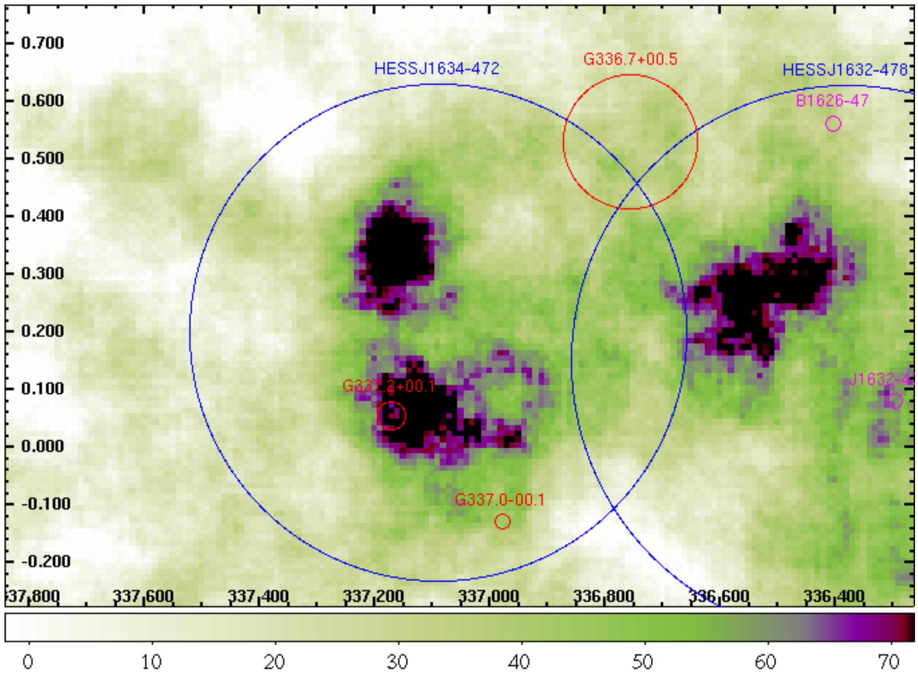

Figure 6.34: Excess map of G337.2+00.1. The SNR is a possible association of the VHE γ-ray source HESS J1634-472. The nearby SNRs G337.0-00.1 and G336.7+00.5 show a significant excess but are not associated with the γ-ray emission.

HESS J1708-443, SNR G343.1-02.3, Fig. 6.35
The γ-ray emission from HESS J1708-443 has first been investigated by Aharonian et al. (2005b), giving an upper limit on the flux. It has later on been identified with the pulsar PSR B1706-44 by Hoppe et al. (2009). The significance of the excess at the position of G343.1-02.3 is $5.9\,\sigma$ after $\sim$12 h of observation time.

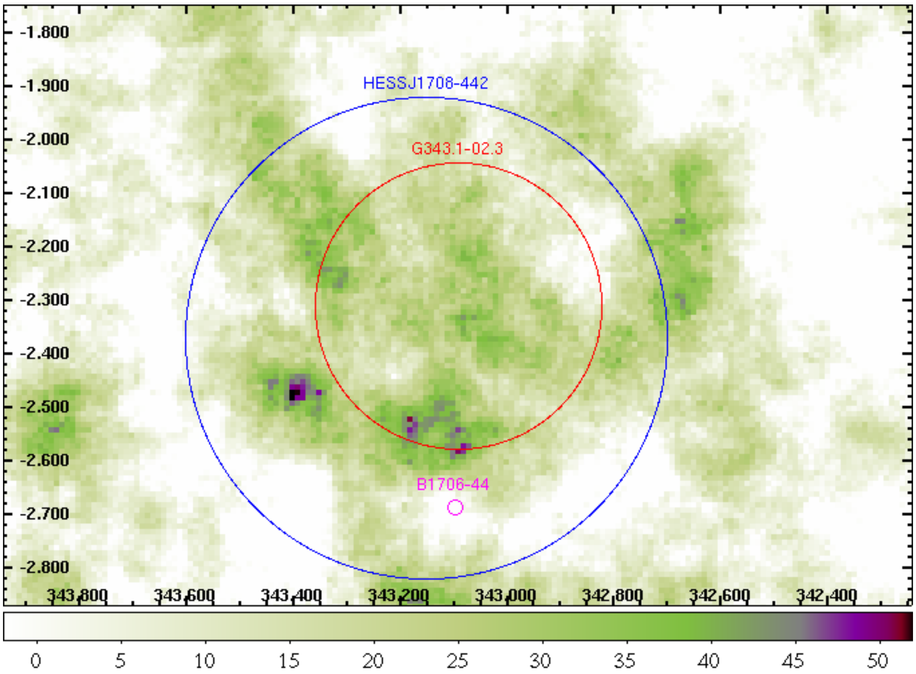

Figure 6.35: Excess map of G343.1-02.3. The γ-ray emission of HESS J1841-055 has been associated with the pulsar PSR B1706-44.

HESS J1702-420, SNR G344.7-00.1, Fig. 6.36
Possible counterparts for the γ-ray emission from HESS J1702-420, detected during the H.E.S.S. Galactic Plane Survey (Aharonian et al. 2006d), have been discussed by Aharonian et al. (2008a). The SNR G344.7-00.1, which coincides with the X-ray pulsar PSR J1702-4128 (Manchester et al. 2005) is unlikely to be the origin of the VHE γ-ray emission. A possible scenario is the displacement of the pulsar wind nebula with respect to the pulsar due to properties of the ambient medium. The significance of the excess at the position of G344.7-00.1 is 5.4σ after ~8 h of observation time.

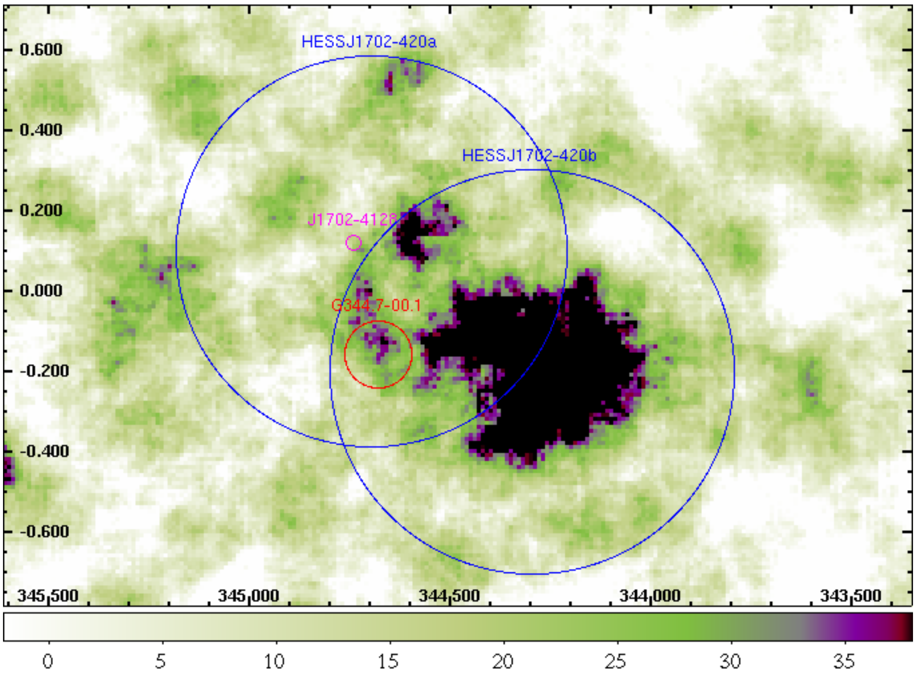

Figure 6.36: Excess map of G344.7-00.1. The image shows two exclusion regions covering the same γ-ray source HESS J1702-420. The SNR is coincident with the X-ray pulsar PSR J1702-4128 but is not likely to be the origin of the VHE γ-ray emission region.

6.2.5 SNRs far from known H.E.S.S. sources

The great number of SNRs which are nearby but not associated with known VHE γ-ray emission regions illustrates the difficulty of this study. Due to the large number of radio SNRs and the dense population of objects in the galactic plane the chances for a coincidence with other objects emitting VHE γ-rays are considerable. Furthermore it is possible that particles accelerated in SNRs illuminate distant molecular clouds and generate a VHE γ-ray signal, which is later on hard to associate with the SNR.

Therefore the investigation of SNRs being far from known H.E.S.S. sources allows to search for a VHE γ-ray emission, which is not confused by any known association of the VHE γ-ray emission. Despite significances being too low for a detection of individual SNRs it is possible that the mean of the significance distribution of these SNRs is above zero. Fig. 6.37 illustrates the distances between the SNRs' and the H.E.S.S. sources' centres and regions. The value used is an angular distance of at least 0.5° between the SNR region and the closest H.E.S.S. exclusion region. Fig. 6.38 depicts the significance distribution of these SNRs. Table 6.4 lists the SNRs together with the nearby VHE γ-ray emission regions and the respective distances between them.

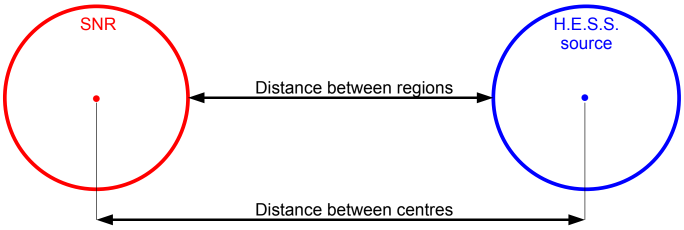

Figure 6.37: The image illustrates the distances between the SNRs' and H.E.S.S. sources' centres and regions. In Fig 6.38 the distance between the regions has been chosen to be larger than 0.5°.

The significance distribution in Fig. 6.38 can be described by a Gaussian of width $1.6\,\sigma$ centered around $0.45\,\sigma$, using an unbinned likelihood fit. It shows a slight shift towards positive significances, the effect has a significance of 2σ. Enforcing such a distance supports the observation of SNRs in regions with less hours of observation time, especially at higher galactic latitudes and longitudes, where less VHE γ-ray emitting objects are expected. This results in a lower significance for these SNR positions. Fig. 6.39 illustrates the positions of the 60 SNRs considered in Fig. 6.38.

The investigation of SNRs with large distances from H.E.S.S. exclusion regions gives a hint for a VHE γ-ray emission if considering the entire ensemble. Future work could be the comparison of this result with a simulated ensemble of SNRs. Except for 10 out of the 60 SNRs, the exposure is below 30 h. Additional observation of these radio SNRs is therefore expected to lead to further detections in VHE γ-rays.

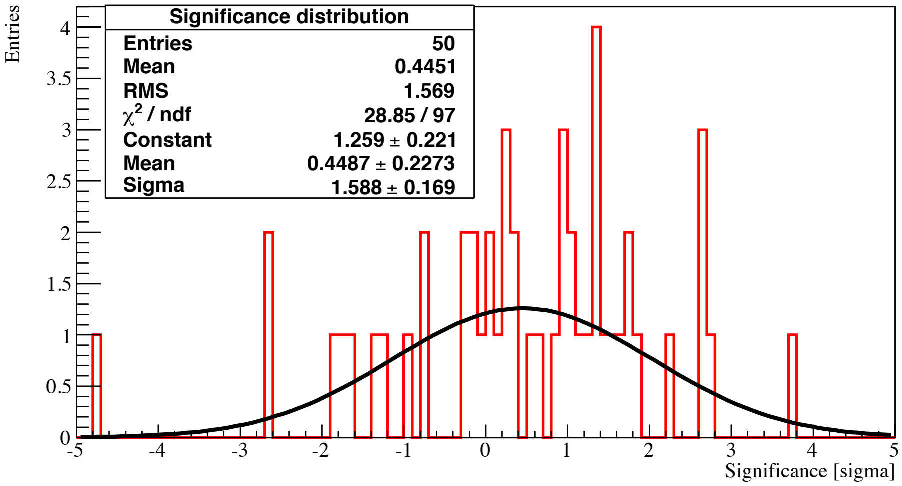

Figure 6.38: In this significance distribution only those SNRs are considered which do not overlap with known H.E.S.S. sources and have an additional gap of at least 0.5 ° between the H.E.S.S. and the SNR region. The distribution can be described by a Gaussian centered around 0.45 σ.

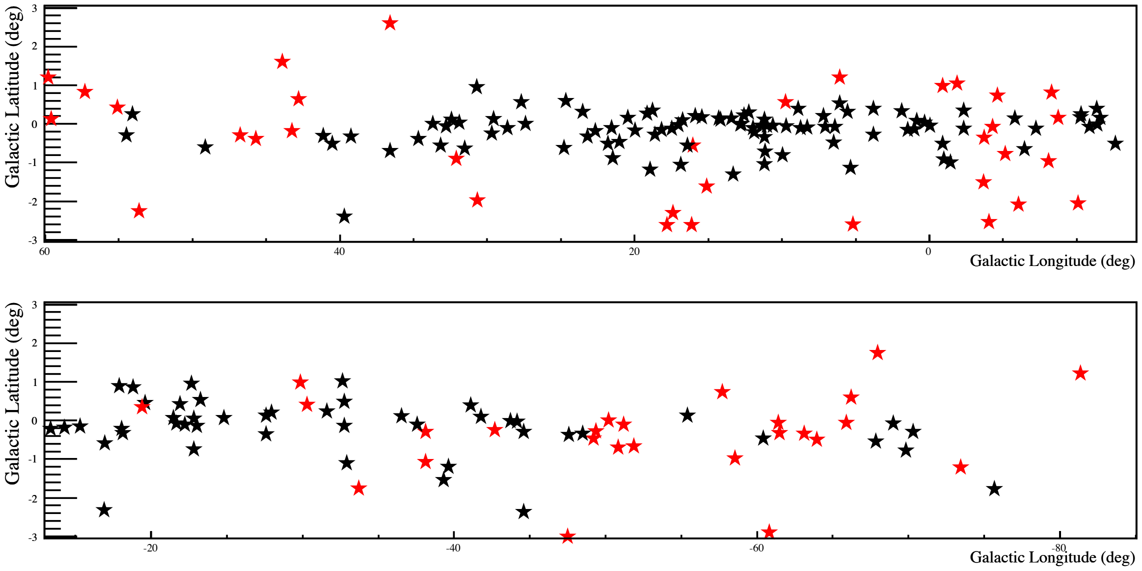

Figure 6.39: The distribution of SNRs within the H.E.S.S. survey region is illustrated by stars. Red stars indicate SNRs with a minimal distance of 0.5 ° between the SNR and the γ-ray emission region.

Table 6.4: SNRs with a distance above 0.5° to the closest known H.E.S.S. source.

SNR				H.E.S.S.				Distance betw.	
Name	Exposure [h]	Significance [σ]	Radius [deg]	Name	Gal. long. [deg]	Gal. lat. [deg]	Radius [deg]	centres [deg]	regions [deg]
G005.2-02.6	1.9	0.2	0.15	HESSJ1800-240a	6.14	-0.63	0.39	2.18	1.64
G006.1+01.2	26.2	-1.3	0.23	HOTSJ1756-240	5.44	0.48	0.25	0.99	0.5
G009.8+00.6	33.8	-0.2	0.1	HOTSJ1808-204	9.9	-0.22	0.2	0.8	0.5
G015.1-01.6	31.3	-4.7	0.23	HESSJ1818-155	15.39	-0.02	0.2	1.62	1.19
G016.0-00.5	48.0	0.3	0.11	HESSJ1818-155	15.39	-0.02	0.2	0.85	0.54
G016.2-02.7	49.7	2.8	0.14	HESSJ1826-148	16.88	-1.28	0.38	1.53	1.01
G017.4-02.3	30.2	1.5	0.2	HESSJ1826-148	16.88	-1.28	0.38	1.14	0.56
G017.8-02.6	45.2	0.3	0.2	HESSJ1826-148	16.88	-1.28	0.38	1.61	1.03
G030.7-02.0	12.9	0.9	0.13	HESSJ1848-018	30.95	-0.11	0.65	1.88	1.1
G032.1-00.9	26.5	1.1	0.33	HOTSJ1848-010	31.77	0.14	0.2	1.1	0.56
G036.6+02.6	0.4	-1.4	0.13	HESSJ1857+026	35.97	-0.06	0.7	2.72	1.9
G042.8+00.6	15.6	1.1	0.2	HESSJ1912+101	44.41	-0.1	0.46	1.76	1.1
G043.3-00.2	28.8	1.0	0.03	HESSJ1912+101	44.41	-0.1	0.46	1.15	0.66
G043.9+01.6	11.5	-1.2	0.5	HESSJ1912+101	44.41	-0.1	0.46	1.78	0.82
G045.7-00.4	24.2	2.2	0.18	HESSJ1912+101	44.41	-0.1	0.46	1.31	0.67
G046.8-00.3	16.9	0.9	0.13	HESSJ1912+101	44.41	-0.1	0.46	2.38	1.79
G053.6-02.2	3.9	-0.7	0.26	HOTSJ1930+186	54.1	0.27	0.2	2.57	2.12
G055.0+00.3	23.3	-0.2	0.15	HOTSJ1930+186	54.1	0.27	0.2	1.02	0.67
G057.2+00.8	15.7	0.8	0.1	HOTSJ1944+213	57.76	-1.28	0.2	2.16	1.86
G059.5+00.1	14.3	1.4	0.12	HOTSJ1944+213	57.76	-1.28	0.2	2.3	1.98
G059.8+01.2	6.1	1.6	0.15	HOTSJ1944+213	57.76	-1.28	0.2	3.22	2.87
G279.0+01.1	1.0	1.7	0.79	HESSJ1023ExtE	-76.41	-0.37	0.4	5.21	4.02
G286.5-01.2	27.3	2.6	0.16	HOTSJ1045-596	-72.4	-0.63	0.2	1.18	0.82
G292.0+01.8	16.8	2.6	0.08	HOTSJ1111-606	-69.0	-0.1	0.2	2.12	1.83
G293.8+00.6	14.9	0.9	0.17	HESSJ1119-614	-67.87	-0.56	0.35	2.01	1.49
G294.1-00.0	13.2	0.1	0.33	HESSJ1119-614	-67.87	-0.56	0.35	2.05	1.37
G296.1-00.5	14.6	-0.2	0.26	HESSJ1119-614	-67.87	-0.56	0.35	3.92	3.31
G296.8-00.3	18.3	0.4	0.14	HESSJ1119-614	-67.87	-0.56	0.35	4.72	4.23
G298.5-00.3	18.7	2.2	0.04	HESSJ1303-631	-55.76	-0.36	0.46	5.78	5.18
G298.6-00.0	18.0	3.8	0.09	HESSJ1303-631	-55.76	-0.36	0.46	5.62	5.07
G299.2-02.9	0.3	-1.8	0.12	HESSJ1302-638	-55.85	-0.99	0.35	5.31	4.84
G301.4-01.0	11.3	-1.0	0.26	HESSJ1302-638	-55.85	-0.99	0.35	2.69	2.08
G302.3+00.7	11.9	1.8	0.14	HESSJ1303-631	-55.76	-0.36	0.46	2.23	1.63
G308.1-00.7	16.4	0.4	0.11	HESSJ1356-645	-50.23	-2.52	0.54	2.48	1.83
G308.8-00.1	17.6	1.7	0.21	HESSJ1356-645	-50.23	-2.52	0.54	2.6	1.85
G309.2-00.6	21.8	-0.0	0.11	HESSJ1356-645	-50.23	-2.52	0.54	1.92	1.26
G309.8+00.0	19.6	1.3	0.19	HESSJ1406-613	-48.3	0.11	0.25	1.91	1.48
G310.6-00.3	19.1	1.2	0.07	HESSJ1406-613	-48.3	0.11	0.25	1.15	0.83
G310.8-00.4	18.8	-0.7	0.1	HESSJ1406-613	-48.3	0.11	0.25	1.06	0.71
G312.5-03.0	1.1	1.0	0.16	HOTSJ1414-619	-47.51	-0.57	0.25	2.43	2.02
G317.3-00.2	28.2	2.7	0.09	HOTSJ1457-594	-41.65	-0.44	0.31	1.06	0.65
G321.9-00.3	28.3	1.4	0.23	HOTSJ1511-579	-39.41	0.04	0.22	1.36	0.91
G321.9-01.1	35.6	-1.7	0.23	HESSJ1514-591	-39.67	-1.2	0.5	1.57	0.83
G326.3-01.8	18.4	0.1	0.32	HOTSJ1554-550	-32.86	-1.02	0.2	1.12	0.6
G329.7+00.4	13.6	0.0	0.31	HOTSJ1550-534	-32.25	0.56	0.4	1.98	1.27
G330.2+01.0	12.4	1.3	0.09	HESSJ1614-518	-28.5	-0.65	0.62	2.1	1.39
G340.6+00.3	29.4	1.8	0.05	HOTSJ1652-438	-18.28	0.15	0.4	1.14	0.69
G350.0-02.0	4.7	-0.3	0.38	HESSJ1718-385	-11.17	-0.46	0.3	1.93	1.25
G351.2+00.1	20.2	1.7	0.06	HOTSJ1718-375	-10.3	0.1	0.2	1.57	1.31
G351.7+00.8	16.0	-2.7	0.13	HESSJ1731-347b	-6.69	-0.12	0.42	1.86	1.31
G351.9-00.9	28.5	1.4	0.09	HESSJ1731-347b	-6.69	-0.12	0.42	1.62	1.11
G353.9-02.0	29.8	-1.6	0.11	HESSJ1731-347a	-6.44	-0.71	0.44	1.43	0.88
G354.8-00.8	37.4	1.0	0.16	HESSJ1731-347a	-6.44	-0.71	0.44	1.31	0.71
G355.4+00.7	16.5	0.6	0.21	HESSJ1731-347c	-6.26	0.5	0.44	1.67	1.03
G355.6-00.0	19.0	2.7	0.06	HESSJ1731-347c	-6.26	0.5	0.44	2.03	1.53
G355.9-02.5	1.9	0.6	0.11	HESSJ1731-347a	-6.44	-0.71	0.44	3.01	2.46
G356.3-00.3	10.5	0.9	0.08	HESSJ1745-303b	-1.21	-0.8	0.45	2.48	1.95
G356.3-01.5	5.7	-2.7	0.15	HESSJ1741-302	-1.54	0.02	0.42	2.4	1.83
G358.1+00.1	46.6	1.8	0.17	HESSJ1741-302	-1.54	0.02	0.42	1.26	0.67
G359.1+00.9	87.9	0.3	0.1	HESSJ1741-302	-1.54	0.02	0.42	1.16	0.65

6.3 Comparison of experimental and theoretical γ-ray flux values

The differential flux for all SNRs is determined including upper and lower error bars according to a confidence level of 68 % and 99 %. For all SNRs a spectral index of 2.1 is assumed, following the initial spectrum of cosmic rays. By integrating over the assumed underlying power-law spectrum the assumed integral flux above 1 TeV can be calculated. If for the given confidence level the differential flux is compatible with zero (i.e. the lower error bar is equal to or below zero), the result is an upper limit on the flux above 1 TeV, following the approach by Feldman & Cousins (1998). For 81 out of 203 analyzed SNRs, the flux is measurable at a confidence level of 99%, for the remaining 122 an upper limit on the flux can be given. Since the detection threshold of 5σ is an arbitrarily chosen value, it is possible that a flux value can be given for non-detected SNRs, i.e. with a significance of the excess of less than 5σ. Therefore the number of SNRs with flux measurements is greater than the number of detected γ-ray emission regions within the total SNR sample. For all SNRs listed in the appendix in Table A.2 with *Excess lower limit* = 0, the use of the upper limit on the flux is appropriate.

Observations with the H.E.S.S. instrument can be used to investigate the model proposed by Drury et al. (1994) and to discuss the values chosen for the total supernova explosion energy, the acceleration efficiency, and the density of the surrounding medium. The theoretical model is described in section 5.7. The flux and upper limits determined from H.E.S.S. observations are compared to the theoretically predicted values. Given that only 17 SNRs within the survey region have a known distance and the $\Sigma - D$ relation giving an estimate for the distance of shell-type SNRs, in the following only shell type SNRs are considered. This reduces the total SNR sample to 154. For these targets the expected γ-ray flux above 1 TeV has been determined using equation 5.20. The theoretically determined flux values are listed together with analysis results in the appendix in Table A.2. The error on the estimated flux, for all SNRs with calculated distance, has been derived from the RMS of the distance difference distribution shown in Fig. 6.5.

Fig. 6.40 illustrates the correlation between predicted and measured γ-ray flux and upper limits for SNRs with known (a) and calculated (b) distances. Black vertical error bars correspond to 68% errors, whereas red and green arrows indicate upper limits at a 68% (1σ) and 99% (3σ) confidence level, respectively. Horizontal error bars result from the error on the calculated distance. For some SNRs the flux value is compatible with zero at a 99% confidence level but is non-zero at a 68% confidence level. The diagonal line indicates linear correlation between the theoretical model and the experimental value.

In total 17 SNRs with known and 38 SNRs with calculated distance are shown in the plots. For 10 SNRs with known and 30 with calculated distance flux values with their errors according to a 1σ confidence level are shown in the images. In general the model describes the experimentally determined flux values and upper limits. However, large differences between experimentally and theoretically predicted flux values of up to a factor of 10 exist. These result from the choice of model parameters for the theoretical flux prediction of the acceleration efficiency $\theta = 0.1$, the total SN explosion energy $E_{SN} = 10^{51}$ erg and the assumed density of the surrounding ISM $n = 1\,\mathrm{cm}^{-3}$.

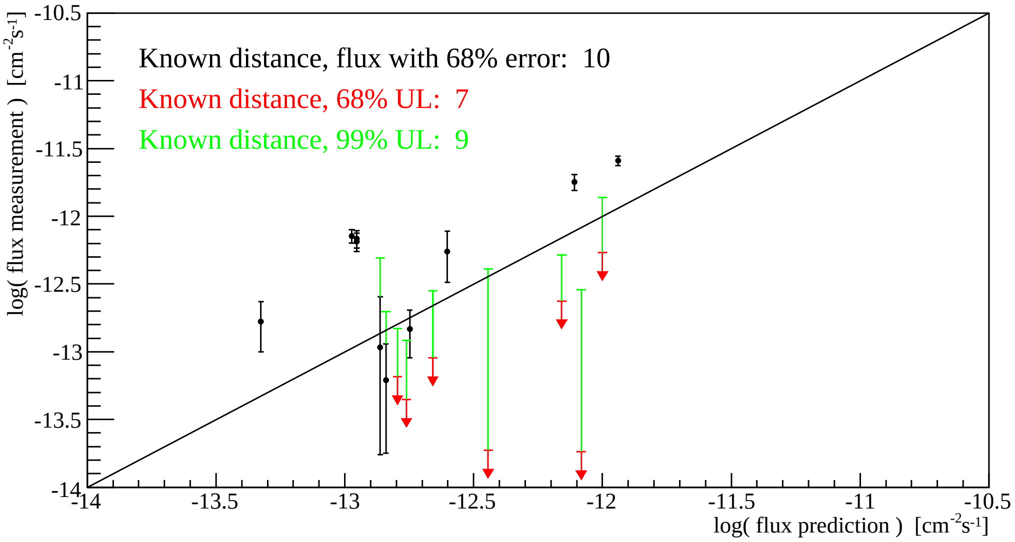

(a)

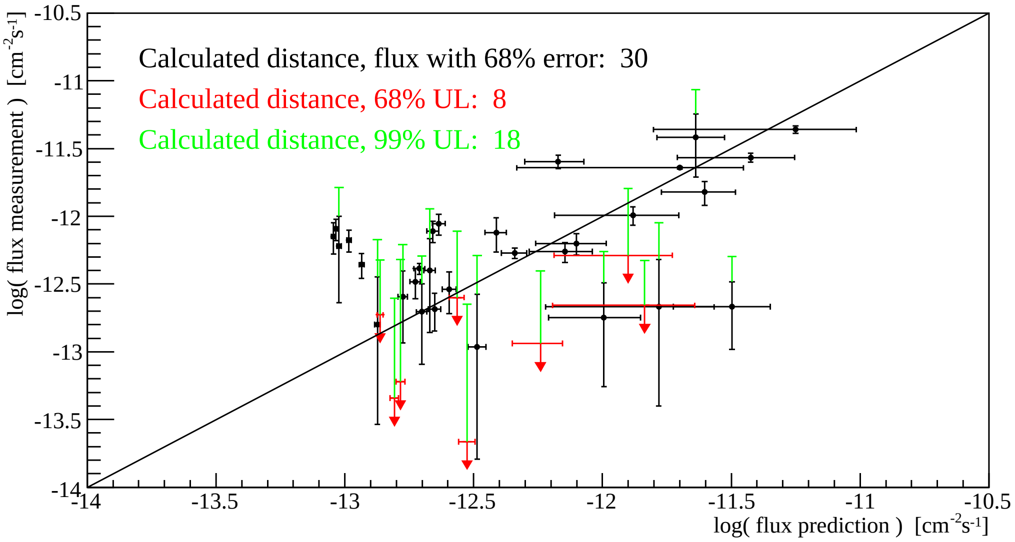

(b)

Figure 6.40: The figures illustrate the differences between theoretically predicted and measured VHE γ-ray flux for shell-type SNRs with (a) known and (b) calculated distances above an energy threshold of 1 TeV. Black vertical error bars correspond to 68% errors, whereas red and green arrows show upper limits at a 68% (1σ) and 99% (3σ) confidence level, respectively. Horizontal error bars in (b) result from the error on the calculated distance. The error on the predicted flux from SNRs with known distance (a) is not considered here. The diagonal line indicates linear correlation between the theoretical prediction and the experimental value. For the theoretical flux prediction, an acceleration efficiency of $\theta = 0.1$, a total SN explosion energy of $E_{SN} = 10^{51}$ erg and an ambient ISM density of $n = 1\,\mathrm{cm}^{-3}$ has been assumed.

For SNRs of type Ia the total energy of the supernova explosion is widely agreed to be $\sim 10^{51}$erg. Since the type of supernova is not known for the considered SNRs the total explosion energy could differ from the used value by a factor of 5-10. For the efficiency of cosmic ray acceleration, values ranging from 0.05 to 0.5 have been discussed by Drury et al. (1994). The choice of the value therefore introduces an uncertainty on the resulting flux. Furthermore the model proposed by Drury et al. (1994) predicts the hadronic component of VHE γ-rays only. On the other hand, flux measurements from H.E.S.S. observations include VHE γ-radiation from both, hadronic and leptonic CR interactions. Therefore the model can only predict part of the measured flux. An additional uncertainty arises from the density of the interstellar medium in which the SNR evolves. The density has been set to $1\,\mathrm{cm}^{-3}$ for all considered SNRs but in reality can be lower than this value, leading to a lower VHE γ-ray production from π^0-decay. Finally an error is introduced by the distance determination. The correction of the bias resulting from the $\Sigma - D$ relation follows a simple fit and is therefore rather rudimentary. In total the error on the predicted flux is quite considerable for individual SNRs and can reach up to an order of magnitude.

For some SNRs the theoretical model overestimates the experimentally determined upper limits. Fig. 6.41 shows a zoom into Fig. 6.40 giving the names of all SNRs for which the theoretical flux prediction is above the experimental results. This can result from a negative number of excess events, as for G053.6-02.2 and G054.4-00.3 in Fig. 6.41(a). The low exposure of these SNRs is not reflected in the flux prediction, which is in these cases not comparable to the experimental results. Other SNRs do not suffer from very low exposure, like G304.6+00.1 in Fig. 6.41(a), which indicates an inappropriate choice of model parameters E_{SN}, θ and n. Tables 6.5 and 6.6 list SNRs for which the flux values or the 1σ upper limits are below the theoretical value. The tables give the significance, the VHE γ-ray excess, the exposure, the mean zenith angle during the observation, the experimental and theoretical flux values, and upper limit at the 1σ and 3σ confidence level on the product of the model parameters $\theta \cdot E_{SN} \cdot n$ for these SNRs with known and calculated distances, respectively.

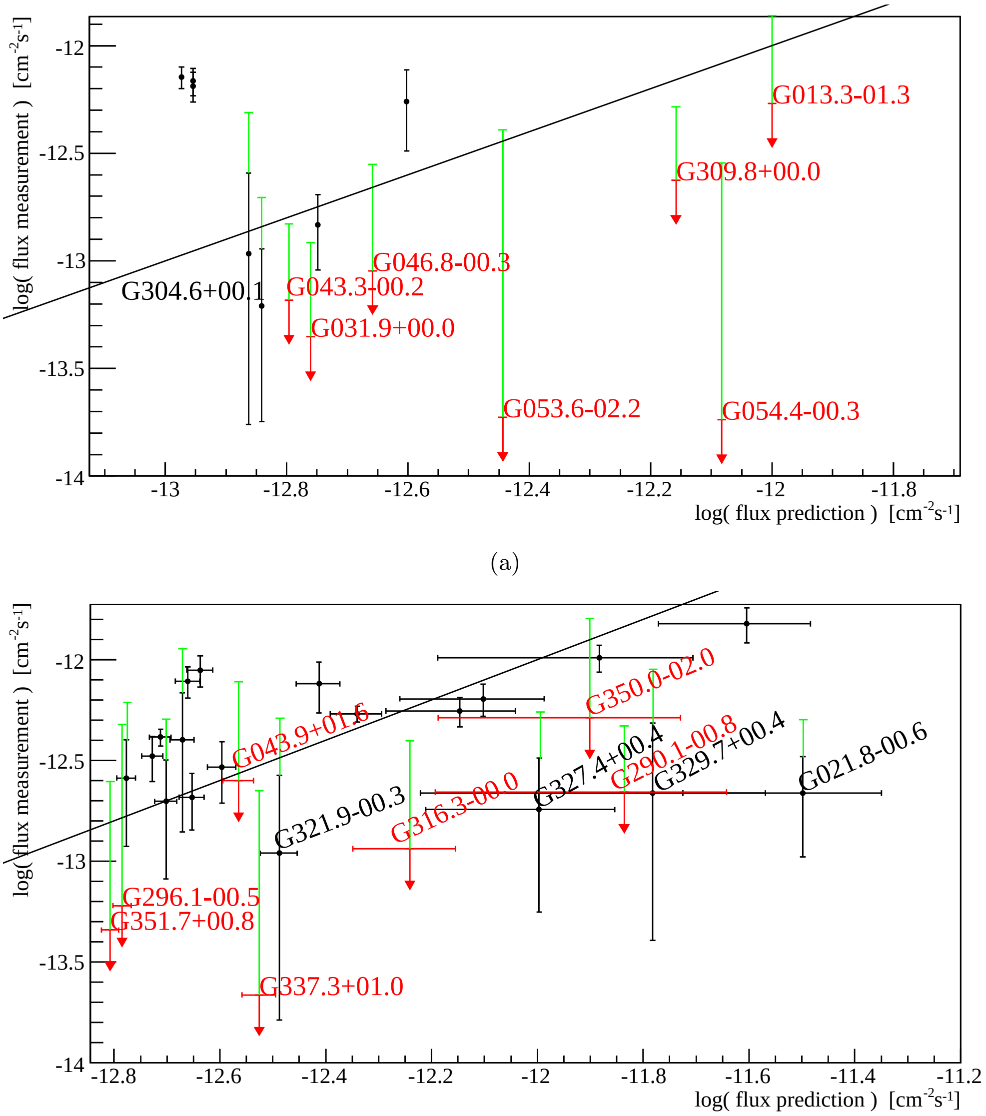

(a)

(b)

Figure 6.41: The figures represent a zoom into Fig. 6.40 indicating the names of the SNRs, for which the model overestimates the 1σ flux values and upper limits. Black data points represent experimentally determined flux values, whereas red and green data points show the 1σ and 3σ upper limits, respectively. Horizontal error bars in (b) result from the error on the calculated distance. The diagonal line indicates linear correlation between the theoretical prediction and the experimental value.

Table 6.5: SNRs with known distances and theoretical predictions above experimental flux values.

SNR	Significance [σ]	Excess [counts]	Exposure [h]	Mean zenith angle [deg]	int. Flux (>1TeV) $\log_{10}$ [$\mathrm{cm}^{-2}\mathrm{s}^{-1}$]	Upper limit $\log_{10}$ [$\mathrm{cm}^{-2}\mathrm{s}^{-1}$]		Theoret. flux pred. $\log_{10}$ [$\mathrm{cm}^{-2}\mathrm{s}^{-1}$]	$\theta E_{SN} n$ [10^{51}erg cm^{-3}]	
						(68%)	(99%)		(99%)	(68%)
G013.3-01.3	-1.3	-53.1	6.3	17.05	-14.08	-12.27	-11.86	-12.0	0.14	0.05
G031.9+00.0	0.0	0.0	42.2	29.21	–	-13.35	-12.92	-12.76	0.07	0.03
G043.3-00.2	1.0	12.8	28.8	38.09	-13.88	-13.18	-12.83	-12.8	0.09	0.04
G046.8-00.3	0.9	17.3	16.9	38.9	–	-13.05	-12.55	-12.66	0.13	0.04
G053.6-02.2	-0.7	-9.0	3.9	46.66	–	-13.73	-12.39	-12.44	0.11	0.01
G054.4-00.3	-0.5	-16.9	19.8	46.96	–	-13.74	-12.54	-12.08	0.03	0.002
G304.6+00.1	4.4	133.6	79.6	42.89	-13.21	-12.94	-12.71	-12.84	0.14	0.08
G309.8+00.0	1.3	30.8	19.6	41.81	-13.23	-12.63	-12.28	-12.16	0.07	0.03

Table 6.6: SNRs with calculated distances and theoretical predictions above experimental flux values.

SNR	Significance [σ]	Excess [counts]	Exposure [h]	Mean zenith angle [deg]	int. Flux (>1TeV) $\log_{10}$ [$\mathrm{cm}^{-2}\mathrm{s}^{-1}$]	Upper limit $\log_{10}$ [$\mathrm{cm}^{-2}\mathrm{s}^{-1}$]		Theoret. flux pred. $\log_{10}$ [$\mathrm{cm}^{-2}\mathrm{s}^{-1}$]	$\theta E_{SN} n$ [10^{51}erg cm^{-3}]	
						(68%)	(99%)		(99%)	(68%)
G006.5-00.4	4.8	194.0	32.7	18.4	-12.2	-12.13	-12.03	-12.1	0.19	0.15
G008.7-00.1	17.8	1051.1	23.1	22.57	-11.36	-11.33	-11.29	-11.25	0.31	0.29
G009.9-00.8	-0.1	-3.8	36.7	19.99	–	-13.54	-12.87	-13.17	0.1	0.02
G011.1-01.0	-0.5	-13.5	27.0	20.31	–	-13.82	-12.86	-13.21	0.11	0.01
G015.1-01.6	-4.7	-198.3	31.3	20.2	–	-14.49	-13.13	-13.09	0.05	0.002
G017.8-02.6	0.3	13.4	45.2	22.09	–	-13.81	-12.84	-13.35	0.13	0.01
G021.8-00.6	2.0	69.9	28.2	21.47	-12.67	-12.49	-12.3	-11.5	0.05	0.03
G022.7-00.2	6.1	237.1	24.5	22.57	-11.99	-11.93	-11.85	-11.88	0.22	0.18
G023.3-00.3	15.6	588.6	18.9	22.46	-11.57	-11.53	-11.49	-11.42	0.26	0.24
G043.9+01.6	-1.2	-49.7	11.5	38.71	–	-12.6	-12.11	-12.56	0.28	0.09
G290.1-00.8	0.7	12.0	16.5	40.23	-13.2	-12.66	-12.33	-11.84	0.07	0.03
G296.1-00.5	-0.2	-3.5	14.6	43.36	–	-13.22	-12.32	-12.78	0.23	0.03
G310.8-00.4	-0.7	-11.4	18.8	41.76	–	-13.57	-12.72	-13.25	0.16	0.02
G312.4-00.4	4.9	184.2	18.7	42.82	-11.82	-11.74	-11.64	-11.6	0.24	0.19
G316.3-00.0	1.0	27.0	19.4	38.69	–	-12.94	-12.4	-12.24	0.1	0.03
G321.9-00.3	1.4	56.8	28.3	36.97	-12.96	-12.58	-12.29	-12.49	0.17	0.09
G321.9-01.1	-1.7	-81.0	35.6	37.29	–	-14.26	-12.93	-13.43	0.12	0.01
G327.4+00.4	1.6	42.4	24.1	33.61	-12.75	-12.49	-12.26	-11.99	0.1	0.06
G329.7+00.4	0.0	0.3	13.6	32.9	-12.67	-12.32	-12.05	-11.78	0.12	0.06
G337.3+01.0	-0.9	-15.1	9.4	27.35	–	-13.66	-12.65	-12.53	0.08	0.01
G350.0-02.0	-0.3	-7.2	4.7	17.59	–	-12.29	-11.79	-11.9	0.25	0.08
G351.7+00.8	-2.7	-59.7	16.0	17.96	–	-13.34	-12.6	-12.81	0.12	0.02
G359.0-00.9	6.6	423.7	70.6	21.38	-12.26	-12.19	-12.1	-12.15	0.17	0.14

The tables show negative significances for 13 SNRs, resulting from statistical fluctuations of the background. Small numbers of excess events can result from low exposures, like for G013.3-01.3 and G053.6-02.2 (Table 6.5) and for G337.3+01.0 and G350.0-02.0 (Table 6.6). For all listed SNRs the mean zenith angle of the observation is in a range between ∼17° and ∼45° and shows no effect on the significance of the VHE γ-ray excess.

Given that the theoretical model should rather underestimate the measured γ-ray flux (due to the missing VHE γ-ray component from inverse Compton scattering) the SNRs with an overestimation of the theoretical value can be used to derive a constraint on the parameters. This constraint is however only accessible for the product of the parameters. Therefore the product of total supernova explosion energy, acceleration efficiency and surrounding density, $\theta E_{SN} n$, has been calculated according to equation 5.20. Tables 6.5 and 6.6 list the value derived from upper limits on the flux with confidence levels of 1σ and 3σ. The value is given in 10^{51}erg cm^{-3}.

The value $\theta E_{SN} n$ used for the calculation of the theoretical model is $0.1 \cdot 10^{51}$erg cm^{-3}. This value is compared to the results given in the last two columns of Tables 6.5 and 6.6. Considering only SNRs with positive significances (4 with known and 12 with calculated distance) the comparison shows large differences in the results. The experimentally derived value for $\theta E_{SN} n$ ranges between 0.03 and $0.29 \cdot 10^{51}$erg cm^{-3}. A smaller value for $\theta E_{SN} n$

can result from either a lower acceleration efficiency, a lower total explosion energy, a lower density of the surrounding medium, or a combination of all. To further constrain the parameters it is necessary to investigate more in detail the individual SNRs. Additional observations of these SNRs in the VHE γ-ray range as well as in other wavebands are needed.

6.3.1 Comparison to HEGRA observations

In this section the results from current H.E.S.S. observations of SNRs are compared to former VHE observations using the HEGRA detector (Fonseca 1998). With this instrument a search for VHE γ-ray emission has been conducted in the Galactic plane in the longitude range between -2 ° and 85 ° (Aharonian et al. 2002), resulting in an upper limit on the γ-ray flux for 63 SNRs. For 19 SNRs with longitudes $l < 20°$ and distances $d <10\,\mathrm{kpc}$ the statistics was accumulated and an upper limit on the flux of the ensemble of 6.7 % of the flux of the Crab nebula has been derived, which is about a factor of two above the theoretical flux of the ensemble of 2.9 % of the Crab flux. The theoretical ensemble flux $F_{Ensemble}$ is defined as

$$\frac{F_{Ensemble}}{F_{Crab}} = \sum_i \frac{F_\gamma^i}{F_{Crab}} \frac{T^i}{T} = \frac{F_{SNR}}{F_{Crab}} \frac{1\ \mathrm{kpc}^2}{T} \sum_i \frac{T^i}{{d_i}^2} \tag{6.6}$$

where F_{SNR} is the predicted flux from a source at a distance of 1 kpc according to equation (5.20), T is the sum of the total observation time, and T^i/d_i^2 is the exposure and distance weight of the ith SNR. The flux of the Crab nebula above 1 TeV is $F_{Crab} = 2.2 \cdot 10^{-11}\,\mathrm{cm}^{-2}\mathrm{s}^{-1}$ (Aharonian et al. 2006a).

The HEGRA results are compared with the ensemble limit and flux prediction based on current H.E.S.S. observations of the same ensemble. Table 6.7 lists the analysis results for the 19 SNRs observed with HEGRA and H.E.S.S. (columns marked with 1 and 2, respectively). The individual upper limits derived from H.E.S.S. observations are all below the HEGRA limits by up to an order of magnitude, resulting from longer exposure and the increased sensitivity of the H.E.S.S. detector. The last row gives the ensemble limits. The theoretical value is derived from equation (6.6). The observationally determined ensemble upper limit is a stacked upper limit based on analysis results from the individual SNRs. In the case of HEGRA the limits are taken from Aharonian et al. (2002), using $F_{SNR} = 1.44{\cdot}10^{-11}\,\mathrm{cm}^{-2}\mathrm{s}^{-1}$ for the theoretical flux prediction with equation (5.20). For the H.E.S.S. limits four SNRs are excluded from the ensemble: G021.5-00.9, G024.7-00.6, and G040.5-00.5 are associated with pulsar wind nebulae and G073.9+00.9 is not included in the H.E.S.S. GPS region. The upper limit derived from H.E.S.S. observations is about 1.8 % of the Crab flux. During this thesis a value of $F_{SNR} = 0.9{\cdot}10^{-11}\,\mathrm{cm}^{-2}\mathrm{s}^{-1}$ has been used, assuming the acceleration efficiency to be $\theta = 0.1$ rather than $\theta = 0.16$ as applied by Aharonian et al. (2002). Therefore, equation (6.6) yields a theoretically predicted flux value for the ensemble of 8.7 % of the Crab flux, which is about a factor of 5 above the observational upper limit.

The direct comparison of the H.E.S.S. and HEGRA results is difficult due to the different ensemble size and due to differing distances considered for the theoretical model, since the bias of the $\Sigma - D$ relation has not been taken into account for the results obtained with

HEGRA data. Furthermore the ensemble upper limit is dominated by two SNRs with a significant flux: G022.7-00.2 and G023.3-00.3 with flux values of 6 % and 15 % of the Crab flux, respectively. The value for the theoretical flux of the ensemble is strongly influenced by the correction of the distance calculation described in section 6.1.2. The correction based on Fig. 6.5 reduces all distances below 6 kpc. The dominant contribution comes from the SNR G034.7-00.4 with a calculated distance of 3.3 kpc and a corrected distance of 0.8 kpc. Together with the increased observation time of 40.5 h (compared to 3.7 h with HEGRA) the weight factor is ∼64, which has a strong effect on the predicted ensemble flux.

Table 6.7: Comparison of analysis results from SNRs observed with HEGRA and H.E.S.S. (columns marked with 1 and 2, respectively). The type indicates the morphology according to Green's catalog (C = Composite, S = shell type, ? denotes some uncertainties). The upper limit on the integral flux is calculated above 1 TeV for H.E.S.S. and above the given energy threshold for HEGRA. Flux values are given in units [CU] of the Crab nebula's integral flux above 1 TeV of $F_{crab} = 2.2 \cdot 10^{-11}\text{cm}^{-2}\text{s}^{-1}$. The last column gives the expected γ-ray flux from hadronic interactions according to Drury et al. (1994). SNRs with known non-SNR counterpart are excluded. The last row indicates the ensemble limit, summing over all remnants and deriving a significance and upper limit for the entire sample. The weight for each SNR is given by $Exposure/distance^2$. The ensemble values determined with HEGRA observations include all 19 SNR, whereas limits from H.E.S.S. observations exclude the SNR G073.9+00.9, which is not in the field of view of the H.E.S.S. GPS, as well as the SNRs G021.5-00.9, G024.7-00.6, and G040.5-00.5, whose γ-ray emission is associated with pulsar wind nebulae.

SNR	Type	Rad.	Distance		Exposure		Significance		Weight Exposure/Distance^2		Energy thresh.	Upper limit 99% CL		Theoret. flux pred.
			1	2	1	2	1	2	1	2	1	1	2	2
		[deg]	[kpc]		[h]		[σ]		[h/kpc^2]		[TeV]	[CU]		[CU]
(G021.5-00.9)	C	0.03	6.3	(–)	1.6	(27.1)	1.7	(6.4)	0.04	(–)	1.5	0.7	(0.03)	(–)
G021.8-00.6	S	0.17	2.9	1.7	2.6	28.2	0.9	2.0	0.31	3.48	1.5	0.39	0.02	0.145
G022.7-00.2	S?	0.22	3.7	2.6	1.2	24.5	1.5	6.1	0.09	1.77	1.4	0.89	0.06	0.06
G023.3-00.3	S	0.22	2.7	1.5	1.2	18.9	0.6	15.6	0.17	2.6	1.4	0.69	0.15	0.171
(G024.7-00.6)	S?	0.12	7.4	(9.3)	3.3	(23.7)	-0.9	(7.7)	0.06	(0.447)	1.3	0.23	(0.04)	(0.005)
G030.7+01.0	S?	0.18	7.9	10.6	2.1	29.1	-0.8	-0.3	0.03	0.47	1.0	0.3	0.01	0.004
G031.9+00.0	S	0.05	7.2	7.2	4.2	42.2	0.5	0.0	0.08	1.46	1.0	0.16	0.01	0.008
G032.8-00.1	S?	0.14	6.3	6.9	3.1	42.0	1.2	4.7	0.08	1.05	1.0	0.32	0.02	0.009
G033.6+00.1	S	0.08	7.1	7.1	5.8	51.4	0.3	2.7	0.12	1.94	0.9	0.14	0.01	0.008
G034.7-00.4	C	0.26	3.3	0.8	3.7	40.5	-0.9	4.5	0.34	15.83	0.9	0.19	0.04	0.65
G039.2-00.3	C	0.06	5.9	6.1	3.1	31.5	-0.1	0.5	0.09	0.9	0.8	0.18	0.01	0.011
(G040.5-00.5)	S	0.18	6.1	(6.4)	2.1	(28.5)	1.7	(8.0)	0.06	(0.8)	0.8	0.43	(0.05)	(0.01)
G041.1-00.3	S	0.03	6.1	6.4	3.2	27.2	0.8	3.0	0.09	0.75	0.8	0.18	0.02	0.01
G043.3-00.2	S	0.03	7.5	7.5	3.4	28.8	-0.1	1.0	0.06	1.24	0.7	0.14	0.01	0.007
G045.7-00.4	S	0.18	9.1	14.0	2.6	24.2	-0.5	2.2	0.03	0.29	0.7	0.2	0.02	0.002
G046.8-00.3	S	0.13	6.4	6.4	2.6	16.9	0.4	0.9	0.06	0.5	0.7	0.22	0.01	0.01
G049.2-00.7	S?	0.25	6.0	6.0	3.0	15.6	0.6	2.3	0.08	4.44	0.6	0.27	0.05	0.011
G054.4-00.3	S	0.33	3.3	2.6	1.5	19.8	-0.5	-0.5	0.14	1.42	0.6	0.38	0.01	0.038
(G073.9+00.9)	S?	0.18	6.6	(–)	2.0	(–)	-0.2	(–)	0.05	(–)	0.6	0.18	(–)	(–)
$\Sigma_{1-19\ (15)}$			$< 5.2 >$	$< 5.83 >$	52.3	440.8	1.1	11.45	1.962	93.94		0.067	0.0188	0.087

Beyond the comparison with HEGRA results it is possible to determine upper limits of the entire currently available SNR ensemble, excluding SNRs whose VHE γ-ray flux is associated to non-SNR counterparts. Table 6.9 lists the results for the 99 SNRs, which fulfill this condition and for which a theoretical flux value can be calculated.

With longer exposure and the increased sensitivity of the H.E.S.S. detector 16 out of the 99 SNRs show a significance of the γ-ray excess above $5\,\sigma$. While the upper limits determined with HEGRA were up to an order of magnitude larger , recent observations with H.E.S.S. result in upper limits of the same order of magnitude than the theoretically predicted values. The theoretical ensemble flux according to equation (6.6) is 3.8 % of the Crab flux. The upper limit derived from the observations is 1.4 % of the Crab flux, which is about a factor of 2.7 below the theoretical value. Again, the theoretical value is dominated by SNRs with a strong weight due to their small calculated distance and long exposure, resulting in a total weight of ~236 for the entire sample of 99 SNRs, calculated as the sum of all individual SNR weights. As before the choice of the density of the surrounding medium n, of the total supernova explosion energy $\mathrm{E_{SN}}$, and the acceleration efficiency θ influence the resulting flux value.

Based on the ensemble of 99 SNRs Table 6.10 lists the results for those 61 SNRs, which do not have a measurable VHE γ-ray flux but only upper limits on the flux. Assuming $\theta E_{SN} n = 0.1\,\mathrm{erg\,cm^3}$ the VHE γ-ray flux is theoretically predicted and listed in the second last column and the upper limit derived from observations is given in the third last column. The resulting ensemble upper limit is expected to decrease compared to the sample including significant SNRs, since the dominating flux values are not considered any more. The resulting theoretical flux value of the ensemble is a factor of ~40 larger than the experimental upper limit. This results mainly from those SNRs with a small calculated distance whose weight is more important. Although the result depends strongly on the chosen ensemble and the estimated distance, it illustrates the influence of the choice of parameters used for the theoretical model, hidden in the product $\theta E_{SN} n d^{-2}$. Assuming the distance to be a correct estimate, the upper limits for $\theta E_{SN} n$ for the individual SNRs are given in the last column. The value derived from the measured flux is between $0.01\,\mathrm{erg\,cm^{-3}}$ and $1.92\,\mathrm{erg\,cm^{-3}}$. The individual parameters' influence cannot be unfolded from the product and thus differences in $\theta E_{SN} n$ can result from either the acceleration efficiency, the supernova explosion energy or density of the surrounding medium. The large sample of 61 SNRs with only about 10 SNRs showing a product $\theta E_{SN} n$ close to $0.01\,\mathrm{erg\,cm^{-3}}$ suggests a further investigation of the model parameters. Another aspect, that has not been considered here is the age of the SNRs. As pointed out by Ptuskin & Zirakashvili (2005), SNRs are generally not bright in VHE γ-rays at an age above a few thousand years. The age of most SNRs of the investigated sample is unknown. It is therefore likely that the theoretical VHE γ-ray flux prediction is not the since it does not take into account the SNRs age.

Table 6.8 summarizes all results from the ensemble studies of upper limits and theoretical flux predictions.

Sample	HEGRA		H.E.S.S.	
	Upper limit	Theory	Upper limit	Theory
$d < 10$, $l > 20$ 19 (18) SNRs	0.067	0.029	0.0188	0.087
All SNRs within GPS without SNRs obtaining VHE γ-ray flux from confused non-SNR H.E.S.S. counterparts and with flux prediction (99 SNRs)	–	–	0.0144	0.0378
Like above additionally only SNRs without measurable VHE γ-ray flux (61 SNRs)	–	–	0.00057	0.0251

Table 6.8: Summary of upper limits and theoretical flux values for different ensembles.

Table 6.9: Analysis results for SNRs observed with H.E.S.S.. Snrs, whose VHE γ-ray flux results from a known emission region which has a non-SNR associations are excluded. Only SNRs for which a theoretical flux prediction is available are considered. The type indicates the morphology according to Green's catalog (C = Composite, S = shell type, ? denotes some uncertainties). The upper limit on the integral flux is calculated above 1 TeV. Flux values are given in units [CU] of the Crab nebula's integral flux above 1 TeV of $F_{crab} = 2.2 \cdot 10^{-11}\mathrm{cm}^{-2}\mathrm{s}^{-1}$. The last column gives the expected γ-ray flux from hadronic interactions according to Drury et al. (1994). The last row indicates the ensemble limit, summing over all remnants and deriving a significance and upper limit for the entire sample. The weight for each SNR is given by $Exposure/distance^2$.

SNR	Type	Radius [deg]	Distance [kpc]	Exposure [h]	Significance [σ]	Weight Exposure/ Distance^2 [h/kpc^2]	Upper limit 99% CL [CU]	Theoret. flux pred. [CU]
G001.0-00.1	S	0.07	6.79	128.2	11.5	2.78	0.023	0.0090
G005.4-01.2	C?	0.29	2.31	22.7	2.5	4.24	0.041	0.076
G005.5+00.3	S	0.11	13.06	35.8	3.8	0.21	0.023	0.0020
G006.1+00.5	S	0.13	14.85	20.0	1.7	0.09	0.019	0.0020
G006.1+01.2	F	0.23	13.53	26.2	-1.3	0.14	0.011	0.0020
G006.4-00.1	C	0.4	0.67	19.8	5.5	44.68	0.124	0.923
G006.5-00.4	S	0.15	3.37	32.7	4.8	2.88	0.042	0.036
G008.9+00.4	S	0.2	7.32	25.3	1.4	0.47	0.028	0.0080
G009.9-00.8	S	0.1	11.54	36.7	-0.1	0.28	0.0060	0.0030
G011.1-01.0	S	0.13	12.05	27.0	-0.5	0.19	0.0060	0.0030
G011.2-00.3	C	0.03	6.17	38.4	5.5	1.01	0.017	0.011
G011.4-00.1	S?	0.07	14.35	36.8	4.5	0.18	0.019	0.0020
G013.3-01.3	S?	0.48	3.0	6.3	-1.3	0.7	0.063	0.045
G015.1-01.6	S	0.23	10.52	31.3	-4.7	0.28	0.0030	0.0040
G015.4+00.1	S	0.12	12.61	28.1	1.6	0.18	0.026	0.0030
G016.4-00.5	S	0.11	15.35	35.8	1.9	0.15	0.018	0.0020
G017.4-02.3	S	0.2	12.23	30.2	1.5	0.2	0.016	0.0030
G017.8-02.6	S	0.2	14.21	45.2	0.3	0.22	0.0070	0.0020
G018.8+00.3	S	0.12	8.1	12.4	1.3	0.19	0.022	0.0060
G018.9-01.1	C?	0.28	2.26	30.8	-0.6	6.03	0.022	0.08
G019.1+00.2	S	0.22	6.49	7.2	0.9	0.17	0.052	0.01
G020.0-00.2	F	0.08	8.8	14.3	2.0	0.18	0.018	0.0050
G021.8-00.6	S	0.17	1.68	28.2	2.0	9.98	0.023	0.145
G022.7-00.2	S?	0.22	2.62	24.5	6.1	3.57	0.065	0.06
G023.3-00.3	S	0.22	1.55	18.9	15.6	7.9	0.148	0.171
G023.6+00.3	?	0.08	10.56	20.3	1.5	0.18	0.019	0.0040
G024.7+00.6	C?	0.2	3.91	14.9	3.3	0.97	0.046	0.027
G027.8+00.6	F	0.34	2.47	19.3	2.8	3.16	0.071	0.067
G030.7+01.0	S?	0.18	10.58	29.1	-0.3	0.26	0.012	0.0040
G031.9+00.0	S	0.05	7.2	42.2	0.0	0.81	0.0060	0.0080
G032.8-00.1	S?	0.14	6.92	42.0	4.7	0.88	0.025	0.0090
G033.6+00.1	S	0.08	7.1	51.4	2.7	1.02	0.013	0.0080
G034.7-00.4	C	0.26	0.79	40.5	4.5	64.35	0.038	0.65
G039.2-00.3	C	0.06	6.09	31.5	0.5	0.85	0.011	0.011
G039.7-02.0	?	0.79	1.04	11.1	0.6	10.2	0.053	0.376
G041.1-00.3	S	0.03	6.35	27.2	3.0	0.67	0.017	0.01
G043.3-00.2	S	0.03	7.5	28.8	1.0	0.51	0.0070	0.0070
G043.9+01.6	S?	0.5	5.75	11.5	-1.2	0.35	0.035	0.012
G045.7-00.4	S	0.18	14.03	24.2	2.2	0.12	0.024	0.0020
G046.8-00.3	S	0.13	6.4	16.9	0.9	0.41	0.013	0.01
G049.2-00.7	S?	0.25	6.0	15.6	2.3	0.43	0.051	0.011
G053.6-02.2	S	0.26	5.0	3.9	-0.7	0.16	0.019	0.016
G054.4-00.3	S	0.33	2.62	19.8	-0.5	2.89	0.013	0.038
G279.0+01.1	S	0.79	1.98	1.0	1.7	0.26	0.392	0.105
G284.3-01.8	S	0.2	6.23	29.3	6.2	0.75	0.058	0.011
G289.7-00.3	S	0.13	11.22	16.3	0.3	0.13	0.022	0.0030
G290.1-00.8	S	0.14	2.48	16.5	0.7	2.67	0.021	0.066
G291.0-00.1	C	0.12	5.44	26.5	2.7	0.9	0.021	0.014
G292.0+01.8	C	0.08	6.31	16.8	2.6	0.42	0.02	0.01
G293.8+00.6	C	0.17	12.52	14.9	0.9	0.1	0.036	0.0030
G296.1-00.5	S	0.26	7.4	14.6	-0.2	0.27	0.022	0.0070

Continued on next page

Table 6.9 – continued from previous page

SNR	Type	Radius [deg]	Distance [kpc]	Exposure [h]	Significance [σ]	Weight Exposure/ Distance^2 [h/kpc^2]	Upper limit 99% CL [CU]	Theoret. flux pred. [CU]
G296.8-00.3	S	0.14	8.1	18.3	0.4	0.28	0.022	0.0060
G298.6-00.0	S	0.09	15.27	18.0	3.8	0.08	0.025	0.0020
G302.3+00.7	S	0.14	13.17	11.9	1.8	0.07	0.026	0.0020
G304.6+00.1	S	0.07	7.9	79.6	4.4	1.28	0.0090	0.0070
G308.8-00.1	C?	0.21	4.79	17.6	1.7	0.77	0.042	0.018
G309.2-00.6	S	0.11	10.71	21.8	-0.0	0.19	0.02	0.0040
G309.8+00.0	S	0.19	3.6	19.6	1.3	1.51	0.024	0.032
G310.6-00.3	S	0.07	16.69	19.1	1.2	0.07	0.014	0.0010
G310.8-00.4	S	0.1	12.64	18.8	-0.7	0.12	0.0090	0.0030
G312.4-00.4	S	0.32	1.9	18.7	4.9	5.17	0.104	0.113
G315.4-00.3	?	0.16	8.61	20.5	1.2	0.28	0.016	0.0060
G315.4-02.3	S	0.35	2.8	40.0	12.1	5.1	0.142	0.052
G316.3-00.0	S	0.19	3.96	19.4	1.0	1.24	0.018	0.026
G317.3-00.2	S	0.09	15.89	28.2	2.7	0.11	0.024	0.0020
G318.2+00.1	S	0.31	12.61	31.6	7.1	0.2	0.073	0.0030
G318.9+00.4	C	0.2	14.32	29.4	1.1	0.14	0.019	0.0020
G321.9-00.3	S	0.23	5.25	28.3	1.4	1.03	0.023	0.015
G321.9-01.1	S	0.23	15.48	35.6	-1.7	0.15	0.0050	0.0020
G326.3-01.8	C	0.32	0.95	18.4	0.1	20.47	0.032	0.455
G327.1-01.1	C	0.15	9.81	24.9	2.8	0.26	0.034	0.0040
G327.4+00.4	S	0.18	2.98	24.1	1.6	2.71	0.025	0.046
G328.4+00.2	F	0.04	7.84	25.7	0.2	0.42	0.01	0.0070
G329.7+00.4	S	0.31	2.33	13.6	0.0	2.5	0.041	0.075
G330.2+01.0	S?	0.09	15.1	12.4	1.3	0.05	0.015	0.0020
G332.0+00.2	S	0.1	9.98	8.8	4.3	0.09	0.054	0.0040
G332.4+00.1	S	0.12	3.66	7.6	11.3	0.57	0.149	0.031
G332.4-00.4	S	0.08	3.4	7.0	9.9	0.61	0.109	0.035
G335.2+00.1	S	0.18	4.82	11.3	3.8	0.49	0.06	0.018
G336.7+00.5	S	0.1	12.58	10.6	5.5	0.07	0.064	0.0030
G337.3+01.0	S	0.11	5.49	9.4	-0.9	0.31	0.01	0.014
G337.8-00.1	S	0.06	5.95	21.1	3.2	0.6	0.025	0.012
G338.1+00.4	S	0.12	16.47	22.3	1.9	0.08	0.029	0.0020
G338.3-00.0	C?	0.07	12.64	29.8	24.5	0.19	0.123	0.0030
G338.5+00.1	?	0.08	7.84	31.4	8.8	0.51	0.046	0.0070
G340.4+00.4	S	0.07	16.29	30.1	1.7	0.11	0.011	0.0020
G343.1-00.7	S	0.2	8.2	14.4	0.9	0.21	0.03	0.0060
G346.6-00.2	S	0.07	11.32	46.3	3.8	0.36	0.023	0.0030
G348.5+00.1	S	0.12	9.0	49.8	8.8	0.61	0.043	0.0050
G348.5-00.0	S?	0.08	8.8	41.0	4.1	0.53	0.031	0.0050
G348.7+00.3	S	0.14	9.0	54.1	9.1	0.67	0.042	0.0050
G349.7+00.2	S	0.02	13.8	25.8	3.6	0.14	0.016	0.0020
G350.0-02.0	S	0.38	2.68	4.7	-0.3	0.66	0.073	0.057
G351.7+00.8	S	0.13	7.6	16.0	-2.7	0.28	0.011	0.0070
G355.4+00.7	S	0.21	11.67	16.5	0.6	0.12	0.024	0.0030
G355.9-02.5	S	0.11	9.74	1.9	0.6	0.02	0.074	0.0040
G357.7+00.3	S	0.2	6.73	41.2	1.5	0.91	0.023	0.0090
G357.7-00.1	?	0.05	3.64	33.6	4.1	2.54	0.017	0.031
G358.5-00.9	S	0.14	15.84	75.4	8.2	0.3	0.035	0.0020
Σ_{1-99}			< 8.07 >	2554.5	21.18	235.8	0.0144	0.0378

Table 6.10: Analysis results for SNRs observed with H.E.S.S., which have no known non-SNR counterpart and for which a theoretical flux prediction is available but no significant flux has been measured. The table is indexed similar to Table 6.9. The last column gives the product $\theta E_{SN} n$, calculated according to equation 5.20 from the upper limit at a 99 % confidence level and the distance given in the table.

SNR	Type	Radius [deg]	Distance [kpc]	Exposure [h]	Significance [σ]	Weight Exposure/ Distance^2 [h/kpc^2]	Upper limit 99% CL [CU]	Theoret. flux pred. [CU]	$\theta E_{SN} n$ [10^{51} ergcm^{-3}]
G005.4-01.2	C?	0.29	2.31	22.7	2.5	4.24	0.041	0.076	0.05
G006.1+00.5	S	0.13	14.85	20.0	1.7	0.09	0.019	0.002	1.0
G006.1+01.2	F	0.23	13.53	26.2	-1.3	0.14	0.011	0.002	0.48
G008.9+00.4	S	0.2	7.32	25.3	1.4	0.47	0.028	0.008	0.37
G009.9-00.8	S	0.1	11.54	36.7	-0.1	0.28	0.006	0.003	0.2
G011.1-01.0	S	0.13	12.05	27.0	-0.5	0.19	0.006	0.003	0.22
G013.3-01.3	S?	0.48	3.0	6.3	-1.3	0.7	0.063	0.045	0.14
G015.1-01.6	S	0.23	10.52	31.3	-4.7	0.28	0.003	0.004	0.09
G017.4-02.3	S	0.2	12.23	30.2	1.5	0.2	0.016	0.003	0.6
G017.8-02.6	S	0.2	14.21	45.2	0.3	0.22	0.007	0.002	0.32
G018.8+00.3	S	0.12	8.1	12.4	1.3	0.19	0.022	0.006	0.36
G018.9-01.1	C?	0.28	2.26	30.8	-0.6	6.03	0.022	0.080	0.03
G019.1+00.2	S	0.22	6.49	7.2	0.9	0.17	0.052	0.010	0.53
G020.0-00.2	F	0.08	8.8	14.3	2.0	0.18	0.018	0.005	0.34
G021.8-00.6	S	0.17	1.68	28.2	2.0	9.98	0.023	0.145	0.02
G023.6+00.3	?	0.08	10.56	20.3	1.5	0.18	0.019	0.004	0.51
G030.7+01.0	S?	0.18	10.58	29.1	-0.3	0.26	0.012	0.004	0.32
G031.9+00.0	S	0.05	7.2	42.2	0.0	0.81	0.006	0.008	0.07
G039.2-00.3	C	0.06	6.09	31.5	0.5	0.85	0.011	0.011	0.1
G039.7-02.0	?	0.79	1.04	11.1	0.6	10.2	0.053	0.376	0.01
G043.3-00.2	S	0.03	7.5	28.8	1.0	0.51	0.007	0.007	0.09
G043.9+01.6	S?	0.5	5.75	11.5	-1.2	0.35	0.035	0.012	0.29
G045.7-00.4	S	0.18	14.03	24.2	2.2	0.12	0.024	0.002	1.14
G046.8-00.3	S	0.13	6.4	16.9	0.9	0.41	0.013	0.010	0.13
G053.6-02.2	S	0.26	5.0	3.9	-0.7	0.16	0.019	0.016	0.11
G054.4-00.3	S	0.33	2.62	19.8	-0.5	2.89	0.013	0.038	0.02
G279.0+01.1	S	0.79	1.98	1.0	1.7	0.26	0.392	0.105	0.37
G289.7-00.3	S	0.13	11.22	16.3	0.3	0.13	0.022	0.003	0.69
G290.1-00.8	S	0.14	2.48	16.5	0.7	2.67	0.021	0.066	0.03
G291.0-00.1	C	0.12	5.44	26.5	2.7	0.9	0.021	0.014	0.15
G292.0+01.8	C	0.08	6.31	16.8	2.6	0.42	0.020	0.010	0.19
G293.8+00.6	C	0.17	12.52	14.9	0.9	0.1	0.036	0.003	1.39
G296.1-00.5	S	0.26	7.4	14.6	-0.2	0.27	0.022	0.007	0.29
G296.8-00.3	S	0.14	8.1	18.3	0.4	0.28	0.022	0.006	0.35
G298.6-00.0	S	0.09	15.27	18.0	3.8	0.08	0.025	0.002	1.45
G302.3+00.7	S	0.14	13.17	11.9	1.8	0.07	0.026	0.002	1.09
G304.6+00.1	S	0.07	7.9	79.6	4.4	1.28	0.009	0.007	0.14
G308.8-00.1	C?	0.21	4.79	17.6	1.7	0.77	0.042	0.018	0.24
G309.2-00.6	S	0.11	10.71	21.8	-0.0	0.19	0.020	0.004	0.55
G309.8+00.0	S	0.19	3.6	19.6	1.3	1.51	0.024	0.032	0.07
G310.6-00.3	S	0.07	16.69	19.1	1.2	0.07	0.014	0.001	0.95
G310.8-00.4	S	0.1	12.64	18.8	-0.7	0.12	0.009	0.003	0.34
G315.4-00.3	?	0.16	8.61	20.5	1.2	0.28	0.016	0.006	0.28
G316.3-00.0	S	0.19	3.96	19.4	1.0	1.24	0.018	0.026	0.07
G318.9+00.4	C	0.2	14.32	29.4	1.1	0.14	0.019	0.002	0.93
G321.9-00.3	S	0.23	5.25	28.3	1.4	1.03	0.023	0.015	0.16
G321.9-01.1	S	0.23	15.48	35.6	-1.7	0.15	0.005	0.002	0.31
G326.3-01.8	C	0.32	0.95	18.4	0.1	20.47	0.032	0.455	0.01
G327.4+00.4	S	0.18	2.98	24.1	1.6	2.71	0.025	0.046	0.05
G328.4+00.2	F	0.04	7.84	25.7	0.2	0.42	0.010	0.007	0.15
G329.7+00.4	S	0.31	2.33	13.6	0.0	2.5	0.041	0.075	0.05
G330.2+01.0	S?	0.09	15.1	12.4	1.3	0.05	0.015	0.002	0.83
G337.3+01.0	S	0.11	5.49	9.4	-0.9	0.31	0.010	0.014	0.08
G338.1+00.4	S	0.12	16.47	22.3	1.9	0.08	0.029	0.002	1.92
G340.4+00.4	S	0.07	16.29	30.1	1.7	0.11	0.011	0.002	0.71
G343.1-00.7	S	0.2	8.2	14.4	0.9	0.21	0.030	0.006	0.5
G350.0-02.0	S	0.38	2.68	4.7	-0.3	0.66	0.073	0.057	0.13
G351.7+00.8	S	0.13	7.6	16.0	-2.7	0.28	0.011	0.007	0.16
G355.4+00.7	S	0.21	11.67	16.5	0.6	0.12	0.024	0.003	0.81
G355.9-02.5	S	0.11	9.74	1.9	0.6	0.02	0.074	0.004	1.71
G357.7+00.3	S	0.2	6.73	41.2	1.5	0.91	0.023	0.009	0.26
Σ_{1-61}			$< 8.3 >$	1318.3	-3.78	80.91	0.00057	0.0251	

6.3.2 Recommendation for further SNR observations

Using the theoretical flux prediction and experimental flux measurements it is possible to identify SNRs which have low exposure but have an upper limit close to the theoretical flux prediction. In particular those SNRs with few hours of observation time are suitable as targets for further observations, as the gain in VHE γ-ray excess can substantially change the current value. Therefore all SNRs with less exposure than 17 h are considered in the following and their experimental and theoretical flux values compared. Fig. 6.42 depicts upper limits at a 3σ confidence level (red triangles) and the corresponding theoretically predicted flux value (black triangles) for SNRs with an observation time of less than 17 h, for which only an upper limit can be given. For several of the theoretical values the error bars are hidden within the triangular marker.

For most of the SNRs the difference between the experimental and theoretical flux values is large and reaches a factor of 15. Three SNRs, G013.3-01.3, G053.6-02.2 (both Fig. 6.42(a)), and G350.0-02.0 (Fig. 6.42(b)) show a small difference between the flux values. These three SNRs will be discussed in the following, showing the excess map of the region of ~2 ° around each SNR. Red, blue and magenta circles in the images illustrate the position and size of the SNRs, H.E.S.S. sources and pulsars in the region, respectively. According to Aharonian et al. (2006a) the necessary amount of observation time to reach the theoretically predicted flux is given. It is calculated from

$$T_{necessary} = \frac{F^2_{theoret.}}{F^2_{UL}} \cdot T_{current} \,, \tag{6.7}$$

where $F_{theoret.}$ is the theoretically predicted flux value, F_{UL} the upper limit on the VHE γ-ray flux derived from H.E.S.S. observations and $T_{current}$ the currently accumulated observation time at the SNR position.

G013.3-01.3

The significance of the VHE γ-ray excess from the shell type SNR is -1.3σ after 6.3 h of observation time. The upper limit on the flux above 1 TeV at a 99% confidence level is $1.4{\cdot}10^{-12}\,\mathrm{cm}^{-2}\mathrm{s}^{-1}$. This value is close to the theoretical flux prediction of $1.0{\cdot}10^{-12}\,\mathrm{cm}^{-2}\mathrm{s}^{-1}$. The distance to the SNR given in Case & Bhattacharya (1998) is 3 kpc. The SNR is located close to the γ-ray source HESS J1813-178 but is not associated with the γ-ray emission. No other counterparts are nearby. Table 6.5 gives the value for $\theta E_{SN} n = 0.14{\cdot}10^{51}\,\mathrm{erg\ cm}^{-3}$ derived from the upper limit on the flux. To meet the predicted flux value additional observations of ~3 h are required for G013.3-01.3. Fig. 6.43 shows the excess map of G013.3-01.3 with a correlation radius of 0.1 °.

G053.6-02.2

The significance of the γ-ray excess from the shell type SNR is -0.7σ after 3.9 h of observation time. The upper limit on the flux at a 99% confidence level is $4.1{\cdot}10^{-13}\,\mathrm{cm}^{-2}\mathrm{s}^{-1}$. This value is close to the theoretical flux prediction of $3.6{\cdot}10^{-13}\,\mathrm{cm}^{-2}\mathrm{s}^{-1}$. The distance to the SNR given in Case & Bhattacharya (1998) is 5 kpc. The SNR is located ~2.5 °

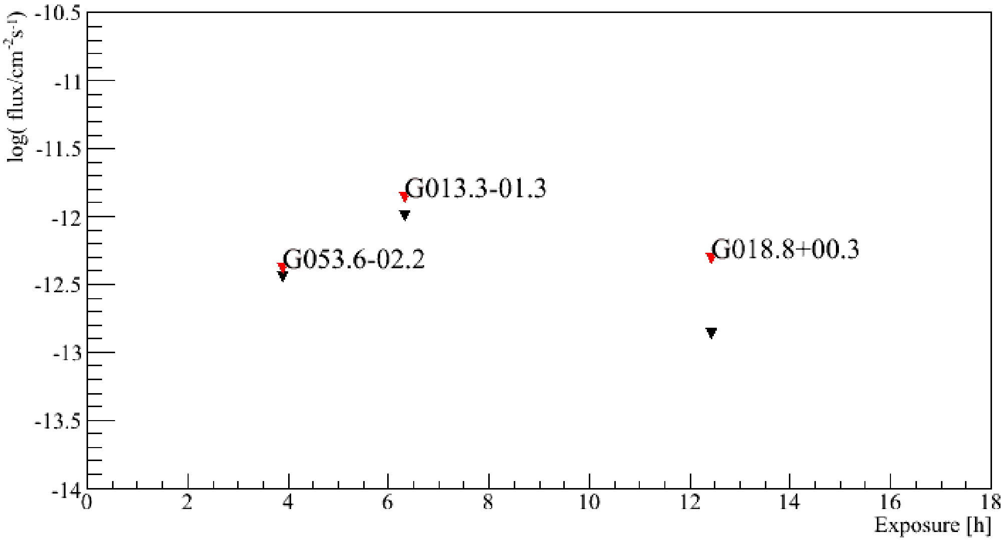

(a) SNRs with known distance

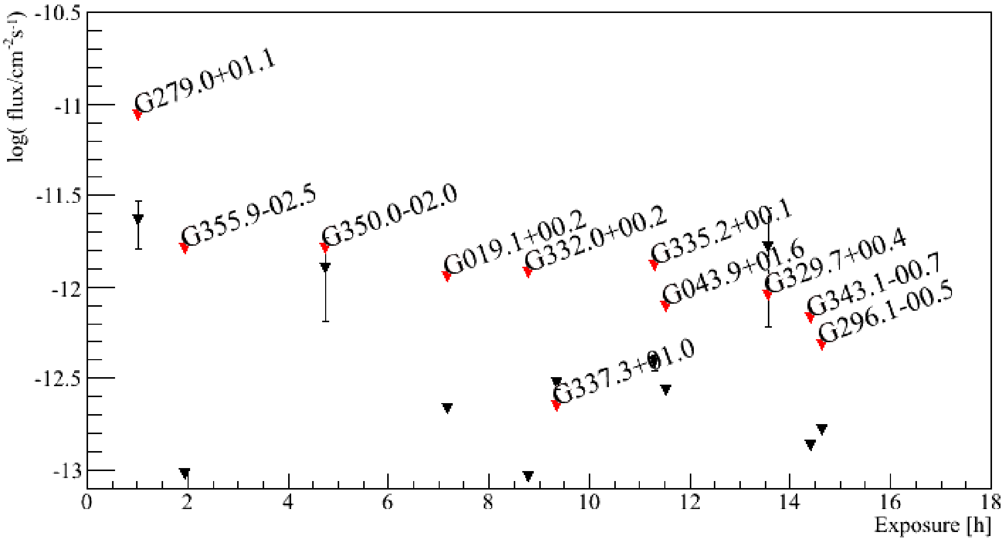

(b) SNRs with calculated distance

Figure 6.42: Illustration of 3σ upper limits (red triangles) and the corresponding theoretically predicted flux value (black triangles) for SNRs with an observation time of less than 17 h, for which only an upper limit can be given. (a) illustrates SNRs with known distance, (b) shows SNRs for which only a calculated distance can be given.

from the nearest γ-ray emission region and ∼1 ° from the pulsar PSR B1933+16. No other counterparts are nearby. Table 6.5 gives the value for $\theta E_{SN} n = 0.11 \cdot 10^{51}$ erg cm^{-3} derived from the upper limit on the flux. To meet the predicted flux value additional observations of ∼3 h are required for G053.6-02.2. Fig. 6.44 shows the excess map of G053.6-02.2 with a correlation radius of 0.1 °.

G350.0-02.0

The significance of the γ-ray excess from the shell type SNR is -0.3σ after 4.7 h of observation time. The upper limit on the flux at a 99% confidence level is $1.6 \cdot 10^{-12}\,\mathrm{cm}^{-2}\mathrm{s}^{-1}$. This value is close to the theoretical flux prediction of $1.3 \cdot 10^{-12}\,\mathrm{cm}^{-2}\mathrm{s}^{-1}$, derived from the calculated distance d =3.8 kpc. The SNR is located $\sim 2.3\,°$ from the nearest H.E.S.S.source HESS J1718-385. Table 6.6 gives the value for $\theta E_{SN} n = 0.25 \cdot 10^{51}$ erg cm^{-3} derived from the upper limit on the flux. The difference to the value used for the calculation of the predicted flux is considerable. To meet the predicted flux value additional observations of $\sim$3 h are required for G053.6-02.2. Fig. 6.45 shows the excess map of G350.0-02.0 with a correlation radius of 0.1 °.

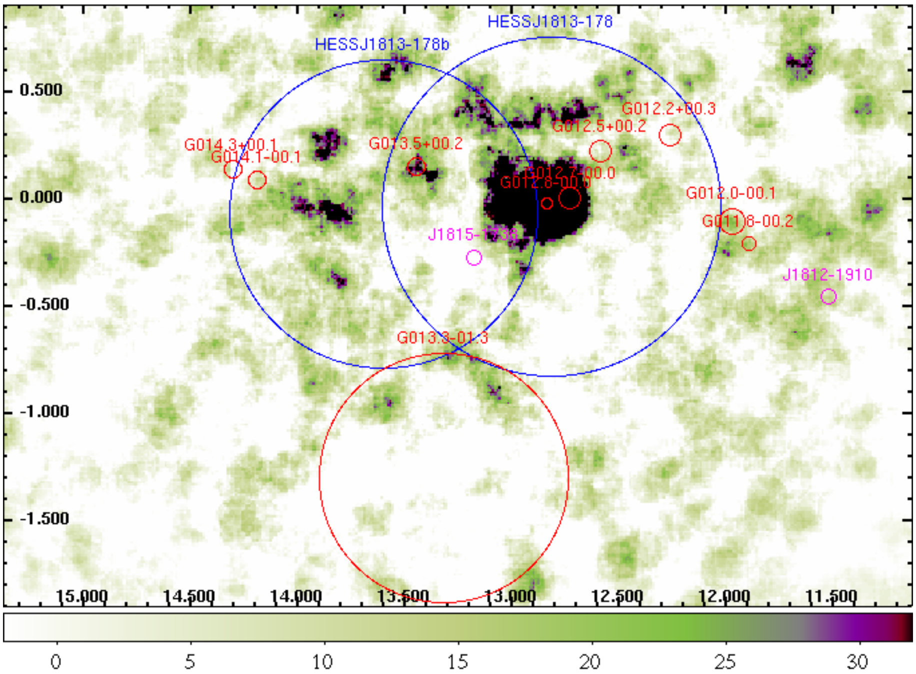

Figure 6.43: Excess map of G013.3-01.3 with a correlation radius of 0.1 °. The γ-ray signal is dominated by statistical fluctuations.

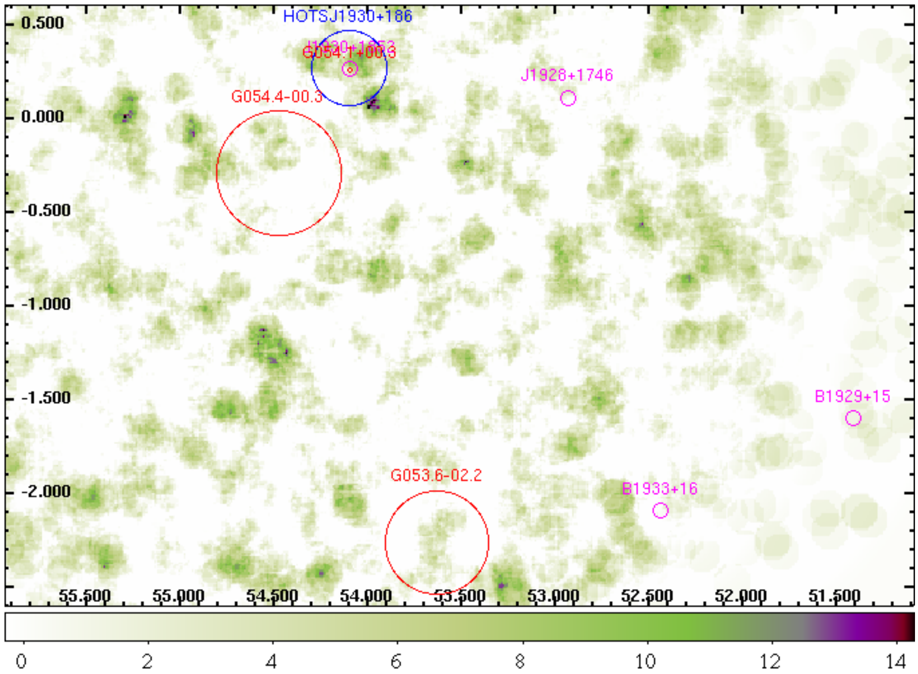

Figure 6.44: Excess map of G053.6-02.2 with a correlation radius of 0.1 °. No known γ-ray emission region is nearby the SNR.

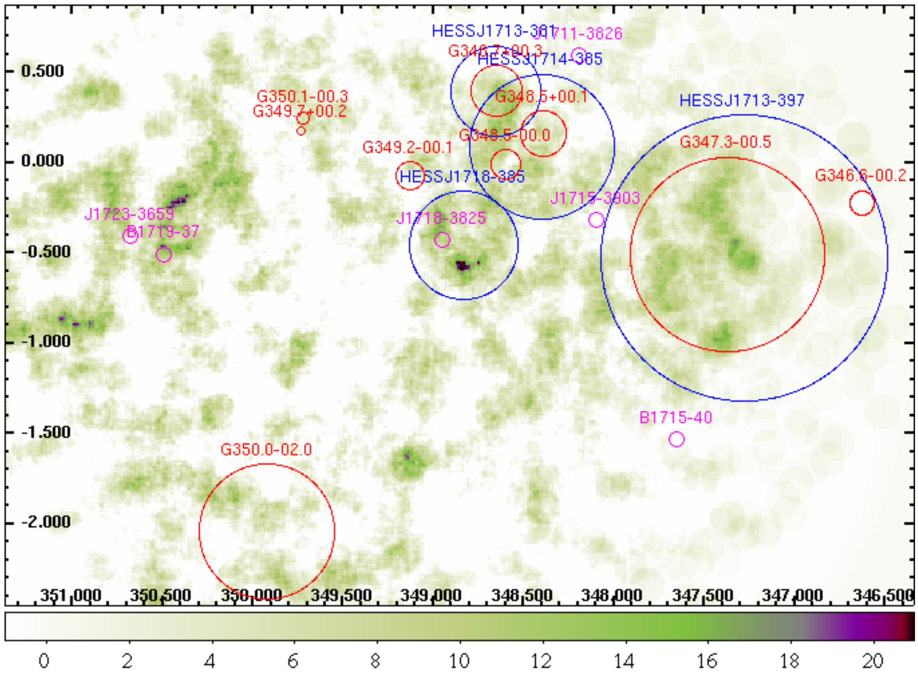

Figure 6.45: Excess map of G350.0-02.0 with a correlation radius of 0.1 °.

6.4 Spatial correlation of SNRs with H.E.S.S.

The detection of VHE γ-rays generated in low-density regions of the ISM is rather difficult due to the low interaction rate. However, Aharonian (2004) discusses the illumination of molecular clouds (MCs), either when the SN occurs within the MC or when the shell overtakes a nearby MC. In the following, the scenario of MCs being illuminated by shell-type SNRs is investigated. Therefore the distance between the radio SNRs and known VHE γ-ray emission regions is compared to the distance resulting, when a sample of SNRs with simulated positions is considered. The positions of 157 shell type SNRs from Green's catalog are compared to VHE γ-ray emission regions detected with the H.E.S.S. instrument. A higher rate of VHE γ-ray detections at small distances between the SNRs and H.E.S.S. sources of $\sim 1°$ would support the prediction of VHE γ-ray production within the SNR or its shell. The maximum of VHE γ-ray sources being at distances of a few degrees from the SNRs could be an indication of VHE γ-ray emission from MCs.

6.4.1 Simulation of SNR sample

Of the total number of 203 SNRs, 157 are of shell type. Among these, 18 have not been definitely confirmed to be shell type but are still considered as part of the test sample. These SNRs are characterized by distributions in galactic latitude and longitude and in radius. Following the distributions of the catalog SNRs 10,000 new samples of each 157 SNRs are generated. The catalog and simulated distributions are shown in Fig. 6.46. The fit functions used are the sum of a Gaussian and a first order polynomial for the galactic latitude, a Gaussian for the galactic longitude and a Landau function for the radius. The fit parameters are given in the figures. The simulated sample of SNRs is generated using the fit of the catalog sample.

6.4.2 Distance to H.E.S.S. sources

For both the catalog and the simulated sample, the distance to known H.E.S.S. sources is calculated. The distance distributions as well as the fractional difference between catalog and simulated distances are shown in Fig. 6.47.

The left side of Fig. 6.47 (a, c, e) shows the distance to VHE γ-ray emission regions, whereas the right side (b, d, f) illustrates distances to potential H.E.S.S. sources, which show VHE γ-ray emission above a certain level but do not fulfill the 5σ requirement of source detection yet. Both samples are generated from the database of exclusion regions, which are conservatively created around VHE γ-ray emission regions with a certain significance of the VHE γ-ray excess. The catalog distributions (Figs. a and b) reflect the increasing number of detections for distances up to $\sim 10°$. Distances between H.E.S.S. sources and simulated SNRs (Fig. c) roughly follow the same distribution, with many SNR at small distances and decreasing numbers of SNRs with a distance of more than $\sim 10°$. The peaks emerging in Fig. c occur at distances of more than $\sim 20°$ for the distance distribution between simulated and also real SNRs. The distribution of distances between SNRs and Hotspots is much broader. This reflects the smaller number of Hotspots compared to the total number of exclusion regions. The fractional distance distributions both

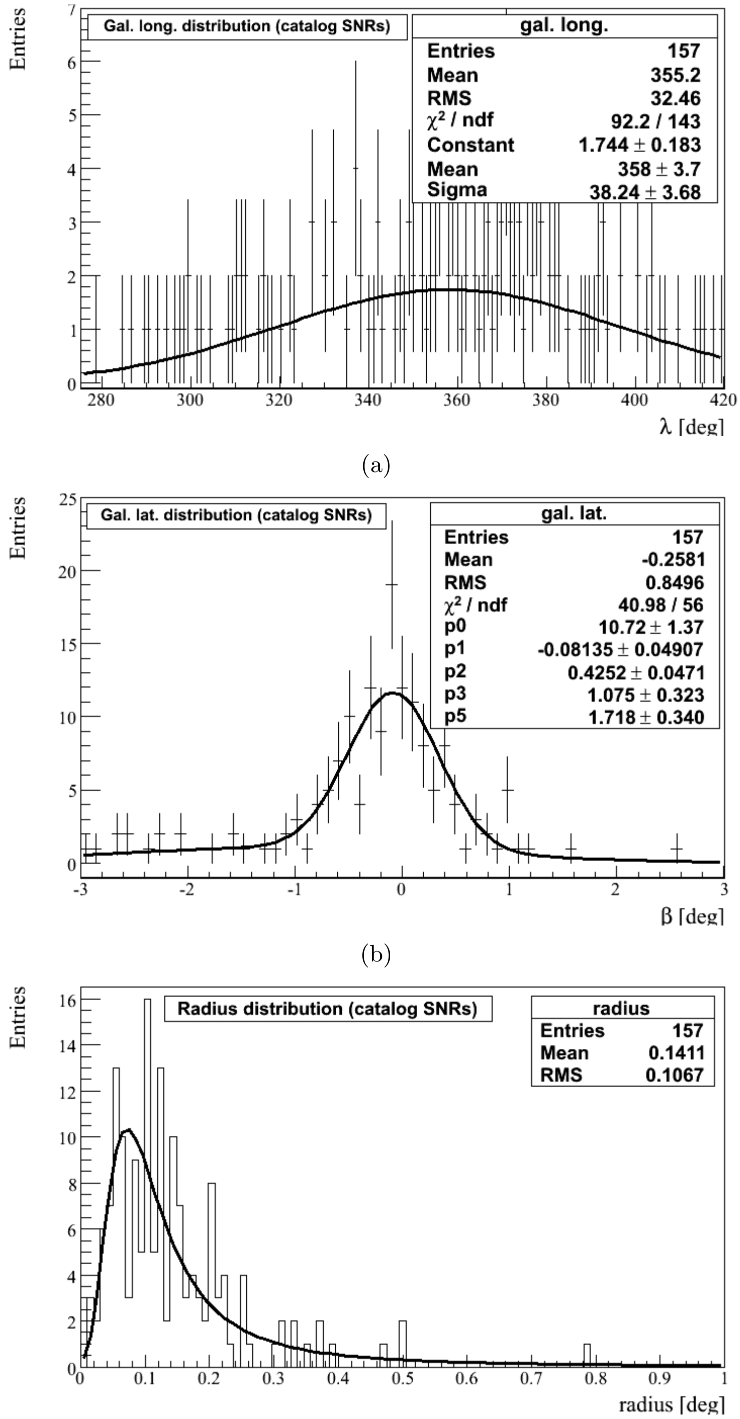

(a)

(b)

(c)

Figure 6.46: The plots show the distribution of 157 shell type SNRs from Green's catalog in (a) the galactic latitude interpolated with the sum of a Gaussian and a first order polynomial, (b) the galactic longitude interpolated with a Gaussian, and (c) the radius fitted by a Landau function.

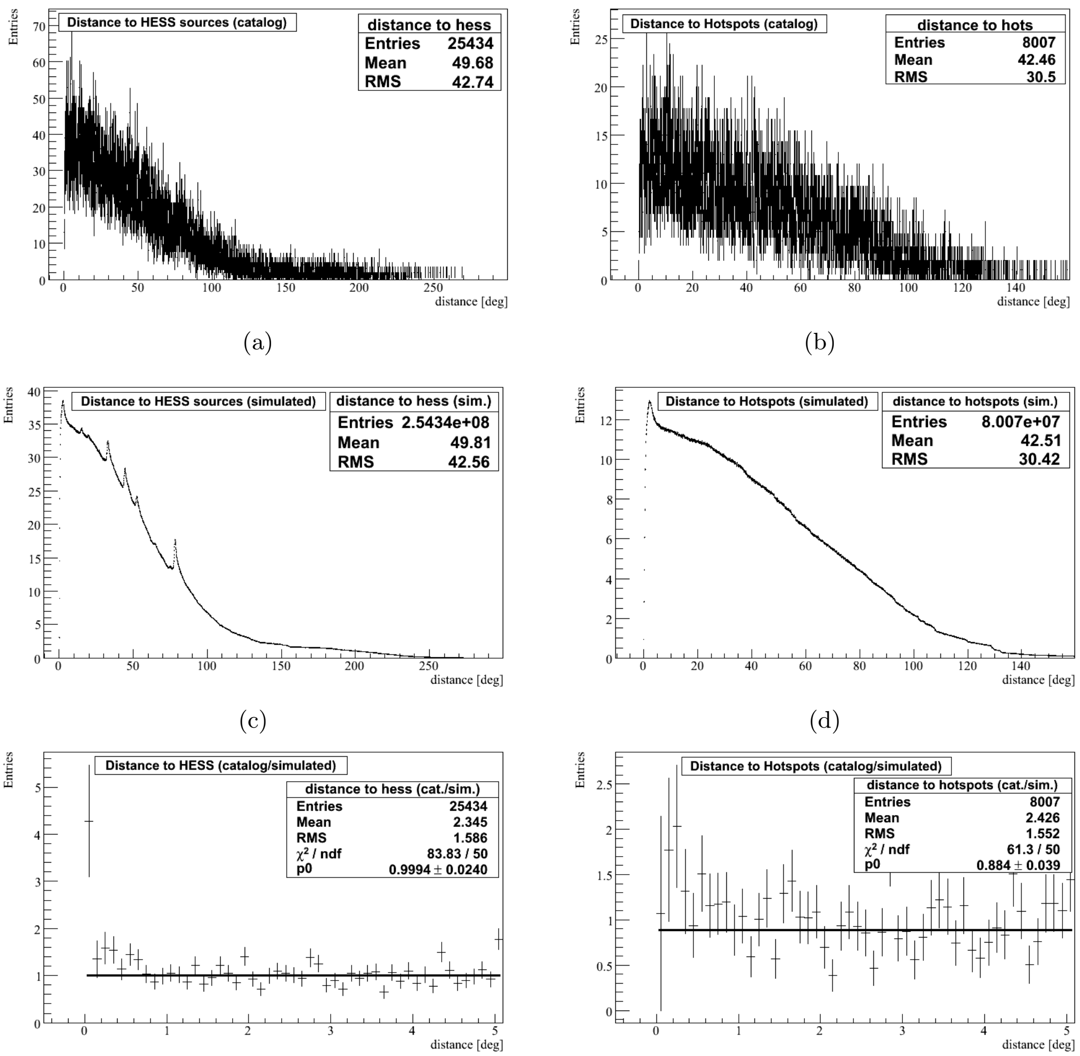

(a) (b)

(c) (d)

(e) (f)

Figure 6.47: Distribution of distances between radio SNRs and VHE γ-ray emission regions (left side) and potential VHE γ-ray sources (right side).

show an excess of SNRs at distances close to zero. In the case of distances to the entire list of exclusion regions (Fig. e) these represent the coincidences of SNRs with VHE γ-ray sources. In the case of potential VHE γ-ray sources (Fig. f) the excess is not directly at zero but at a distance of $\sim 0.3^\circ$ between the VHE γ-ray emission region and the SNR. In both cases, no significant excess at a distance of a few degrees appears in the fractional distance distribution.

As a result from the above considerations, the observation of distances between radio SNRs and TeV γ-ray emission regions does not indicate the general illumination of nearby MCs. A further study could provide more details on the positions of known MCs. It should also involve the consideration of only those SNRs, which are not confused with γ-ray emission regions resulting from non-SNR counterparts.

7 Conclusion and future perspectives

The H.E.S.S. experiment, an array of currently four Čerenkov telescopes, has been built to image air showers generated by very-high-energy (VHE) γ-rays in the energy range between 100 GeV and 100 TeV. Through the detection of VHE γ-rays, which are the result of hadronic interactions or inverse Compton processes of VHE cosmic rays, it is possible to identify cosmic accelerators. Since the beginning of γ-ray astronomy over 100 VHE γ-ray sources have been detected. Among these are pulsars, pulsar wind nebulae, supernova remnants (SNRs), and binary systems, but also extragalactic sources. Due to the large amount of energy released during a supernova explosion, SNRs are widely believed to be accelerators of cosmic rays, although the precise acceleration processes are still not completely understood.

In this work, a systematic study of VHE γ-radiation emitted by SNRs has been presented, based on data taken with the H.E.S.S. experiment during a deep survey of the Galactic plane and dedicated observations. After the discovery of over 50 VHE γ-ray sources with the H.E.S.S. detector during the past years and meanwhile about 2000 h of observation time in the inner Galactic region, the available data allows to study individual VHE γ-ray sources as well as to investigate large samples of SNRs. The present study tries to confirm statistically the hypothesis that SNRs provide enough energy to act efficiently as cosmic accelerators and represent VHE γ-ray production sites. Theoretical considerations predict the VHE γ-ray flux generated by hadronic interactions based on characteristic SNR parameters. These parameters are the supernova explosion energy E_{SN}, the acceleration efficiency θ, and the density n of the surrounding medium. Their product is suggested to be $\theta E_{SN} n \approx 0.1 \cdot 10^{51}$ erg cm^{-3}. The distance of SNRs can be determined experimentally or derived from their apparent size and brightness in radio. Until now, only 10 out of over 200 SNRs known in the radio waveband have been associated with VHE γ-ray emission regions. This study therefore aims at investigating the VHE γ-ray signal from the ensemble of radio SNRs, resulting in either significant VHE γ-ray fluxes or upper limits on the VHE γ-ray flux. The comparison of the measured VHE γ-ray flux of such a large ensemble of SNRs with theoretical flux predictions allows for the first time to investigate the parameters employed in the theoretical model.

Including previously confirmed SNR-γ-ray associations, 47 of the observed SNRs show a significant VHE γ-ray excess in H.E.S.S. data. Among these are several SNRs, which are currently investigated as new VHE γ-ray source discoveries, while many others are contaminated by a spill-over of γ-rays from the emission region without being the origin of the emission. The values for $\theta E_{SN} n$ obtained for individual SNRs differ by up to an order of magnitude from the value suggested for the theoretical flux prediction. This implies that the individual parameters used within this study are not appropriate for all considered SNRs. However, assuming the theoretical model to be approximately suitable, a recommendation for further observation can be given for three SNRs whose flux measurements are close to the theoretical predictions. For a detection in VHE γ-rays, G013.3-01.3, G053.6-02.2, and G350.0-02.0 require an additional observation time of ~3 h, each.

The difference for a sample of 19 SNRs found between HEGRA and H.E.S.S. results is considerable, however, expected. While upper limits of the individual SNRs determined from HEGRA data are over an order of magnitude above the theoretically predicted flux value, current H.E.S.S. data yield individual upper limits close to the prediction or below, confirming actual H.E.S.S. detections. Considering HEGRA data, the ensemble limit of 6 % of the Crab nebula's flux, derived from the stacked VHE γ-ray signal of the 19 SNRs, was about a factor of 2 above the theoretical predictions. With increased exposure and sensitivity, current H.E.S.S. data yields an ensemble limit of ~2 % of the Crab flux.

The investigation of spatial coincidence of radio SNRs with known H.E.S.S. sources underlines the connection between SNR positions and VHE γ-ray emission regions. An excess of SNRs at a distance of few degrees, which would hint at the illumination of nearby molecular clouds with cosmic rays, is not observed. The comparison of distances between known VHE γ-ray emission regions and SNRs on the one hand and a simulated SNR sample on the other hand shows a small excess of SNRs for distances to H.E.S.S. sources close to zero, resulting from actual SNR-γ-ray associations.

With the actual sensitivity of the H.E.S.S. instrument and the available amount of data this thesis presents the currently most detailed study of SNRs in VHE γ-ray sky. Future instruments like the Čerenkov Telescope Array (CTA) are expected to increase the number of detected VHE γ-ray sources, especially from distant and young SNRs, which are too faint for current detectors. Dedicated observations of SNRs in other wavelengths will lead to further constraints on parameters, which describe particle acceleration and VHE γ-ray production processes, as well as the different environment of individual SNRs. Especially the distance determination will benefit enormously from modern experimental techniques and allow for more reliable theoretical flux predictions.

A first taste of what is to come with future detectors is given by the current upgrade of the H.E.S.S. experiment to phase II. A fifth Čerenkov telescope, CT 5, with a much larger mirror area is currently being added to the existing array. With this new telescope it will be possible to extend the measurable spectrum of VHE γ-rays down to ~50 GeV. This is only possible if the multiplicity condition, requesting at least two camera images of the same air shower, is not applied for CT 5. This requires hardware and software changes within the central trigger system of the detector. During this thesis a solution for the upgrade of the central trigger system of the extended H.E.S.S. array has been developed and tested. After completion of all changes the central trigger electronics will allow to generate two different types of events: stereo events including at least two telescopes and mono events with data from CT 5 only. The necessary test procedure for the internal trigger electronics as well as for interface tests with the camera of CT 5 has been developed.

In summary it can be stated that 40 years after its first use, the Imaging Atmospheric Čerenkov Technique still represents a very powerful experimental technique. Detections of individual VHE γ-ray sources as well as statistical ensemble studies allow for exciting discoveries in the field. With the upcoming era of very large arrays of tens to hundreds of Čerenkov telescopes we can expect to further approach the remaining puzzles of the VHE universe.

A Appendix

A.1 List of SNRs with known or calculated distance

Table A.1: SNRs with known or calculated distance.

SNR	Known distance [kpc]	Calculated distance [kpc]	Error of calc. distance [kpc]
G000.0+00.0	-	2.12	0.81
G000.3+00.0	-	4.44	0.25
G001.0-00.1	-	6.79	0.16
G006.5-00.4	-	3.37	0.51
G008.7-00.1	-	1.27	0.46
G008.9+00.4	-	7.32	0.15
G013.3-01.3	3.0	-	-
G018.8+00.3	8.1	3.09	0.56
G019.1+00.2	-	6.49	0.17
G021.8-00.6	-	1.68	0.34
G022.7-00.2	-	2.62	0.66
G023.3-00.3	-	1.55	0.37
G024.7-00.6	-	9.31	0.1
G031.9+00.0	7.2	5.08	0.22
G032.8-00.1	-	6.92	0.16
G033.6+00.1	7.1	4.69	0.24
G040.5-00.5	-	6.4	0.17
G041.1-00.3	-	6.35	0.17
G043.3-00.2	7.5	4.17	0.26
G043.9+01.6	-	5.75	0.19
G046.8-00.3	6.4	5.91	0.19
G049.2-00.7	6.0	0.94	0.61
G053.6-02.2	5.0	7.48	0.15
G054.4-00.3	3.3	2.62	0.66
G279.0+01.1	-	1.98	0.29
G284.3-01.8	-	6.23	0.18
G290.1-00.8	-	2.48	0.7
G292.2-00.5	-	9.87	0.09
G296.1-00.5	-	7.4	0.15
G296.8-00.3	-	8.1	0.11
G304.6+00.1	7.9	7.18	0.15
G309.8+00.0	3.6	4.52	0.24
G312.4-00.4	-	1.9	0.3
G315.4-02.3	2.8	1.75	0.33
G316.3-00.0	-	3.96	0.44
G321.9-00.3	-	5.25	0.21
G327.4+00.4	-	2.98	0.58
G329.7+00.4	-	2.33	0.74
G332.0+00.2	-	9.98	0.09
G332.4+00.1	-	3.66	0.47
G332.4-00.4	3.4	3.89	0.44
G335.2+00.1	-	4.82	0.23
G337.3+01.0	-	5.5	0.2

Continued on next page

Table A.1 – continued from previous page

SNR	Known distance [kpc]	Calculated distance [kpc]	Error of calc. distance [kpc]
G337.8-00.1	-	5.95	0.19
G343.1-00.7	-	8.2	0.11
G348.5+00.1	9.0	1.76	0.33
G348.5-00.0	-	8.8	0.1
G348.7+00.3	9.0	3.53	0.49
G349.7+00.2	13.8	7.93	0.14
G350.0-02.0	-	2.68	0.65
G351.7+00.8	-	7.6	0.14
G355.9-02.5	-	9.74	0.09
G357.7+00.3	-	6.73	0.16
G359.0-00.9	-	3.55	0.49
G359.1-00.5	9.2	5.15	0.21

A.2 Analysis results for all SNRs observed with H.E.S.S.

Table A.2: Analysis results of individual SNRs. The assumed spectral index for the flux determination has been set to 2.1.

SNR	Type	Radius	Distance		Expo-sure-	Signi-ficance	Excess	Excess	Integral flux	Upper Limit		Theoretical flux prediction		
			known	calc.				Lower limit		99% CL	68% CL	known dist.	calc. dist.	error
		[deg]	[kpc]	[kpc].	[h]	[σ]	[counts]	[counts]	[$\log_{10}\mathrm{cm}^{-2}\mathrm{s}^{-1}$]	[$\log_{10}\mathrm{cm}^{-2}\mathrm{s}^{-1}$]		[$\log_{10}\mathrm{cm}^{-2}\mathrm{s}^{-1}$]	[$\log_{10}\mathrm{cm}^{-2}\mathrm{s}^{-1}$]	[$\log_{10}\mathrm{cm}^{-2}\mathrm{s}^{-1}$]
G000.0+00.0	S	0.03	–	3.3	138.2	66.6	3425.0	2571.0	-11.64	-11.62	-11.63	–	-11.7	-11.82
G000.3+00.0	S	0.1	–	5.0	115.4	12.6	744.3	402.0	-12.27	-12.18	-12.23	–	-12.34	-13.29
G000.9+00.1	C	0.07	–	5.8	97.4	19.9	905.2	575.9	-12.07	-12.01	-12.05	–	-12.58	-13.78
G001.0-00.1	S	0.07	–	6.3	128.2	11.5	583.7	328.1	-12.39	-12.29	-12.35	–	-12.71	-14.03
G001.4-00.1	S	0.08	–	14.1	91.4	6.5	303.2	137.5	-12.51	-12.37	-12.45	–	–	–
G001.9+00.3	S	0.01	–	31.6	78.6	0.4	10.8	0.0	-13.69	-13.01	-13.3	–	–	–
G003.7-00.2	S	0.1	–	12.8	25.6	2.2	58.1	0.0	-12.79	-12.38	-12.58	–	–	–
G003.8+00.3	S?	0.15	–	10.8	35.6	2.5	91.5	1.7	-12.62	-12.3	-12.47	–	–	–
G005.2-02.6	S	0.15	–	11.5	1.9	0.2	1.4	0.0	–	-12.28	-13.41	–	–	–
G005.4-01.2	C?	0.29	–	3.5	22.7	2.5	130.6	0.0	-12.48	-12.05	-12.26	–	-11.77	-11.96
G005.5+00.3	S	0.11	–	8.8	35.8	3.8	129.2	17.9	-12.56	-12.29	-12.43	–	-13.28	–
G006.1+00.5	S	0.13	–	9.4	20.0	1.7	46.5	0.0	-13.08	-12.39	-12.68	–	-13.39	–
G006.1+01.2	F	0.23	–	8.9	26.2	-1.3	-57.7	0.0	–	-12.63	-13.63	–	-13.31	–
G006.4-00.1	C	0.4	–	1.3	19.8	5.5	397.3	173.6	-11.72	-11.56	-11.65	–	-10.69	-10.28
G006.5-00.4	S	0.15	–	4.3	32.7	4.8	194.0	92.4	-12.2	-12.03	-12.13	–	-12.1	-12.62
G007.0-00.1	S	0.12	–	12.0	37.8	1.7	66.5	0.0	-12.85	-12.43	-12.64	–	–	–
G007.2+00.2	S	0.1	–	11.9	32.9	2.4	76.2	0.0	-12.74	-12.39	-12.57	–	–	–
G008.3-00.0	S	0.04	–	19.8	23.2	14.6	277.3	151.1	-11.98	-11.89	-11.94	–	–	–
G008.7-00.1	S?	0.38	–	2.4	23.1	17.8	1051.0	602.2	-11.36	-11.29	-11.33	–	-11.25	-11.39
G008.9+00.4	S	0.2	–	6.5	25.3	1.4	49.0	0.0	-12.59	-12.21	-12.4	–	-12.78	-14.16
G009.7-00.0	S	0.11	–	10.4	39.1	2.4	72.0	0.0	-13.03	-12.55	-12.78	–	–	–
G009.8+00.6	S	0.1	–	10.3	33.8	-0.2	-4.9	0.0	-13.1	-12.56	-12.81	–	–	–
G009.9-00.8	S	0.1	–	8.2	36.7	-0.1	-3.8	0.0	–	-12.87	-13.54	–	-13.17	–
G010.5-00.0	S	0.05	–	21.4	36.3	4.6	98.7	24.4	-12.65	-12.43	-12.55	–	–	–
G011.0-00.0	S	0.08	–	16.9	38.7	14.8	442.9	286.1	-11.95	-11.87	-11.92	–	–	–
G011.1+00.1	S	0.09	–	13.1	37.6	10.4	310.0	184.6	-12.09	-11.99	-12.05	–	–	–
G011.1-00.7	S	0.08	–	19.1	32.5	0.0	1.0	0.0	–	-12.77	-13.19	–	–	–
G011.1-01.0	S	0.13	–	8.4	27.0	-0.5	-13.5	0.0	–	-12.86	-13.82	–	-13.21	–
G011.2-00.3	C	0.03	–	6.0	38.4	5.5	110.8	33.3	-12.62	-12.43	-12.53	–	-12.63	-13.87
G011.4-00.1	S?	0.07	–	9.2	36.8	4.5	108.1	28.8	-12.6	-12.38	-12.5	–	-13.36	–
G011.8-00.2	S	0.03	–	25.3	31.4	1.7	29.6	0.0	-13.52	-12.79	-13.09	–	–	–
G012.0-00.1	?	0.06	–	11.8	29.3	0.7	12.9	0.0	-13.09	-12.6	-12.84	–	–	–
G012.2+00.3	S	0.05	–	22.8	25.3	2.4	41.4	11.6	-12.66	-12.4	-12.54	–	–	–
G012.5+00.2	C?	0.05	–	25.7	20.5	4.7	77.6	15.1	-12.57	-12.33	-12.46	–	–	–
G012.7-00.0	S	0.05	–	22.5	18.4	19.3	364.2	243.5	-11.73	-11.66	-11.7	–	–	–
G012.8-00.0	C?	0.03	–	25.1	19.4	24.3	411.1	280.3	-11.71	-11.64	-11.68	–	–	–
G013.3-01.3	S?	0.48	3.0	–	6.3	-1.3	-53.1	0.0	-14.08	-11.86	-12.27	-12.0	–	–
G013.5+00.2	S	0.04	–	12.6	13.1	3.3	43.0	8.0	-12.53	-12.26	-12.4	–	–	–
G014.1-00.1	S	0.05	–	27.7	10.0	0.8	10.0	0.0	-13.71	-12.55	-12.92	–	–	–
G014.3+00.1	S	0.04	–	26.5	10.3	1.8	20.3	0.0	-12.81	-12.38	-12.6	–	–	–
G015.1-01.6	S	0.23	–	7.8	31.3	-4.7	-198.3	0.0	–	-13.13	-14.49	–	-13.09	–
G015.4+00.1	S	0.12	–	8.6	28.1	1.6	43.0	16.2	-12.51	-12.24	-12.38	–	-13.25	–
G015.9+00.2	S?	0.05	–	10.4	42.4	1.4	30.6	0.0	-13.05	-12.65	-12.85	–	–	–
G016.0-00.5	S	0.11	–	11.9	48.0	0.3	9.3	0.0	-13.51	-12.7	-13.02	–	–	–
G016.2-02.7	S	0.14	–	12.9	49.7	2.8	109.3	0.0	-12.84	-12.46	-12.65	–	–	–
G016.4-00.5	S	0.11	–	9.5	35.8	1.9	55.9	2.9	-12.71	-12.4	-12.56	–	-13.42	–
G016.7+00.1	C	0.03	–	13.8	61.0	4.6	115.5	33.7	-12.76	-12.55	-12.67	–	–	–
G016.8-01.1	?	0.23	–	12.0	44.6	19.8	1194.0	738.6	-11.63	-11.57	-11.61	–	–	–

Continued on next page

Table A.2 – continued from previous page

SNR	Type	Radius	Distance		Expo-	Signi-	Excess	Excess	Integral flux	Upper Limit		Theoretical flux prediction		
			known	calc.	sure-	ficance		Lower limit		99% CL	68% CL	known dist.	calc. dist.	error
		[deg]	[kpc]	[kpc].	[h]	[σ]	[counts]	[counts]	[$\log_{10}$cm^{-2}s^{-1}]	[$\log_{10}$cm^{-2}s^{-1}]		[$\log_{10}$cm^{-2}s^{-1}]	[$\log_{10}$cm^{-2}s^{-1}]	[$\log_{10}$cm^{-2}s^{-1}]
G017.0-00.0	S	0.04	–	28.2	59.5	6.6	173.9	45.1	-12.68	-12.49	-12.59	–	–	–
G017.4-00.1	S	0.05	–	30.0	51.3	12.6	335.9	191.6	-12.19	-12.1	-12.15	–	–	–
G017.4-02.3	S	0.2	–	8.5	30.2	1.6	59.0	0.0	-13.41	-12.44	-12.79	–	-13.22	–
G017.8-02.6	S	0.2	–	9.1	45.2	0.3	13.4	0.0	–	-12.84	-13.81	–	-13.35	–
G018.1-00.1	S	0.07	–	10.3	34.0	6.9	161.5	82.8	-12.29	-12.15	-12.23	–	–	–
G018.6-00.2	S	0.05	–	17.8	21.6	2.8	46.0	12.4	-12.58	-12.33	-12.46	–	–	–
G018.8+00.3	S	0.12	8.1	4.1	12.4	1.3	23.1	0.0	-12.97	-12.31	-12.59	-12.86	-12.03	-12.47
G018.9-01.1	C?	0.28	–	3.4	30.8	-0.6	-28.4	0.0	-13.13	-12.31	-12.63	–	-11.75	-11.92
G019.1+00.2	S	0.22	–	6.1	7.2	0.9	19.6	0.0	-12.4	-11.95	-12.17	–	-12.67	-13.95
G020.0-00.2	F	0.08	–	7.2	14.3	2.0	33.3	0.0	-12.95	-12.4	-12.65	–	-12.94	-14.57
G020.4+00.1	S	0.07	–	12.1	14.3	1.7	26.3	0.0	-13.24	-12.5	-12.8	–	–	–
G021.0-00.4	S	0.07	–	18.7	22.5	0.0	0.4	0.0	–	-12.8	-13.34	–	–	–
G021.5-00.1	S	0.04	–	30.9	21.3	1.2	18.2	0.0	-13.09	-12.58	-12.82	–	–	–
G021.5-00.9	C	0.03	–	10.3	27.1	6.4	112.2	47.0	-12.42	-12.26	-12.35	–	–	–
G021.8-00.6	S	0.17	–	2.8	28.2	2.0	69.9	0.0	-12.67	-12.3	-12.49	–	-11.5	-11.89
G022.7-00.2	S?	0.22	–	3.7	24.5	6.1	237.1	119.2	-11.99	-11.85	-11.93	–	-11.88	-12.18
G023.3-00.3	S	0.22	–	2.7	18.9	15.6	588.6	332.0	-11.57	-11.49	-11.53	–	-11.42	-11.74
G023.6+00.3	?	0.08	–	7.9	20.3	1.5	29.7	0.0	-12.8	-12.39	-12.59	–	-13.09	–
G024.7+00.6	C?	0.2	–	4.7	14.9	3.3	90.7	5.4	-12.29	-11.99	-12.15	–	-12.23	-12.88
G024.7-00.6	S?	0.12	–	7.4	23.7	7.7	200.1	63.1	-12.18	-12.01	-12.1	–	-12.98	-14.67
G027.4+00.0	S	0.03	–	10.3	24.7	6.0	94.3	27.4	-12.48	-12.29	-12.4	–	–	–
G027.8+00.6	F	0.34	–	3.6	19.3	2.8	127.5	33.3	-12.05	-11.8	-11.94	–	-11.83	-12.08
G028.6-00.1	S	0.09	–	11.7	33.2	7.1	179.0	66.8	-12.3	-12.14	-12.23	–	–	–
G029.6+00.1	S	0.04	–	17.8	33.2	4.5	80.8	17.5	-12.7	-12.46	-12.59	–	–	–
G029.7-00.3	C	0.03	–	8.7	35.6	10.1	177.4	94.0	-12.32	-12.2	-12.27	–	-13.26	–
G030.7+01.0	S?	0.18	–	7.9	29.1	-0.3	-11.0	0.0	–	-12.59	-13.06	–	-13.09	–
G030.7-02.0	?	0.13	–	23.4	12.9	0.9	16.2	0.0	–	-12.49	-12.97	–	–	–
G031.5-00.6	S?	0.15	–	12.8	36.3	1.9	60.1	0.0	-13.08	-12.5	-12.76	–	–	–
G031.9+00.0	S	0.05	7.2	5.4	42.2	0.0	0.0	0.0	–	-12.92	-13.35	-12.76	-12.46	-13.52
G032.1-00.9	C?	0.33	–	–	26.5	1.1	52.3	0.0	-12.7	-12.16	-12.41	–	–	–
G032.4+00.1	S	0.05	–	33.9	42.0	2.2	45.1	0.0	-13.08	-12.68	-12.88	–	–	–
G032.8-00.1	S?	0.14	–	6.3	42.0	4.7	158.5	39.8	-12.48	-12.26	-12.38	–	-12.73	-14.07
G033.2-00.6	S	0.15	–	10.1	44.5	2.5	85.6	0.0	-12.91	-12.48	-12.69	–	–	–
G033.6+00.1	S	0.08	7.1	5.1	51.4	2.7	74.8	5.9	-12.83	-12.53	-12.69	-12.75	-12.39	-13.39
G034.7-00.4	C	0.26	–	1.6	40.5	4.5	224.2	56.1	-12.3	-12.08	-12.2	–	-10.84	-10.58
G036.6+02.6	S	0.13	–	20.5	0.4	-1.4	-3.2	0.0	–	-11.7	-12.72	–	–	–
G036.6-00.7	S?	0.21	–	–	14.7	0.2	5.2	0.0	-13.31	-12.29	-12.64	–	–	–
G039.2-00.3	C	0.06	–	5.9	31.5	0.5	7.4	0.0	-13.15	-12.62	-12.87	–	-12.62	-13.84
G039.7-02.0	?	0.79	–	2.0	11.1	0.6	38.0	0.0	–	-11.94	-12.59	–	-11.08	-11.06
G040.5-00.5	S	0.18	–	6.1	28.5	8.0	234.2	70.1	-12.11	-11.94	-12.04	–	-12.66	-13.93
G041.1-00.3	S	0.03	–	6.0	27.2	3.0	37.9	9.4	-12.69	-12.43	-12.57	–	-12.65	-13.92
G042.8+00.6	S	0.2	–	10.3	15.6	1.1	24.6	0.0	-12.41	-12.07	-12.24	–	–	–
G043.3-00.2	S	0.03	7.5	4.8	28.8	1.0	12.8	0.0	-13.88	-12.83	-13.18	-12.8	-12.29	-13.18
G043.9+01.6	S?	0.5	–	5.7	11.5	-1.2	-49.7	0.0	–	-12.11	-12.6	–	-12.56	-13.74
G045.7-00.4	S	0.18	–	9.1	24.2	2.2	65.8	0.0	-12.71	-12.28	-12.49	–	-13.34	–
G046.8-00.3	S	0.13	6.4	5.8	16.9	0.9	17.3	0.0	–	-12.55	-13.05	-12.66	-12.59	-13.79
G049.2-00.7	S?	0.25	6.0	1.9	15.6	2.3	60.2	2.1	-12.26	-11.95	-12.11	-12.6	-11.0	-10.88
G053.6-02.2	S	0.25	5.0	6.6	3.9	-0.7	-9.0	0.0	–	-12.39	-13.73	-12.44	-12.79	-14.2
G054.1+00.3	F?	0.01	–	34.1	23.9	3.8	38.5	9.5	-12.64	-12.39	-12.52	–	–	–
G054.4-00.3	S	0.33	3.3	3.7	19.8	-0.5	-16.9	0.0	–	-12.54	-13.74	-12.08	-11.88	-12.18
G055.0+00.3	S	0.15	–	23.0	23.3	-0.2	-4.3	0.0	-13.07	-12.36	-12.66	–	–	–
G057.2+00.8	S?	0.1	–	14.3	15.7	0.8	11.6	0.0	-12.93	-12.31	-12.59	–	–	–
G059.5+00.1	S	0.12	–	11.1	14.3	1.4	21.2	0.0	-12.79	-12.22	-12.48	–	–	–
G059.8+01.2	?	0.15	–	14.1	6.1	1.6	17.0	0.0	-12.37	-11.93	-12.14	–	–	–
G279.0+01.1	S	0.79	–	3.2	1.0	1.7	34.1	0.0	-11.42	-11.06	-11.25	–	-11.64	-12.17

Continued on next page

Table A.2 – continued from previous page

SNR	Type	Radius	Distance		Expo-	Signi-	Excess	Excess	Integral flux	Upper Limit		Theoretical flux prediction		
			known	calc.	sure-	ficance		Lower limit		99% CL	68% CL	known dist.	calc. dist.	error
		[deg]	[kpc]	[kpc].	[h]	[σ]	[counts]	[counts]	[$\log_{10}$cm^{-2}s^{-1}]	[$\log_{10}$cm^{-2}s^{-1}]		[$\log_{10}$cm^{-2}s^{-1}]	[$\log_{10}$cm^{-2}s^{-1}]	[$\log_{10}$cm^{-2}s^{-1}]
G284.3-01.8	S	0.2	–	6.0	29.3	6.2	198.7	79.9	-12.05	-11.89	-11.98	–	-12.64	-13.88
G286.5-01.2	S?	0.16	–	14.8	27.3	2.6	62.7	0.0	-12.73	-12.26	-12.48	–	–	–
G289.7-00.3	S	0.13	–	8.1	16.2	0.3	5.5	0.0	-13.1	-12.31	-12.62	–	-13.15	–
G290.1-00.8	S	0.14	–	3.6	16.5	0.7	12.0	0.0	-13.2	-12.33	-12.66	–	-11.84	-12.09
G291.0-00.1	C	0.12	–	5.6	26.5	2.7	60.0	0.0	-12.78	-12.33	-12.55	–	-12.52	-13.64
G292.0+01.8	C	0.08	–	6.0	16.8	2.6	40.0	0.0	-12.96	-12.37	-12.63	–	-12.65	-13.9
G292.2-00.5	S	0.15	–	7.6	27.4	6.4	165.8	66.8	-12.09	-11.93	-12.02	–	-13.03	-14.77
G293.8+00.6	C	0.17	–	8.6	14.9	0.9	17.8	0.0	-12.6	-12.1	-12.33	–	-13.24	–
G294.1-00.0	S	0.33	–	11.3	13.2	0.1	2.4	0.0	–	-12.29	-13.28	–	–	–
G296.1-00.5	S	0.26	–	6.5	14.6	-0.2	-3.5	0.0	–	-12.32	-13.22	–	-12.78	-14.18
G296.8-00.3	S	0.14	–	6.9	18.3	0.4	6.2	0.0	-14.24	-12.32	-12.73	–	-12.86	-14.43
G298.5-00.3	?	0.04	–	10.7	18.7	2.2	24.2	0.0	-12.65	-12.3	-12.48	–	–	–
G298.6-00.0	S	0.09	–	9.5	18.0	3.8	55.3	0.0	-12.66	-12.25	-12.46	–	-13.41	–
G299.2-02.9	S	0.12	–	23.6	0.3	-1.8	-3.1	0.0	–	-11.36	-11.88	–	–	–
G299.6-00.5	S	0.11	–	18.1	23.4	0.3	5.0	0.0	-13.31	-12.44	-12.77	–	–	–
G301.4-01.0	S	0.26	–	11.5	11.4	-1.0	-20.2	0.0	-12.81	-12.01	-12.33	–	–	–
G302.3+00.7	S	0.14	–	8.8	11.9	1.8	31.2	0.0	-14.04	-12.25	-12.65	–	-13.28	–
G304.6+00.1	S	0.07	7.9	6.4	79.6	4.4	133.6	0.0	-13.21	-12.71	-12.94	-12.84	-12.76	-14.13
G308.1-00.7	S	0.11	–	16.7	16.4	0.4	5.7	0.0	-14.38	-12.43	-12.83	–	–	–
G308.8-00.1	C?	0.21	–	5.2	17.6	1.7	43.0	0.0	-12.43	-12.03	-12.23	–	-12.41	-13.42
G309.2-00.6	S	0.11	–	7.9	21.8	-0.0	-0.1	0.0	-13.03	-12.36	-12.65	–	-13.11	–
G309.8+00.0	S	0.19	3.6	5.0	19.6	1.3	30.8	0.0	-13.23	-12.28	-12.63	-12.16	-12.36	-13.32
G310.6-00.3	S	0.07	–	9.9	19.1	1.2	16.6	0.0	-13.38	-12.51	-12.84	–	-13.49	–
G310.8-00.4	S	0.1	–	8.6	18.8	-0.7	-11.4	0.0	–	-12.72	-13.57	–	-13.25	–
G311.5-00.3	S	0.04	–	13.3	17.1	-2.8	-30.1	0.0	–	-13.0	-14.16	–	–	–
G312.4-00.4	S	0.32	–	3.1	18.8	4.9	184.2	73.8	-11.82	-11.64	-11.74	–	-11.6	-12.1
G312.5-03.0	S	0.16	–	10.0	1.1	1.0	5.5	0.0	-11.65	-11.27	-11.46	–	–	–
G315.4-00.3	?	0.16	–	7.1	20.5	1.2	28.5	0.0	–	-12.46	-12.98	–	-12.92	-14.54
G315.4-02.3	S	0.35	2.8	2.9	40.0	12.1	795.9	512.6	-11.59	-11.51	-11.56	-11.94	-11.53	-11.96
G315.9-00.0	S	0.17	–	18.5	17.3	-2.1	-46.0	0.0	–	-12.78	-14.05	–	–	–
G316.3-00.0	S	0.19	–	4.7	19.5	1.0	27.0	0.0	–	-12.4	-12.94	–	-12.24	-12.9
G317.3-00.2	S	0.09	–	9.7	28.2	2.7	55.2	9.7	-12.56	-12.28	-12.43	–	-13.45	–
G318.2+00.1	S	0.31	–	8.6	31.5	7.1	347.2	110.8	-11.96	-11.79	-11.89	–	-13.25	–
G318.9+00.4	C	0.2	–	9.2	29.4	1.1	34.5	0.0	-13.33	-12.39	-12.73	–	-13.36	–
G320.4-01.2	C	0.29	–	2.8	25.0	27.2	1434.0	1048.0	-11.17	-11.13	-11.16	–	-11.46	-11.8
G320.6-01.6	S	0.4	–	–	14.3	8.6	396.4	258.9	-11.41	-11.3	-11.36	–	–	–
G321.9-00.3	S	0.23	–	5.5	28.3	1.4	56.8	0.0	-12.96	-12.29	-12.58	–	-12.49	-13.58
G321.9-01.1	S	0.23	–	9.6	35.6	-1.7	-81.0	0.0	–	-12.93	-14.26	–	-13.43	–
G322.5-00.1	C	0.12	–	14.9	20.2	0.3	7.1	0.0	–	-12.83	-13.9	–	–	–
G323.5+00.1	S	0.11	–	11.4	17.7	0.5	8.7	0.0	–	-12.68	-13.48	–	–	–
G326.3-01.8	C	0.32	–	1.9	18.4	0.1	4.8	0.0	-13.1	-12.15	-12.49	–	-11.0	-10.89
G327.1-01.1	C	0.15	–	7.6	24.9	2.8	67.2	14.0	-12.4	-12.13	-12.27	–	-13.03	-14.76
G327.2-00.1	S	0.04	–	30.9	29.8	0.4	5.2	0.0	–	-12.89	-13.49	–	–	–
G327.4+00.4	S	0.17	–	4.0	24.1	1.6	42.4	0.0	-12.75	-12.26	-12.49	–	-11.99	-12.4
G327.4+01.0	S	0.12	–	13.6	21.8	-1.5	-30.4	0.0	–	-12.69	-13.43	–	–	–
G328.4+00.2	F	0.04	–	6.7	25.7	0.2	2.3	0.0	-13.44	-12.67	-12.97	–	-12.83	-14.28
G329.7+00.4	S	0.31	–	3.5	13.6	0.0	0.3	0.0	-12.67	-12.05	-12.32	–	-11.78	-11.98
G330.2+01.0	S?	0.09	–	9.4	12.4	1.3	19.8	0.0	-14.76	-12.48	-12.89	–	-13.4	–
G332.0+00.2	S	0.1	–	7.6	8.8	4.3	66.2	18.7	-12.15	-11.93	-12.05	–	-13.04	-14.79
G332.4+00.1	S	0.12	–	4.5	7.6	11.3	195.8	105.6	-11.6	-11.48	-11.55	–	-12.17	-12.76
G332.4-00.4	S	0.08	3.4	4.6	7.0	9.9	132.1	64.3	-11.75	-11.62	-11.69	-12.11	-12.23	-12.87
G335.2+00.1	S	0.17	–	5.2	11.3	3.8	91.9	22.2	-12.12	-11.88	-12.01	–	-12.41	-13.44
G336.7+00.5	S	0.1	–	8.6	10.6	5.5	100.9	40.5	-12.03	-11.85	-11.95	–	-13.25	–
G337.0-00.1	S	0.01	–	21.5	12.6	6.2	68.9	14.0	-12.43	-12.21	-12.34	–	–	–
G337.2+00.1	?	0.02	–	19.8	12.3	7.7	92.3	39.5	-12.17	-12.02	-12.1	–	–	–

Continued on next page

Table A.2 – continued from previous page

SNR	Type	Radius	Distance		Expo-	Signi-	Excess	Excess	Integral flux	Upper Limit		Theoretical flux prediction		
			known	calc.	sure-	ficance		Lower limit		99% CL	68% CL	known dist.	calc. dist.	error
		[deg]	[kpc]	[kpc].	[h]	[σ]	[counts]	[counts]	[$\log_{10}\mathrm{cm}^{-2}\mathrm{s}^{-1}$]	[$\log_{10}\mathrm{cm}^{-2}\mathrm{s}^{-1}$]		[$\log_{10}\mathrm{cm}^{-2}\mathrm{s}^{-1}$]	[$\log_{10}\mathrm{cm}^{-2}\mathrm{s}^{-1}$]	[$\log_{10}\mathrm{cm}^{-2}\mathrm{s}^{-1}$]
G337.2-00.7	S	0.05	–	17.2	15.8	3.4	50.9	6.8	-12.51	-12.23	-12.38	–	–	–
G337.3+01.0	S	0.11	–	5.6	9.4	-0.9	-15.1	0.0	–	-12.65	-13.66	–	-12.53	-13.66
G337.8-00.1	S	0.06	–	5.8	21.1	3.2	57.8	8.7	-12.54	-12.27	-12.41	–	-12.6	-13.8
G338.1+00.4	S	0.12	–	9.9	22.3	1.8	45.9	0.0	-12.52	-12.2	-12.37	–	-13.48	–
G338.3-00.0	C?	0.07	–	8.6	29.8	24.5	609.8	382.6	-11.63	-11.57	-11.6	–	-13.25	–
G338.5+00.1	?	0.08	–	6.7	31.5	8.8	212.2	101.7	-12.12	-11.99	-12.06	–	-12.83	-14.28
G340.4+00.4	S	0.07	–	9.8	30.1	1.7	36.8	0.0	-13.49	-12.62	-12.95	–	-13.47	–
G340.6+00.3	S	0.05	–	10.4	29.4	1.8	33.6	0.0	-13.31	-12.61	-12.91	–	–	–
G341.2+00.9	C	0.16	–	14.3	14.6	0.8	18.0	0.0	-12.52	-12.11	-12.32	–	–	–
G341.9-00.3	S	0.06	–	13.6	15.6	1.0	14.2	0.0	-13.52	-12.54	-12.89	–	–	–
G342.0-00.2	S	0.09	–	11.0	11.1	0.7	9.9	0.0	-13.49	-12.43	-12.79	–	–	–
G342.1+00.9	S	0.08	–	25.4	9.9	0.6	8.3	0.0	-12.78	-12.29	-12.52	–	–	–
G343.1-00.7	S	0.2	–	6.9	14.4	0.9	28.0	0.0	-12.8	-12.17	-12.45	–	-12.87	-14.45
G343.1-02.3	C?	0.27	–	6.5	12.3	5.8	211.7	81.7	-11.81	-11.64	-11.73	–	-12.78	-14.17
G344.7-00.1	C?	0.08	–	12.8	8.1	5.4	83.2	25.3	-12.08	-11.88	-11.99	–	–	–
G345.7-00.2	S	0.05	–	25.3	37.3	4.3	103.0	34.5	-12.48	-12.27	-12.39	–	–	–
G346.6-00.2	S	0.07	–	8.1	46.2	3.8	116.3	39.7	-12.5	-12.29	-12.41	–	-13.15	–
G347.3-00.5	S?	0.5	–	–	5.0	22.7	978.9	670.0	-10.78	-10.73	-10.76	–	–	–
G348.5+00.1	S	0.12	9.0	2.9	49.8	8.8	352.9	137.5	-12.16	-12.03	-12.11	-12.95	-11.54	-11.96
G348.5-00.0	S?	0.08	–	7.2	41.0	4.1	117.4	53.3	-12.36	-12.17	-12.28	–	-12.94	-14.57
G348.7+00.3	S	0.14	9.0	4.4	54.1	9.1	419.3	135.9	-12.19	-12.04	-12.12	-12.95	-12.14	-12.7
G349.2-00.1	S	0.06	–	17.1	40.2	0.3	7.3	0.0	–	-12.86	-13.51	–	–	–
G349.7+00.2	S	0.02	13.8	6.8	25.8	3.6	55.5	1.7	-12.78	-12.47	-12.63	-13.33	-12.84	-14.3
G350.0-02.0	S	0.38	–	3.8	4.8	-0.3	-7.2	0.0	–	-11.79	-12.29	–	-11.9	-12.22
G350.1-00.3	?	0.03	–	10.3	25.7	2.1	34.4	0.0	-13.67	-12.7	-13.05	–	–	–
G351.2+00.1	C?	0.06	–	10.1	20.2	1.7	30.4	0.0	-12.89	-12.44	-12.66	–	–	–
G351.7+00.8	S	0.13	–	6.6	16.0	-2.7	-59.7	0.0	–	-12.6	-13.34	–	-12.81	-14.23
G351.9-00.9	S	0.09	–	14.6	28.5	1.4	32.8	0.0	-13.13	-12.52	-12.79	–	–	–
G352.7-00.1	S	0.06	–	11.1	40.3	2.7	65.6	9.8	-12.75	-12.47	-12.62	–	–	–
G353.6-00.7	S	0.25	–	10.8	48.4	15.6	1032.0	586.5	-11.68	-11.6	-11.65	–	–	–
G353.9-02.0	S	0.11	–	18.1	29.8	-1.6	-39.9	0.0	–	-13.03	-14.27	–	–	–
G354.1+00.1	C?	0.09	–	–	42.0	1.9	55.2	0.0	-12.99	-12.55	-12.76	–	–	–
G354.8-00.8	S	0.16	–	11.0	37.4	1.0	38.6	0.0	–	-12.78	-13.58	–	–	–
G355.4+00.7	S	0.21	–	8.3	16.5	0.6	18.2	0.0	-13.24	-12.27	-12.62	–	-13.18	–
G355.6-00.0	S	0.06	–	12.6	19.0	2.7	47.7	0.0	-12.7	-12.36	-12.53	–	–	–
G355.9-02.5	S	0.11	–	7.5	1.9	0.6	4.8	0.0	-12.22	-11.79	-12.0	–	-13.02	-14.75
G356.3-00.3	S	0.08	–	12.0	10.5	0.9	15.0	0.0	-12.76	-12.28	-12.51	–	–	–
G356.3-01.5	S	0.15	–	10.8	5.7	-2.7	-43.5	0.0	–	-12.69	-13.99	–	–	–
G357.7+00.3	S	0.2	–	6.2	41.2	1.5	75.4	0.0	-12.71	-12.29	-12.5	–	-12.7	-14.02
G357.7-00.1	?	0.05	–	4.5	33.6	4.1	93.5	8.1	-12.71	-12.43	-12.58	–	-12.17	-12.75
G358.1+00.1	S	0.17	–	12.6	46.6	1.8	83.0	0.0	-12.94	-12.43	-12.67	–	–	–
G358.5-00.9	S	0.14	–	9.7	75.4	8.2	452.3	222.7	-12.24	-12.11	-12.19	–	-13.45	–
G359.0-00.9	S	0.19	–	4.4	70.6	6.6	423.7	166.0	-12.26	-12.1	-12.19	–	-12.15	-12.71
G359.1+00.9	S	0.1	–	13.8	87.9	0.3	14.0	0.0	-13.45	-12.78	-13.07	–	–	–
G359.1-00.5	S	0.2	9.2	5.4	90.8	9.4	714.2	352.8	-12.15	-12.03	-12.1	-12.97	-12.47	-13.55

List of Figures

List of Tables

Bibliography

Abdo, A. A., Ackermann, M., Ajello, M., et al. 2010, Fermi/Large Area Telescope 1 year catalog, `http://fermi.gsfc.nasa.gov/ssc/data/access/lat/1yr_catalog/1FGL_catalog_v2.pdf`

Abdo, A. A., Ackermann, M., Ajello, M., et al. 2009, ApJS, 183, 46

Abdo, A. A., Allen, B., Berley, D., et al. 2007, ApJ, 664, L91

Aharonian. 1993, in Towards a Major Atmospheric Cherenkov Detector – II for TeV Astro/Particle Physics, ed. R. C. Lamb, 81–+

Aharonian, F., Akhperjanian, A. G., Anton, G., et al. 2009a, A&A, 499, 723

Aharonian, F., Akhperjanian, A. G., Aye, K., et al. 2005a, A&A, 432, L25

Aharonian, F., Akhperjanian, A. G., Aye, K., et al. 2005b, A&A, 432, L9

Aharonian, F., Akhperjanian, A. G., Aye, K., et al. 2005c, Science, 307, 1938

Aharonian, F., Akhperjanian, A. G., Aye, K., et al. 2005d, Science, 309, 746

Aharonian, F., Akhperjanian, A. G., Aye, K., et al. 2005e, A&A, 442, 1

Aharonian, F., Akhperjanian, A. G., Aye, K., et al. 2005f, A&A, 435, L17

Aharonian, F., Akhperjanian, A. G., Barres de Almeida, U., et al. 2008a, A&A, 477, 353

Aharonian, F., Akhperjanian, A. G., Barres de Almeida, U., et al. 2008b, A&A, 490, 685

Aharonian, F., Akhperjanian, A. G., Barres de Almeida, U., et al. 2008c, A&A, 486, 829

Aharonian, F., Akhperjanian, A. G., Bazer-Bachi, A. R., et al. 2008d, A&A, 481, 401

Aharonian, F., Akhperjanian, A. G., Bazer-Bachi, A. R., et al. 2007a, A&A, 472, 489

Aharonian, F., Akhperjanian, A. G., Bazer-Bachi, A. R., et al. 2006a, A&A, 457, 899

Aharonian, F., Akhperjanian, A. G., Bazer-Bachi, A. R., et al. 2006b, A&A, 449, 223

Aharonian, F., Akhperjanian, A. G., Bazer-Bachi, A. R., et al. 2006c, Nature, 439, 695

Aharonian, F., Akhperjanian, A. G., Bazer-Bachi, A. R., et al. 2006d, ApJ, 636, 777

Aharonian, F., Akhperjanian, A. G., Bazer-Bachi, A. R., et al. 2007b, A&A, 464, 235

Aharonian, F., Akhperjanian, A. G., Bazer-Bachi, A. R., et al. 2006e, A&A, 460, 743

Aharonian, F., Akhperjanian, A. G., Bazer-Bachi, A. R., et al. 2006f, A&A, 460, 365

Aharonian, F., Akhperjanian, A. G., de Almeida, U. B., et al. 2009b, ApJ, 692, 1500

Aharonian, F. A. 2004, Very high energy cosmic gamma radiation : a crucial window on the extreme Universe (World Scientific Publishing Company; 1st edition (April 30, 2003))

Aharonian, F. A., Akhperjanian, A. G., Aye, K., et al. 2004, Nature, 432, 75

Aharonian, F. A., Akhperjanian, A. G., Bazer-Bachi, A. R., et al. 2005g, A&A, 442, L25

Aharonian, F. A., Akhperjanian, A. G., Beilicke, M., et al. 2002, A&A, 395, 803

Aharonian, F. A., Atoyan, A. M., & Kifune, T. 1997, MNRAS, 291, 162

Axford, W. I., Leer, E., & Skadron, G. 1977, in International Cosmic Ray Conference, Vol. 11, International Cosmic Ray Conference, 132–+

Bell, A. R. 1978, MNRAS, 182, 147

Berge, D. 2006, PhD thesis, Ruperto-Carola University of Heidelberg

Blandford, R. D. & Ostriker, J. P. 1978, ApJ, 221, L29

Blumenthal, G. R. & Gould, R. J. 1970, Reviews of Modern Physics, 42, 237

Bolz, O. 2004, PhD thesis, Ruperto-Carola University of Heidelberg

Braun, I. 2007, PhD thesis, Ruperto-Carola University of Heidelberg

Camilo, F., Bell, J. F., Manchester, R. N., et al. 2001, ApJ, 557, L51

Camilo, F., Gaensler, B. M., Gotthelf, E. V., Halpern, J. P., & Manchester, R. N. 2004, ApJ, 616, 1118

Camilo, F., Kaspi, V. M., Lyne, A. G., et al. 2000, ApJ, 541, 367

Carroll, B. W. & Ostlie, D. A. 1996, An Introduction to Modern Astrophysics (Addison-Wesely Publishing Comp.)

Case, G. L. & Bhattacharya, D. 1998, ApJ, 504, 761

Claussen, M. J., Goss, W. M., Frail, D. A., & Desai, K. 1999, ApJ, 522, 349

Colin, P., Borla Tridon, D., Carmona, E., et al. 2009, ArXiv e-prints

Daum, A., Hermann, G., Hess, M., et al. 1997, Astroparticle Physics, 8, 1

Davies, J. & Cotton, E. 1957, Journal of Solar Energy Science and Engineering

Djannati-Atai, A., De Jager, O., Terrier, R., Gallant, Y., & for the H.E.S.S. Collaboation, H. S. 2007, in 30th International Cosmic Ray Conference, arXiv:0710.2247v1, 46–49

Drury, L. O., Aharonian, F. A., & Voelk, H. J. 1994, A&A, 287, 959

Feldman, G. J. & Cousins, R. D. 1998, Phys.Rev.D, 57, 3873

Fermi, E. 1949, Physical Review, 75, 1169

Finley, J. P., Srinivasan, R., & Park, S. 1996, ApJ, 466, 938

Fonseca, V. 1998, Ap&SS, 263, 377

Funk, S., Hermann, G., Hinton, J., et al. 2004, Astropart.Phys., 22, 285

Gaensler, B. M., Schulz, N. S., Kaspi, V. M., Pivovaroff, M. J., & Becker, W. E. 2003, ApJ, 588, 441

Gotthelf, E. V. & Halpern, J. P. 2008, ApJ, 681, 515

Gotthelf, E. V., Vasisht, G., Boylan-Kolchin, M., & Torii, K. 2000, ApJ, 542, L37

Green, A. J., Cram, L. E., Large, M. I., & Ye, T. 1999, ApJS, 122, 207

Green, D. A. 2009, Bulletin of the Astronomical Society of India, 37, 45

Hartman, R. C., Bertsch, D. L., Bloom, S. D., et al. 1999, VizieR Online Data Catalog, 212, 30079

HEGRA Collaboration, Konopelko, A., Hemberger, M., et al. 1999, Astroparticle Physics, 10, 275

Heitler, W. 1954, Quantum theory of radiation (Dover Publications; 3 edition (April 1, 1984))

Hillas, A. M. 1985, in International Cosmic Ray Conference, ed. F. C. Jones, Vol. 3, 445–448

Hinton, J. A. 2004, New Astronomy Review, 48, 331

Hoppe, S. 2008, PhD thesis, Ruperto-Carola University of Heidelberg

Hoppe, S., de Oña-Wilhemi, E., Khélifi, B., et al. 2009, ArXiv e-prints

K. Gaisser, T. 1990, Cosmic Rays And Particle Physics (Cambridge University Press)

Krymskii, G. F. 1977, Akademiia Nauk SSSR Doklady, 234, 1306

Kubo, H., Asahara, A., Bicknell, G. V., et al. 2004, New Astronomy Review, 48, 323

Lagage, P. O. & Cesarsky, C. J. 1983, A&A, 125, 249

Lamb, R. C. & Macomb, D. J. 1997, ApJ, 488, 872

Li, T. & Ma, Y. 1983, ApJ, 272, 317

Longair, M. S. 1994, High-energy astrophysics. Vol. 2: Stars, the galaxy and the interstellar medium, Vol. 2 (Cambridge, UK: University Press), (1994) 393 p

Manchester, R. N., Hobbs, G. B., Teoh, A., & Hobbs, M. 2005, AJ, 129, 1993

Meyer, M., Horns, D., & Zechlin, H.-S. 2010, Astronomy & Astrophysics, submitted

Motch, C., Haberl, F., Dennerl, K., Pakull, M., & Janot-Pacheco, E. 1997, A&A, 323, 853

Naumann-Godó, M., Beilicke, M., Hauser, D., Lemoine-Goumard, M., & de Naurois, M. 2008, in American Institute of Physics Conference Series, Vol. 1085, American Institute of Physics Conference Series, ed. F. A. Aharonian, W. Hofmann, & F. Rieger, 304–307

Ohm, S. 2010, PhD thesis, Ruperto-Carola University of Heidelberg

Ptuskin, V. S. & Zirakashvili, V. N. 2005, A&A, 429, 755

Reach, W. T., Rho, J., & Jarrett, T. H. 2005, ApJ, 618, 297

Ritz, S. M., Michelson, P. F., Meegan, C., Grindlay, J., & GLAST Mission Team. 2007, in Bulletin of the American Astronomical Society, Vol. 38, Bulletin of the American Astronomical Society, 909–+

Sedov, L. I. 1946, Journal of Applied Mathematics and Mechanics, 10, 241

Stead, J. J. & Hoare, M. G. 2010, MNRAS, 407, 923

Sugizaki, M., Mitsuda, K., Kaneda, H., et al. 2001a, VizieR Online Data Catalog, 213, 40077

Sugizaki, M., Mitsuda, K., Kaneda, H., et al. 2001b, ApJS, 134, 77

Taylor, G. 1950, Royal Society of London Proceedings Series A, 201, 159

Tian, W. W., Leahy, D. A., Haverkorn, M., & Jiang, B. 2008, ApJ, 679, L85

Tluczykont, M. 2005, in American Institute of Physics Conference Series, Vol. 745, High Energy Gamma-Ray Astronomy, ed. F. A. Aharonian, H. J. Völk, & D. Horns, 785–790

Tomsick, J. A., Lingenfelter, R., Walter, R., et al. 2003, IAU Circ., 8076, 1

Torii, K., Kinugasa, K., Toneri, T., et al. 1998, ApJ, 494, L207+

Trussoni, E., Massaglia, S., Caucino, S., Brinkmann, W., & Aschenbach, B. 1996, A&A, 306, 581

Unsöld, A. & Baschek, B. 1999, Der neue Kosmos. Einführung in die Astronomie und Astrophysik. (Springer Verlag)

van Eldik, C., Bolz, O., Braun, I., & et al. 2008, in International Cosmic Ray Conference, Vol. 2, International Cosmic Ray Conference, 589–592

Vincent, P., Denanca, J., Huppert, J., et al. 2003, in International Cosmic Ray Conference, Vol. 5, International Cosmic Ray Conference, 2887–+

Voges, W., Aschenbach, B., Boller, T., et al. 1999, A&A, 349, 389

Weekes, T. C., Badran, H., Biller, S. D., et al. 2002, Astroparticle Physics, 17, 221

Weekes, T. C., Cawley, M. F., Fegan, D. J., et al. 1989, ApJ, 342, 379

Wilhelmi, E. d. O., Terrier, R., Brun, F.and Chavez, R., et al. 2010, Observations of SNR G284.3-1.9 from X-rays to VHE gamma-rays with XMM-Newton, Fermi LAT and H.E.S.S., COSPAR 2010

Winston, R. 1970, J. Opt. Soc. Am., 60, 245

Woltjer, L. 1972, ARA&A, 10, 129

Yamazaki, R., Kohri, K., Bamba, A., et al. 2006, MNRAS, 371, 1975

Danke!

Für die Unterstützung während meiner Doktorarbeit gilt sehr vielen Menschen mein herzlicher Dank. Besonders möchte ich mich bei meinem Doktorvater Werner Hofmann für die Möglichkeit bedanken, im Rahmen der H.E.S.S.-Kollaboration zu promovieren. Mit Ihren wertvollen Ratschlägen haben Sie sehr zum Gelingen dieser Arbeit beigetragen. Des Weiteren möchte ich meinem Zweitgutachter Heinz Völk danken. Von Ihrer Erfahrung auf dem Gebiet der Supernovaüberreste habe ich sehr profitiert und danke Ihnen für viele ausgiebige Diskussionen. Für die Betreuung im Rahmen der International Max Planck Research School und die Unermüdlichkeit für die Sache der Studenten danke ich herzlich Christian Fendt. Mein Dank gilt auch Gesine Heinzelmann, die den Studenten der Graduate School for Fundamental Physics immer hilfsbereit und freundlich zur Seite steht.

Für die Arbeit am zentralen Trigger gilt mein besonderer Dank Christopher van Eldik, der mir mit viel Geduld Verständnis für die Elektronik des zentralen Triggers und wesentliche Programmierkenntnisse beibrachte. Ich danke weiterhin German Hermann, Thomas Schwab, Christian Föhr, Christian Bauer und allen Mitarbeitern der Elektronikwerkstatt, die mir während der Arbeit am Trigger hilfreich zur Seite standen und mir die Feinheiten der Elektronik näher gebracht haben.
Ohne umfangreiche Hilfe bei der Untersuchung der Supernovaüberreste wäre ich aufgeschmissen gewesen. Deshalb danke ich sehr herzlich Henning Gast, Stefan Ohm, Svenja Carrigan, Andreas Förster, Christopher van Eldik, Daniil Nekrassov, André-Claude Clapson und Christoph Deil für die Beantwortung vieler Fragen zu Supernovaüberresten, ROOT, C++, der H.E.S.S.-Software und der allgemeinen Physik. Wilfried Domainko danke ich sehr für stundenlange Erklärungen der Astronomie am Anfang meiner Doktorarbeit.
Mein herzlicher Dank gilt allen fleissigen Korrekturlesern dieser Dissertation: Henning Gast, Svenja Carrigan, Christopher van Eldik, Stefan Ohm, Petter Hofverberg und Joachim Hahn. Ich danke Ruth Crespo für die fröhliche Stimmung im Sekretariat und ihre schnelle Hilfe in allen Dingen, Jörg Baumgart für technische Hilfe und Thomas Kihm für viele Shell-Skripte.

Neben der Anerkennung für fachliche Unterstützung gilt mein Dank besonders denjenigen, die mir während der Doktorarbeit menschlich zur Seite standen. Ich danke deshalb von ganzem Herzen Ruth, Svenja, Henning, Raquel, Daniil und Stefan für euer immer offenes Ohr und Joachim für deine dauerhaft gute Laune, die einfach ansteckend ist.
Ich möchte mich auch bei Roland Schorr, Antonino Di Piazza, Giuseppe Sansone, Pau Carriò Gaspar und Alexandre Urzhumtsev für ihre Freundschaft bedanken. Meinen lieben Mitbewohnern aus der besten WG danke ich für die letzten drei Jahre, die wir zusammen gewohnt, gefeiert und viel Spaß gehabt haben und in denen ihr alle Höhen und Tiefen der Doktorarbeit miterlebt habt: Catharina, Lea, Nilda, Martin, Max, Olli, Tarek, Sara, Sasi, Simon, Stephan und Verena.
Mein besonderer Dank gilt Sebastian Schöning, Michael Henke, Patrick Plötz und Giovanni Natale, die mir vor allem in der Endphase immer wieder neuen Schwung gegeben haben und ohne die diese Arbeit niemals fertig gestellt worden wäre.

Schließlich danke ich meinen Eltern, meinen Brüdern und Kerstin für ihre Unterstützung aus der Ferne, für viele aufmunternde Telefonate, liebevoll gepackte Carepakete und für ungefähr 300 Postkarten, die ihren Weg nach Heidelberg gefunden haben.